LIQUID PHASE EXFOLIATION OF TWO DIMENSIONAL CRYSTALS

ARLENE O'NEILL

A thesis submitted for the degree of

Doctor of Philosophy

Supervised by Prof. Jonathan Coleman

Chemical Physics of Low Dimensional Nanostructures Group

School of Physics

Trinity College Dublin

2013

To my beautiful mother Denise,

Thank you for always giving me the best tools.

This is as much for you as it for me.

DECLARATION

I declare that this thesis has not been submitted as an exercise for a degree at this or any other university and it is entirely my own work.

I agree to deposit this thesis in the University's open access institutional repository or allow the library to do so on my behalf, subject to Irish Copyright Legislation and Trinity College Library conditions of use and acknowledgement.

Elements of this work that have been carried out jointly with others or by collaborators have been duly acknowledged in the text wherever included.

Arlene O'Neill

ABSTRACT

In recent years, two dimensional materials have received widespread attention due to their incredible properties. Graphene, a single sheet of carbon atoms was the first two dimensional material, and was isolated in 2004. [1] Since then many researchers have worked on ways to prepare this nano material at high yield and high quality. One such method was liquid phase exfoliation of pristine graphite in solvents and was first demonstrated in 2008. [2]The method involves mixing graphite with a specific solvent and ultrasonicating the mixture for a defined period of time. Sedimentation analysis and transmisson electron microscopy (TEM) imaging confirmed that stable, high quality graphene flakes were dispersed, albeit at low concentration (0.01 mg/ml). In order to take full advantage of these graphene flakes, higher concentrations must be achieved. The research presented in this thesis aims to optimise the liquid phase exfoliation process of graphene, and extend all knowledge gained to its inorganic analogue, molybdenum disulphide (MoS_2).

This research begins by increasing the concentration of graphene dispersed two orders of magnitude, up to 1.2 mg/ml. [3] The method involves a long, mild, bath-sonication in the solvent N-methyl pyrrolidinone (NMP), followed by mild centrifugation. Optical absorbance measurements, TEM statistical analysis and Raman spectroscopy, for various sonication times, indicate that while the concentration of graphene increased, the quality of these graphene flakes was maintained.

The flake size distribution within these concentrated dispersions is quite broad, with measured mean lengths between 300 nm and 1 μm. These dimensions are too low for some specific applications. [4, 5] With this in mind, a controlled centrifugation method was demonstrated to take an existing dispersion of graphene and separate constituent flakes by size. [6] Resulting in a set of dispersions with mean flake lengths varying from 1 to 3.5 microns.

These highly concentrated, size separated dispersions have led to a number of advances, including reinforced graphene-polymer composites, however when processing graphene from high boiling point solvents like NMP (202 °C), it can be difficult to fully remove residual solvent. This can present problems in areas such as flake deposition onto a substrate. Alternatively, the direct exfoliation of graphene in low boiling point solvents like isopropanol and chloroform can be advantageous. A dispersion procedure was demonstrated which results in graphene concentrations of up to 0.5 mg/ml in such solvents. [7] To demonstrate the usefulness of this approach, graphene was spray cast onto SiO_2 substrates. Atomic force microscopy of the flakes indicates that they lie flat with minimal aggregation while Raman spectroscopy confirms that they are graphene.

Finally, by extending these optimised preparation procedures to MoS_2 , high quality dispersions of mono and few layer nanosheets were prepared. Again, by prolonged sonication and increased initial concentrations, highly concentrated dispersions of MoS_2 of up to ~40 mg/ml were achieved. [8] Furthermore, re-use of the sediment after centrifugation resulted in dispersions with mean flakes lengths of 2 μm and maximum lengths of between 4-5 μm.

PUBLICATIONS

All research presented in this thesis has been published. The publications containing significant contributions to this thesis have been denoted by **.

1. Cano, Manuela; Khan, Umar; Sainsbury, Toby; O'Neill, Arlene; Wang, Zhiming; McGovern, Ignatius T.; Maser, Wolfgang K.; Benito, Ana M.; Coleman, Jonathan N., Improving the mechanical properties of graphene oxide based materials by covalent attachment of polymer chains. *Carbon* 2013, 52, 363-371.

2. Khan, Umar; May, Peter; O'Neill, Arlene; Bell, Alan P.; Boussac, Elodie; Martin, Arnaud; Semple, James; Coleman, Jonathan N., Polymer reinforcement using liquid-exfoliated boron nitride nanosheets. *Nanoscale* 2013, 5 (**2**), 581-587.

3. Nawaz, Khalid; Khan, Umar; Ul-Haq, Noaman; May, Peter; O'Neill, Arlene; Coleman, Jonathan N., Observation of mechanical percolation in functionalized graphene oxide/elastomer composites. *Carbon* 2012, 50 (**12**), 4489-4494.

4. Sainsbury, Toby; Satti, Amro; May, Peter; O'Neill, Arlene; Nicolosi, Valeria; Gun'ko, Yurii K; Coleman, Jonathan N., Covalently functionalised hexagonal boron nitride nanosheets by nitrene addition. *Chemistry* 2012, 18 (**35**), 10808-10812.

5. Hughes, J. Marguerite; Aherne, Damian; Bergin, Shane D.; O'Neill, Arlene; Streich, Philip V.; Hamilton, James P.; Coleman, Jonathan N., Using solution thermodynamics to describe the dispersion of rod-like solutes: application to dispersions of carbon nanotubes in organic solvents. *Nanotechnology* 2012, 23 (**26**), 265604.

6. Ge, Peiyu; Scanlon, Micheal D.; Peljo, Pekka; Bian, Xiaojun; Vubrel, Heron; O'Neill, Arlene; Coleman, Jonathan N.; Cantoni, Marco; Hu, Xile; Kontturi, Kyosti; Liu, BaoHong; Girault, Hubert H, Hydrogen evolution across nano-

Schottky junctions at carbon supported MoS2 catalysts in biphasic liquid systems. *Chemical Communications* 2012, 48 (**52**), 6484-6486.

7. **O'Neill, Arlene; Khan, Umar; Coleman, Jonathan N., Preparation of High Concentration Dispersions of Exfoliated MoS2 with Increased Flake Size. *Chemistry of Materials* 2012, 24 (**12**), 2414-2421.

8. Khan, Umar; Young, Karen; O'Neill, Arlene; Coleman, Jonathan N., High strength composite fibres from polyester filled with nanotubes and graphene. *Journal of Materials Chemistry* 2012, 22 (**25**), 12907-12914.

9. May, Peter; Khan, Umar; O'Neill, Arlene; Coleman, Jonathan N., Approaching the theoretical limit for reinforcing polymers with graphene. *Journal of Materials Chemistry* 2012, 22 (**4**), 1278-1282.

10. **Khan, Umar; O'Neill, Arlene; Porwal, Harshit; May, Peter; Nawaz, Khalid; Coleman, Jonathan N. Size selection of dispersed, exfoliated graphene flakes by controlled centrifugation. *Carbon* 2012, 50 (**2**), 470-475.

11. Smith, Ronan J.; King, Paul J.; Lotya, Mustafa; Wirtz, Christian; Khan, Umar; De, Sukanta; O'Neill, Arlene; Duesberg, Georg S.; Grunlan, Jaime C.; Moriarty, Gregory; Chen, Jun; Wang, Jiazhao; Minett, Andrew I.; Nicolosi, Valeria; Coleman, Jonathan N., Large-Scale Exfoliation of Inorganic Layered Compounds in Aqueous Surfactant Solutions. *Advanced Materials*, 2011, 23 (**34**), 3944.

12. Khan, Umar; Porwal, Harshit; O'Neill, Arlene; Nawaz, Khalid; May, Peter; Coleman, Jonathan N., Solvent-Exfoliated Graphene at Extremely High Concentration. *Langmuir*, 2011, 27 (**15**), 9077-9082 .

13. Fox, D.; O'Neill, A.; Zhou, D.; Boese, M.; Coleman, J. N.; Zhang, H. Z., Nitrogen assisted etching of graphene layers in a scanning electron microscope. *Applied Physics Letters*, 2011, 98 (**24**), 243117 .

14. Khan, Umar; May, Peter; O'Neill, Arlene; Vilatela, Juan J.; Windle, Alan H.; Coleman, Jonathan N., Tuning the Mechanical Properties of Composites from

Elastomeric to Rigid Thermoplastic by Controlled Addition of Carbon Nanotubes. *Small*, 2011, 7 (**11**), 1579-1586.

15. **O'Neill, Arlene; Khan, Umar; Nirmalraj, Peter N.; Boland, John; Coleman, Jonathan N., Graphene dispersion and exfoliation in low boiling point solvents *Journal of Physical Chemistry C*, 2011, 115 (**13**), 5422-5428.

16. Coleman, Jonathan N.; Lotya, Mustafa; O'Neill, Arlene; Bergin, Shane D.; King, Paul J.; Khan, Umar; Young, Karen; Gaucher, Alexandre; De, Sukanta; Smith, Ronan J.; Shvets, Igor V.; Arora, Sunil K.; Stanton, George; Kim, Hye-Young; Lee, Kangho; Kim, Gyu Tae; Duesberg, Georg S.; Hallam, Toby; Boland, John J.; Wang, Jing Jing; Donegan, John F.; Grunlan, Jaime C.; Moriarty, Gregory; Shmeliov, Aleksey; Nicholls, Rebecca J.; Perkins, James M.; Grieveson, Eleanor M.; Theuwissen, Koenraad; McComb, David W.; Nellist, Peter D.; Nicolosi, Valeria, Two-Dimensional Nanosheets Produced by Liquid Exfoliation of Layered Materials. *Science*, 2011, 331 (**6017**), 568-571.

17. Keeley, Gareth P.; O'Neill, Arlene; Holzinger, Michael; Cosnier, Serge; Coleman, Jonathan N.; Duesberg, Georg S., DMF-exfoliated graphene for electrochemical NADH detection. *Physical Chemistry Chemical Physics*, 2011, 13 (**17**), 7747-7750.

18. Khan, Umar; May, Peter; O'Neill, Arlene; Coleman, Jonathan N., Development of stiff, strong, yet tough composites by the addition of solvent exfoliated graphene to polyurethane. *Carbon*, 2010, 48 (**14**), 4035-4041.

19. **Khan, Umar; O'Neill, Arlene; Lotya, Mustafa; De, Sukanta; Coleman, Jonathan N., High-Concentration Solvent Exfoliation of Graphene. *Small*, 2010, 6 (**7**), 864-871.

20. De, Sukanta; King, Paul J.; Lotya, Mustafa; O'Neill, Arlene; Doherty, Evelyn M.; Hernandez, Yenny; Duesberg, Georg S.; Coleman, Jonathan N., Flexible, Transparent, Conducting Films of Randomly Stacked Graphene from Surfactant-Stabilized, Oxide-Free Graphene Dispersions. *Small*, 2010, 6 (**3**), 458-464.

21. Keeley, Gareth P.; O'Neill, Arlene; McEvoy, Niall; Peltekis, Nikos; Coleman, Jonathan N.; Duesberg, Georg S., Electrochemical ascorbic acid sensor based on DMF-exfoliated graphene. *Journal of Materials Chemistry*, 2010, 20 (**36**), 7864-7869.

Not everything that counts can be counted, and not everything that can be counted counts.

(William Bruce Cameron)

Life is a sum of all your choices

(Albert Camus)

ACKNOWLEDGMENTS

Firstly and foremost I would like to extend my deepest gratitude to my supervisor, Prof. Jonathan Coleman, for this incredible opportunity, and for guiding and inspiring me over the last four years.

I would also like to give special thanks to Umar, Shane and Yenny for always sharing their knowledge and the relentless encouragement, guidance and friendship.

On the first day of my PhD, I was told that a "*PhD is a marathon and not a sprint*", well boy, they weren't lying. I could not have got through the last four years without the wonderful people around me, as the saying goes "*It's not where you are in life, it's who you have by your side that matters*". For that I would like to sincerely thank each and every member that has gone through the Coleman group for support and friendship (in no particular order) : Mustafa, Marguerite, Karen, Phil, Pete, Sophie, Will, Tom, Graeme, Conor, Sebastian, Damien, Ronan, Sukante, Fiona, David, Helen, Evelyn, Damian and by no means least my thesis buddy, Paul. I would also like to greatly thank the members of the Blau and MI groups, specifically Niall, Paula, Darren, Denise, Brian, Anna, Trevor and Eddie and to Prof Valeria Nicolosi for support and EM training in Oxford. A very special thank you must go to those who took time out to read and correct various aspects of this thesis, you know who you are and I am truly indebted to you. Also, to anyone I collaborated with, including Sid, Gar and Peter and to all the summer and final year students that I worked with.

Science communication and outreach are true passions of mine and I am extremely grateful for the opportunities that have been given to me from those from Crann, specifically Diarmuid, Mary and Lia. To all in the school of physics, with special thanks extended to John, Jeanette, Jemmer, Pat, Alan, Nigel, Ken, Robbie, Marie, Ciara and Samantha. A special thank you to those in CMA, Neal, Heath, Amanda and Clodagh. I would also like to thank Danny, Alan, Markus and Prof. Hongzhou Zhang for microscopy training. And by no means least my loving family, Denise, Jim, Rita, Stephen and Dan, and to Ruby and all my friends. Míle buíochas go leor X

CONTENTS

LIST OF FIGURES

1

MOTIVATION AND THESIS OUTLINE

MOTIVATION

Today's materials have very high, multifunctional demands on them. Versatility is essential, with properties such as elasticity, transparency and high conductivity required simultaneously. Nanomaterials can meet such demands, and have the potential to stimulate new technologies for today and *tomorrow*.

Nanomaterial science is a multidisciplinary field, encompassing physics, chemistry, engineering and biology. The field was pioneered by Prof. Richard Feynman, who gave a lecture in 1959, entitled "There's plenty of room at the bottom". During this lecture he foretold the potential of manipulating matter at the atomic scale. With the invention of the scanning tunneling microscope in 1981, [10] and the observing of nanomaterials such as the zero dimensional caged carbon molecule, the buckminsterfullerene in 1985 [11] and the one dimensional single walled carbon nanotube in 1991, [12] nanotechnology attracted a great deal of attention. In 2004, a new low dimensional nanomaterial was isolated; a single sheet of carbon atoms called graphene, and was the first truly two dimensional atomic crystal. [1] Graphene is rich in exceptional physical and chemical properties, offering potential for fundamental research and exciting applications. To that end, it was worthy of the 2010 Nobel prize in Physics, just 6 years after its isolation.

There is arguably no doubt that the nanomaterial age is upon us, but how soon these materials will meet the consumer market will depend upon scalable and reliable ways to prepare these 2D nanomaterials with high quality. Liquid phase exfoliation of layered crystals in solvents offers a way to produce billions of these nanosheets, in a small volume of solvent. It is also a low cost processing option that offers a multitude of advantages like spray deposition or straightforward composite formation, for example.

This preparation technique has also recently been deemed universal. It was shown that ultrasonication in specific solvents can be extended to a range of inorganic layered crystals, each with their own diverse, exotic properties. [13] This offers an avenue to isolate a specific 2D nanosheet, based on the desired properties. The motivation of this thesis was to explore, understand and improve liquid phase processing of graphene and inorganic 2D materials in solvents so more applications of these materials can be realised.

THESIS OUTLINE

Chapter 2: Materials and Background

This chapter begins with discussing two dimensional materials and the unique properties that arise due to their novel geometry. The materials used throughout this research, both graphene and MoS_2 are discussed under the same headings: properties, main production methods and existing and potential applications. The chapter concludes with discussing the opportunities and challenges that face liquid phase processing of 2D materials in solvents.

Chapter 3: Dispersion Theory

This chapter will discuss the theoretical framework for choosing specific solvents that are used to exfoliate and stabilise the two dimensional nanosheets in dispersion. It begins by discussing the energetics of mixing these layered crystals in solvents, which highlights the importance of reducing the enthalpy of mixing. This was shown to be achieved when the surface energy of the solvent is matched to that of the solute. It was also shown that the enthalpy of mixing can be expressed in terms of solubility parameters, indicating once again that they must match that of the solute, to minimise the energetic cost of dispersion. This chapter also discusses Troutons rules which links the boiling point of a solvent to the enthalpy of vaporisation, this in turn is

linked to the cohesive energy density, which is linked to the solubility parameters. The theory behind the stability of nanosheets dispersed in liquids, with specific reference to nanosheets is also discussed.

Chapter 4: Sample Preparation and Characterisation Techniques

In this chapter sample preparation was discussed at length with reference to sonciation and centrifugation. All analysis techniques that were used throughout this research were detailed, with reference to the theory behind its operation and the specific make and model used. UV-Vis NIR spectroscopy, Temporal stability measurements, Raman spectroscopy, electron microscopy and atomic force microscopy were all discussed.

Chapter 5: High Concentration Solvent Exfoliation of Graphene

In this chapter a method was demonstrated to prepare graphene dispersions of up to 1.2 mg/ml in the solvent *N*- methyl-pyrrolidone (NMP). These highly concentrated dispersions were prepared by sonicating the graphite-solvent mixture for long periods of time. Transmission electron microscopy was also used to determine the level of exfoliation and the flakes' dimensions. Statistical analysis of the flake dimensions indicated that they scaled with sonication time as $\frac{1}{\sqrt{t}}$. The data also suggested that the increase in concentration can be correlated to a decrease in flake dimension. While the Raman spectroscopy data indicates that the defect band increases due to an increase in total edge-length to flake area ratio, rather than induced basal plane defects. Free standing graphene networks were also demonstrated as a result of these highly concentrated dispersions.

Chapter 6: Size Selection of Graphene Flakes by Controlled Centrifugation

It was seen in chapter 5, that liquid exfoliation of graphene generally results in flakes with a lateral size of one micron or less on average. This is too small for many

applications. In this chapter, a method was described to separate an existing dispersion, with a mean flake length of ~1 μm, into fractions with different mean flake sizes. The initial dispersion was centrifuged at a high centrifugation rate, separating small flakes in the supernatant from large flakes in the sediment. Redispersion of the sediment, followed by successive centrifugation, separation and redispersion cycles were used to separate the flakes by size, provided the centrifugation rate was decreased with each cycle. This procedure resulted in a range of dispersions with mean flake lengths varying from 1 μm to 3.5 μm for the sample whose final centrifugation rate was 500 rpm.

Chapter 7: Graphene Exfoliation and Dispersion in Low Boiling point Solvent

This chapter discusses the preparation of highly concentrated dispersions of graphene in low boiling point solvents like isopropanol and chloroform. Similar to that discussed in chapter 5, the method involved a long, mild, bath-sonication in volatile solvents. Graphene concentrations of up to 0.5 mg/ml were achieved in such solvents. The main advantage of graphene in volatile solvent systems, is the ease of solvent removal during post processing. To demonstrate this, a graphene sample was spray cast onto an SiO_2 substrate. AFM of the flakes displayed them to lie flat with minimal aggregation, while Raman spectroscopy confirmed the flakes were graphene.

Chapter 8: Preparation of High Concentration Dispersions of Exfolaited MoS_2 with Increased Flake Size

This chapter aimed to optimise the exfolaition of MoS_2 in the solvent NMP. It builds on the research primarily discussed in chapter 5 & 6. In this chapter the yield of dispersed MoS_2 was increased to 40 mg/ml and the lateral dimension of the nanosheets dispersed were increased to ~ 2 μm. These processes relied on prolonged sonication periods and controlled centrifugation of redispersed sediment.

Chapter 9: Conclusions

This chapter summarises all the main data discussed in chapter 5, 6, 7 & 8. It also discusses the future work that I intend to undertake, as a direct consequence of the research presented in this thesis.

2

MATERIALS AND BACKGROUND

2.1 INTRODUCTION

Nanomaterial science has received widespread attention, yielded vast amounts of research effort and resulted in countless publications. However, one class of nanomaterials in particular has shone as a rising star. These are the newest member to the nanomaterial family, two dimensional nanomaterials. Although they are still in their infancy, these materials have demonstrated revolutionary capabilities. This chapter will discuss two dimensional nanomaterials, with an emphasis on graphene and 2D molybdenum disulphide (MoS_2). These two materials will be discussed in further detail under the same headings: properties, main production methods and existing and potential applications. The chapter will conclude with a discussion of the opportunities and challenges that face liquid phase processing of these two dimensional materials in solvent systems.

2.2 TWO DIMENSIONAL MATERIALS

Dimensionality is a crucial factor in determining how a material behaves. Two dimensional nanomaterials are the thinnest form of a three dimensional layered crystal and are arguably the most intriguing and fascinating class of materials ever discovered. In the 1930's, it was theoretically proven that two dimensional materials could not exist in isolation at non zero temperatures. [14, 15] It was thought they would collapse in on themselves forming a curved structure. For some time after, experiments supported the theory, and 2D materials were only thought of as academic materials. [16, 17] Then in the late 60's, the Mermin-Wagner theorem [18] predicted that two dimensional

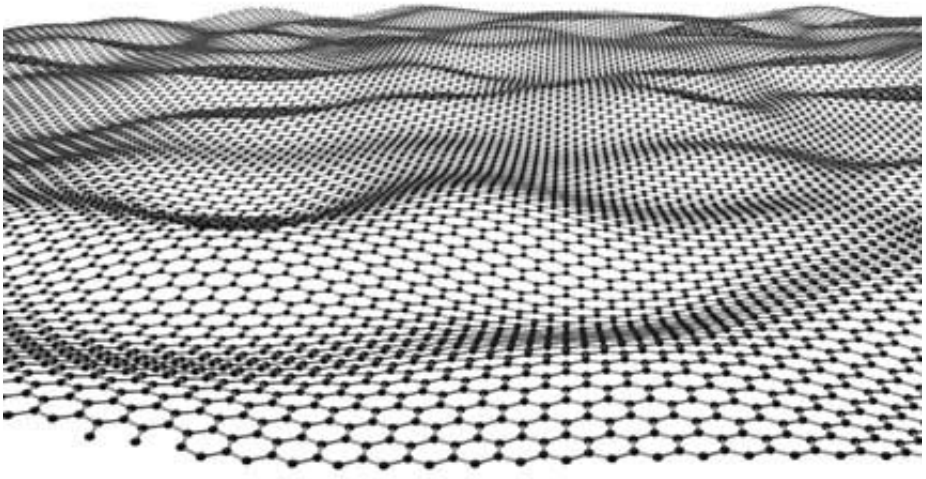

Figure 2.1: Schematic of a suspended graphene sheet displaying thermal fluctuations [19]

materials could exist in 3D space, but would not exhibit long range order due to thermal fluctuations.

In 2004, experimental evidence of the first truly 2D nanomaterial was published, proving that two dimensional materials can exist at finite temperatures. [1] Graphene, a single layer of atoms was isolated from a graphite crystal and upon probing it with and without surface support, it demonstrated exotic properties. [1] These new found phenomena were attributed to the anistropy of its bulk crystal, quantum confinement, geometric effects and surface effects, not to mention differences that arise due to the absence of interlayer interactions. Also, it was found that upon suspending the graphene sheets, ripples at the surface act as a means to stabilise the material, reconciling its existence with thermodynamic stability. The first experimental evidence of stabilising thermal fluctuations was verified by Meyer et al. [19] in 2007 and are schematically depicted in figure 2.1. These structural anomalies termed ripples, were found to reach up to 1 nm in height. Indeed two dimensional, inorganic nanosheets have since been proven to exist and also exhibit unique properties, due to similar aforementioned phenomena. It was also found that 2D MoS_2 was stabilised by thermal fluctuations experimentally found by Brivio et al.. [20]

2.3 GRAPHENE

2.3.1 *Properties of graphene*

Graphite is made up of billions of graphene sheets, Bernel stacked, one on top of the other. Graphene is a one carbon atom thick, monolayer of graphite.

Carbon is one of the most fascinating elements in the periodic table with an electronic configuration of $1s^2\ 2s^2\ 2p^2$ atomic orbitals. In graphene, the 1s electrons are inert and contribute nothing to the chemical bonding. The 2s, $2p_x$ and $2p_y$ orbitals, hybridise to form three planar orbitals called sp^2. These 3 orbitals have 120 degree angle between them and are responsible for the hexagonal lattice structure of graphene, and more notably the strong, covalent chemical bonds between neighbouring carbon atoms. These are sigma bonded and the mechanical properties of graphene are determined by the rigidity of these sigma bonds. The remaining $p_z$orbital contributes one electron for each carbon atom in the lattice. This orbital is perpendicular to the plane formed by the 2s, $2p_x$ and $2p_y$ orbitals and forms a pi-orbital when combined with other p_z orbitals. It is these pi-orbitals that are responsible for graphene's remarkable electronic properties, as when they interact with the periodic potential of the hexagonal lattice, graphene's novel energy spectrum is formed. One can see from its energy spectrum in figure 2.2, that the valence and conduction bands only touch at certain momentum values. These points where they touch are termed the Dirac points. At these Dirac points the density of states is zero at the corresponding energy; therefore graphene is generally termed a semi metal or a zero gap semiconductor.

Another interesting feature seen in the energy spectrum is the conical valleys. [21] Due to graphene having two atoms per unit cell, there are two conical points found at the Brillouin zone edges. Near these points, the valence and conduction band energies vary linearly with the wave vector. [22] This implies that the electrons speed is independent of momentum and behaves similar to photons that travel at constant speed, c. Consequently in order to model the electron dynamics in graphene, the relativistic Dirac equation is required. [23] In this equation, the Fermi velocity of the

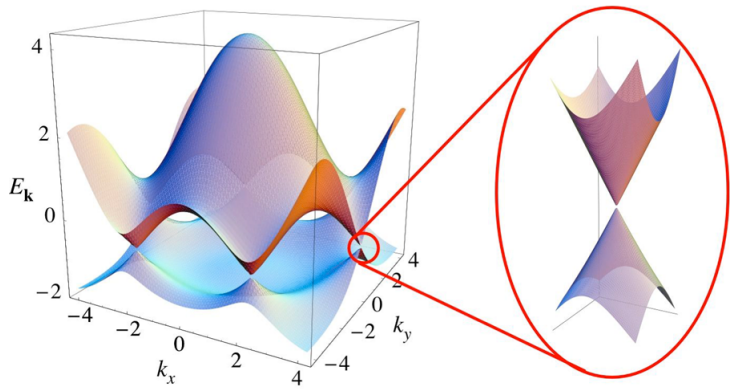

Figure 2.2: The electronic dispersion relation of graphene. [23] The zoomed in image displays the dispersion relation close to one of the Dirac points

massless Dirac fermions of graphene travel 300 times slower than the speed of light, $v_f \sim 10^6$ m/s. Another remarkable property observed was the minimum conductivity displayed even when the concentration of charge carriers tends to zero. This never falls below a minimum value corresponding to the quantum of conductance e^2/h. [24]

As one can determine from the previously discussed properties, graphene has unique electrical characteristics. The charge carriers in graphene behave like massless Dirac fermions at room temperature. [25] This gives rise to ballistic transport properties over several hundreds of nanometres, [1] from which relativistic quantum tunnelling, *the Klein paradox*, and other quantum electrodynamic phenomena can be explored on a bench top experiment. [26–28] Moreover graphene demonstrates ambipolar electric field behaviour, such that charge carriers can be tuned (by doping or local electric fields) continuously between electrons and holes. [23] This creates the possibilities of electrically engineering localised p-n junctions, with high mobilities. Upon isolation it was found that graphene had carrier concentrations as high as 1013 /cm^2 with mobilities exceeding 10,000 cm^2 per volt applied. [1] Bolotin et al. [29] went on to demonstrate an increased mobility of 200,000 cm^2 per volt applied, by suspending the flake between gold contacts thus minimising substrate induced scattering.

Graphene's Dirac fermions also behave in an exotic manner when subjected to magnetic fields, displaying deviations from standard quantum Hall systems. The first Hall conductivity plateau is at half of what is expected, corresponding to a half filled Landau level. After this, all other plateaus follow in the expected integer steps but

are shifted by a half with respect to the normal sequence. [30, 31] This half integer quantum Hall effect can be attributed to graphenes novel linear band structure and the existence of both electronlike and holelike Landau states at zero energy. [32, 33]

In addition to graphene's incredible electrical properties, this material is the strongest ever measured. In 2008, Lee et al. [34] determined the ultimate tensile strength (UTS) and elastic properties of graphene mono- layers suspended across cavities in a SiO_2 wafer. The graphene membranes were indented using a diamond tip cantilever in an atomic force microscope. Their results boast a Young's modulus of 1 TPa and an UTS of 42 TPa. Graphene also demonstrates brittleness, [35] readily folds and can be stretched up to 20% more than any other crystal. [34] Graphene also boasts the highest thermal conductivity (~ 3000 W/m/K) ever reported. [36] It's opacity is defined by fundamental constants. [37] Suspended monolayer graphene absorbs 2.3 % of white light which is defined solely by its fine structure constants. [38] This is a rare situation in condensed matter physics and is attributed to graphene's two-dimensional nature and its gapless electronic spectrum.

Graphene can be considered as the building block for various carbon allotropes, as seen in figure 2.3, and has distinguishing properties that have deemed it an intriguing material. Despite these properties and intense theoretical and experimental interest, widespread implementation of graphene has yet to occur. This is largely due to the difficulty in obtaining a reliable, scalable processing option which is a prerequisite for applications of graphene to flourish. [39]

2.3.2 *Production methods of graphene*

Even though two dimensional materials were thought to be thermodynamically unstable, some scientists continued to investigate how thin they could make graphite planes. Using a refined micromechanical cleavage technique, Geim and co workers peeled a 10 μm sized, two-dimensional graphene from highly oriented pyrolytic graphite (HOPG). [1, 40] Their apparatus consisted of HOPG and scotch tape. This tape was stuck on the graphite and peeled off repeatedly. The graphene were detached from the

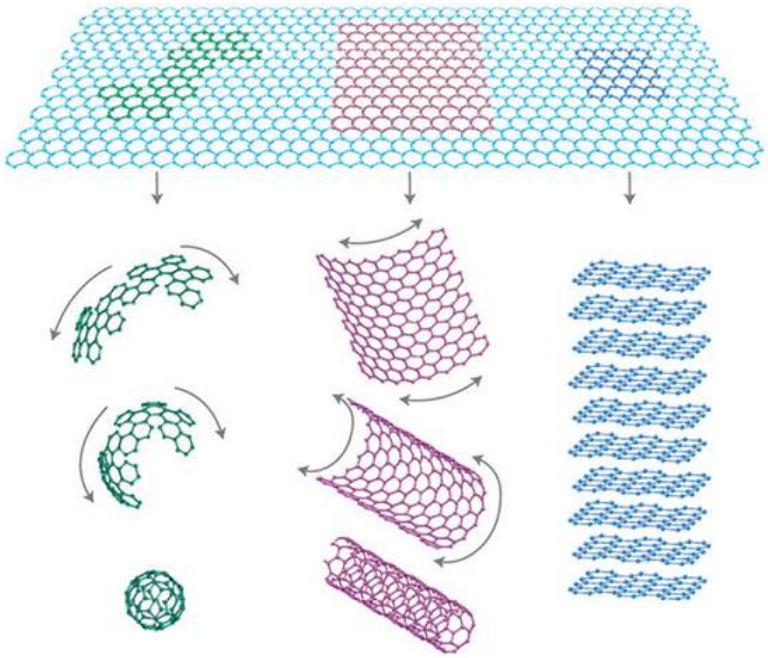

Figure 2.3: Graphene is the building block of all graphitic forms. Graphene is a planar sheets of carbon atoms, that can be wrapped up to form a 0D buckyball, rolled to form a 1D nanotube or stacked to form for 3D graphite. [30]

scotch tape and pinned via van der Waals forces to a Si wafer with a 300 nm oxide layer specifically grown. The graphene was then imaged optically, showing visible contrast on the oxide surface. Next the substrate was etched to minimise induced effects, and graphene's novel intrinsic properties were probed. This original method to produce graphene is delicate, time consuming and not suitable for large scale applications. Residual adhesive glue from the scotch tape can also alter the properties of the flakes. [41] Developments of many processing methods have since become known. They can be broken into three categories, i) growth in situ on a substrate ii) bottom up methods to synthesise graphene from organic precursors and iii) top down methods of liquid phase exfoliation of graphite oxide and pristine graphite. [42]

2.3.2.1 *i) Growth in situ on a substrate*

Graphene mono- and multi- layers have been grown on single crystal silicon carbide (SiC). This process involves heating the SiC to temperatures greater than 1000 °C, in UHV conditions. Si desorbs above this temperature and thus small islands of

graphitised carbon form. A significant advantage of this technique is that SiC substrates offer an insulating supporting medium. Few layer graphene that is produced this way can be patterned using standard lithography techniques thus having potential as a successor of silicon in the post Moore's law era. However, it is challenging to achieve large graphene domains with uniform thickness. Emtsev et al. have tried to overcome this issue by an ex-situ graphitization of Si terminated SiC (0001). [43] This method produces undisturbed monolayer graphene terraces that are up to 3 µm wide and > 50 μm in length. SiC as a supporting medium has also been shown to have appreciable influence on graphene's electrical properties and so must not be made comparable to mechanically cleaved graphene. [44] Zhou et al. found that the interaction between the substrate and the epitaxially grown graphene results in gaps appearing at the Dirac points, which can be exploited to induce a band gap. [44, 45] Band-gap engineering is very encouraging for carbon based electronics, however the high cost of SiC and high temperature requirements are not attractive.

The growth of mono- and few layer graphene on transition metals is also well documented and has established itself as a promising means of production. The procedure involves exposing the transition metal to a hydrocarbon gas, under pressure. This has been demonstrated on Pt [46], Ir [47], Ru [48], Cu [49]and on both Ni single- [50] and poly- crystalline [51, 52] transition metals. There are a lot of requirements for these processing options for example, high temperatures (~700 - 1000 °C) and UHV conditions, not to mention variables like cooling rates and gas phase kinetics. However, an advantage of this processing method is the ability to transfer graphene to a variety of substrates. CVD grown graphene, transferred onto SiO_2, has been shown to exhibit high electron mobilities and even the half integer quantum Hall effect, indicating that the quality can be as high as mechanically cleaved graphene. [52] At present the largest sheet (30 inch diagonal to diagonal) of CVD grown graphene has been demonstrated by Bae et al.. [53] This unique method involves using a 7.5 inch wide quartz tube wrapped in copper foils that is inserted into an 8 inch wide furnace. After oven processing the graphene is transferred to an adhesive polymer support and the copper is etched, which is a complicated, expensive process . The graphene films are then transferred from the polymer support onto a target substrate by removing the adhesive forces. The

resulting graphene films have set the bar for transparent conductive electrodes with a sheet resistance of ~40 Ω sq^{-1} and a transparency at 550 nm of ~90%, however only over small areas.

Although these films [53] are ready for use in transparent conductive coating applications, this processing option is very expensive and has large energy requirements. There are also improvements to be made to the transfer process, grain size, crystallographic orientation and layer thickness. However when these improvements are met, this processing option has huge compatibility advantages with current microelectronic technologies. Thus the inclusion of graphene will be less disruptive and more cost effective than perhaps other processing options. [9]

2.3.2.2 *ii) Bottom up methods to synthesise graphene from organic precursors*

Bottom up synthetic approaches using benzene-based macromolecules have been known for some time. [54, 55] They are referred to as polyaromatic hydrocarbons (PAHs) and they lie between molecule and macromolecule structures. The arrangement of the benzene rings is very similar to the 2D chicken wire structure of graphene and has thus attracted attention as a possible route for controlled growth of graphene on substrates. PAHs are also attractive due to their versatility, their clean processing and the multitude of aliphatic chains that can be attached to modify their solubility. [56] These routes have been largely explored by Mullen and co- workers who have produced a number of graphene precursors. The main disadvantage of increasing the molecular weight of these planar structures is that their solubility in common solvents decreases, complicating their processability. The core molecule in molecular graphene is the hexabenzocoronene (HBC), which consists of 13 fused hexagon rings. This molecule became the building block along with other hexaphenylbenzene derivatives. The largest graphene molecules arranged to date has 222 carbon atoms in its core. [57] Further advances came in 2008, when Yang et al.[58], demonstrated total synthesis of graphene nanoribbons (GNRs) (their advantage is discussed in the application section) with controlled edge configuration. The electrical properties of these GNRs were characterised by scanning tunnelling microscopy (STM), and thin films were prepared showing liquid crystal properties. Also recently, the exfoliation and dispersion

of HBC was demonstrated in 28 different organic solvents by Hughes et al., [59] where it was found that successful solvents were characterised by similar Hildebrand solubility parameters to graphene. Furthermore, organic synthesis of graphene offers an alternative route to synthesising graphene with defined shape, size and edge structure, factors that are quite important for applications that require a finite band gap and edges that allow spin transport.

2.3.2.3 *iii) Top down methods of liquid phase exfoliation of graphite oxide and pristine graphite*

Dispersing graphene in solution requires overcoming the cohesive energy of the graphite planes. [60] To overcome this energy barrier, two main methods have emerged. The first requires the chemical functionalisation of graphite which aims to weaken interlayer interactions [61] and the second involves the sonication of untreated graphite in solvent [2] or surfactant systems. [62]

The first approach results in graphite oxide (GO). This is a product of the oxidation of graphite which results in the decoupling of individual graphene layers but retains the original graphite layered structure. [63] The principle method to oxidise graphite is the Hummers method, [61] and involves dispersing graphite in concentrated sulphuric acid, sodium nitrate and potassium permanganate at 45 °C for a few hours. The resulting graphite intercalation compounds are then rapidly annealed, generating a CO_2 over-pressure that causes the graphite to split. Further ultrasonication results in individual GO sheets. These GO sheets contains large quantities of hydroxyl, carboxyl, carbonyl and epoxide functional groups which are attached to the edge or basal planes. [64] Undesirably during the oxidation processing, the carbon atom is transformed from a planar sp^2 hybridised geometry to a distorted sp^3 hybridised geometry, thus changing its electrical properties to become electrically insulating (see figure 2.4). Attempts to restore the electrical conductivity are performed by means of a hydrazine or hydrogen plasma reduction.

GO is strongly hydrophilic and can be readily exfoliated in water to form stable colloidal dispersions at 2 mg/ml. [65] Further dispersion analysis confirmed that single layer GO sheets, up to hundreds of microns in size, have been dispersed in a variety

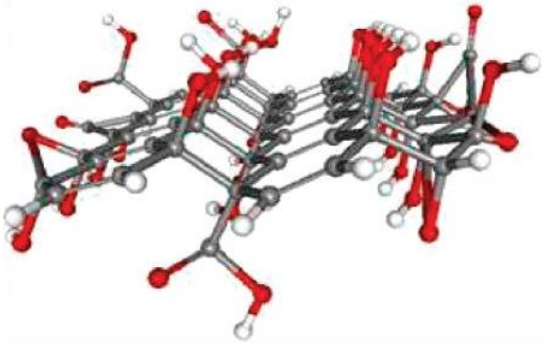

Figure 2.4: Graphene oxide structure demonstrating the distorted sp^2 atomic arrangement with attached functionalities (left) and vial of GO brown dispersion (right). Its brown colour is attributed to the absence of π conjugated structure.

of organic solvents at concentrations of $\approx$ 2 mg/ml. [66–69] Notably, Ang et al. [70] obtained stable dispersions with 90% monolayer yield and mean sheet areas of 330 $\pm$ 10 μm^2. They explained that intercalated GO sediments formed after oxidation, via a modified Hummers method, result in oxidised outer layers of the large sized GO aggregates, but the inner layers consist of mildly oxidised (mainly at the edge planes) graphene sheets. These sediments were then intercalated using tetrabutylammonium hydroxide, (TBA, 40 % water) under reflux conditions for two days. After two days the colour changes from pale yellow to black indicating an increase in UV-Vis absorption region due to the presence of extended conjugate π structure. [71] They were then dispersed in dimethylformamide (DMF) and spin coated onto SiO_2. Their XPS data suggests that less that 10 % of the carbon remains oxidised and a conductivity of 15,000 S/m was measured. Dikin et al. prepared free standing (1 to 30 μm thick) GO paper showing a mean Youngs modulus of 32 GPa and ultimate tensile strength of 60 MPa. [72] These results are greater than most of the reported nanotube bucky papers. [73] Despite increased processability of graphene oxide, it retains significant amounts of oxygen functionalities even after severe reduction processes and can contain irreversible lattice defects. [69] In comparison to mildly defective graphene derived from expanded graphite, it fails to meet the high electrical conductivities due to distorted sp^2 structure and contains many lattice defects. [74–76]

The other mentioned approach to overcome the forces that bind graphene layers together, is liquid phase exfoliation of pristine graphite in solvent and surfactant

systems. Solvent exfoliation of graphite was first demonstrated by Hernandez et al. [2] and concentrations of up to 0.01 mg/ml were achieved. It was found that ultrasonication of graphite in solvents with solubility parameters in a defined range, will result in graphene flakes of varying thickness and dimension stabilised against re-aggregation. Further centrifugation post sonication, was found to result in an increased fraction of thinner flakes in the dispersion. Others, working with similar approaches have yielded dispersions of graphene between 0.05 and 0.1 mg/ml [77, 78]. While exfoliation in ionic liquids has yielded concentrations as high as $\sim$ 5 mg/ml. [79] Surfactant aided aqueous dispersions of graphene have also been prepared, [62] with concentrations of up to 0.3 mg/ml achieved. [80] Since then the concentration of dispersed graphene in solvents has been improved and will be discussed at length in chapter 5 and 7. Also the advantages and challenges of this processing option are discussed later in this chapter.

2.3.3 *Applications of graphene*

From the unique properties of graphene stems a whole wealth of noteworthy applications. For example, graphene's surface area to volume ratio and low intrinsic noise, has offered atomic sensitivity in sensors. [81] These in combination with the fragility of a single point contact makes the band structure of graphene highly sensitive to any change, such as external electric fields, mechanical deformations, doping and adsorbates, which are also desirable for sensing applications. Graphenes' theoretical surface area is 2630 m^2 per gram and its high energy storage density, making it a suitable candidate for ultracapacitors and batteries. [82, 83] The chemistry of graphenes basal plane must also be mentioned, as although it is a chemically inert material , nanometre scale reactivity can be found in localised regions at its surface, which arise because of the ripples. This allows for spatial control of chemical functionalisation at these regions and can lead to a range of applications. For example, a metal to insulator transition at a desired location, and the tuning of the flakes mechanical properties by the incorporation of analyte specific lock and key type binding. [84] The absence of

a band gap in graphene also allows for a vast number of electronic transitions, over a large portion of the electromagnetic spectrum [85] indicating the wealth of potential applications in electronic-photonic devices. Graphene has many applications in electronics including transparent conductive coatings for flexible touch screen displays and faster, smaller transistors consuming less energy and dissipating heat faster than silicon based devices. Finally graphene based polymer composites have exhibited low electrical percolation thresholds (0.1 vol%) [86] and high tensile strength and thermal conductivity. [87]

These are but a few applications of graphene, that can stem for its superlative properties. For more applications to flourish a large scale production method must be found. However, in the near term, top down methods of liquid phase exfoliation of graphene have manifested themselves as a viable route for graphene production.

Graphene is also limited with no band gap, thus restricting its use in some applications. However, attempts have been made to overcome this, for example preparation of graphene nanoribbons. [88] However, this adds complexities to the processing and in some cases can reduce graphene's high mobility. A more ideal approach would be the use of two dimensional nanosheets that are semiconducting.

2.4 TRANSITION METAL DICHALCOGENIDES - MOLYBDENUM DISULPHIDE

Molybdenum disulphide (MoS_2) is the most stable member of the transition metal dichalcogenide (TMDs) compound family. TMDs have an MX_2 stoichiometry, where M is a transition metal atom and X are the chalcogen atoms, illustrated in the schematic at the bottom of figure 2.5. There are approximately 60 different compounds ranging from insulators (eg. HfS_2) to semiconductors (eg. MoS_2) to superconductors (eg. TaS_2), depending on the metal - chalcogen combination (see figure 2.5). [89] In addition each material displays unique novel properties, making them applicable to a whole wealth of material limited technologies like thermoelectrics and supercapacitors, for example. To date MoS_2 is probably the most studied TMD, as it is seen as the semiconducting

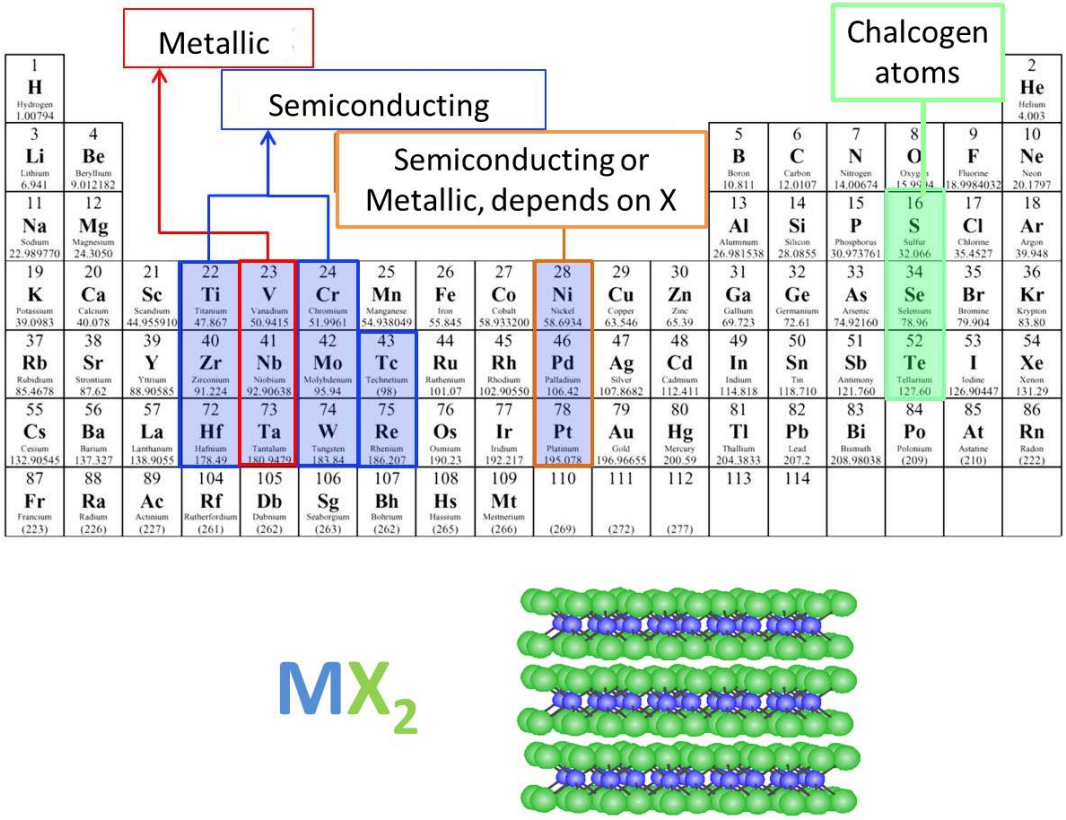

Figure 2.5: Periodic table, with highlighted regions indicating the transition metals (blue) and the chalcogens atoms (green). Under the periodic table is a stick and ball model, demonstrating the MX_2 stoichiometry.

analogue of graphene, however plenty of further research is required to improve processing methods and explore more applications.

2.4.1 *Properties of MoS_2*

MoS_2 comes from a naturally occurring mineral called Molybdenite. This compound consists of hexagonal stacked nanosheets, where each individual nanosheet is three atoms thick. The nanosheet itself is then made up of a metal molybdenum atom (M), sandwiched between chalcogon sulphur atoms (X), giving a monolayer structure of MX_2. As already mentioned, the atoms that make up each nanosheet are bound covalently to one another, while out of plane, the interlayer sulphur - sulphur bonds are loosely held together by weak van der Waals forces that have a strength of about 3

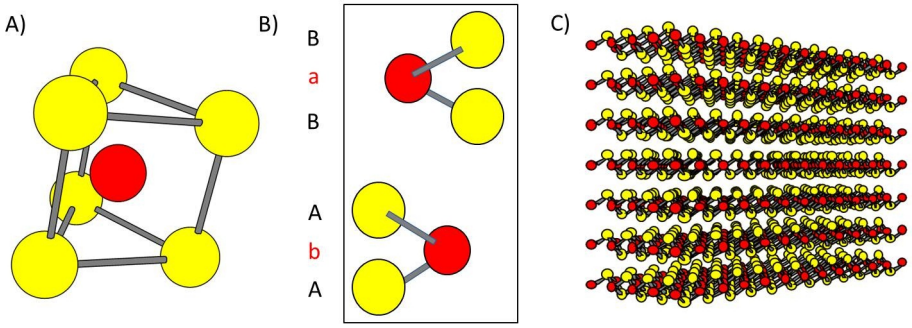

Figure 2.6: A) A schematic of a trigonal prism with the Mo atoms in red and the S atoms in yellow. Each trigional prism joins to form a monolayer in plane while out of plane it stacks with a AbA, BaB where A, B are chalcogen atom layers and a, b are Mo atom layers

% that of the intralayer binding forces. Interlayer, each Mo atoms occupies the centre of a trigonal prismatic structure with 3 equidistant sulphur atoms bound to the top and bottom, as seen in figure 2.6A. Each trigonal prism is then stacked one on top of the other with an interlayer spacing of 0.62 nm, a monolayer height of 0.67 nm and an AbA BaB stacking sequence (as seen in figure 2.6B & C) giving the crystal its layered structure. The hexagonal arrangement of MoS_2 indicates that it is 2H phase with two monolayers per unit cell.

MoS_2 in its bulk form, is a semiconductor with an intrinsic indirect bandgap of 1.29 eV and an electrical conductivity of 1.58 x 10^{-4} Ω cm^{-1}. [38] However, when a monolayer of MoS_2 is isolated, it becomes a direct bandgap semiconductor with a bandgap of 1.8 eV [90] that demonstrates strong photoluminescence as a result of quantum confinement. [91] MoS_2 has also demonstrated thermal stability up to 1100 °C and good mechanical properties, with a high Youngs modulus. Early measurement of bulk MoS_2, indictaed it has a Youngs modulus of E_{bulk} = 0.24 TPa, [92] while more recently, suspended nanosheets of MoS_2 have been shown to have a Youngs modulus of E = 0.33 ±0.07 TPa. [93] These compare favourably with graphene, the strongest material ever discovered, which has a Youngs modulus of E = 0.8 – 1.0 TPa. [34]

2.4.2 *Production methods of MoS_2*

The weakly bound layered structure of MoS_2 has encouraged scientists to try split the bulk crystal into individual monolayers for many years, even though at the time it was unclear whether or not free standing monolayers could exist. Similar to graphite, intercalation was one of the first methods to try prepare monolayer MoS_2. The process involved inserting various bulky intercalation ions, like tetrabutylammonium (TBA) between the layers. [94] Water was also sometimes added to create hydrogen to further separate the layers. [95] The materials prepared were characterised using X-ray diffraction, which gave no indication of how thin the nanosheets were exfoliated. [95, 96] They did however determine that they had created a metastable phase of the exfoliated MoS_2, changing the metal coordination from a trigonal prismatic (2H) to a metastable octahedral geometry (1T). This undesirable change in crystal symmetry resulted in a different electronic structure, [97] and structural distortions. [98, 99] The method itself was also time consuming and extremely sensitive to environmental conditions. More recently efforts have been made to improve on the traditional intercalation methods, with some noteworthy successes published by Eda et al. and Zeng et al.. [100, 101] Monolayers of MoS_2 were prepared however complete restoration of the 2H phase was not fully achieved.

Another successful technique to isolate monolayers of MoS_2 was by micromechanically cleaving the bulk MoS_2 crystal. Individual monolayer sheets were confirmed using AFM and Raman spectroscopy. [38, 40, 102] Similar to graphene, the MoS_2 nanosheets were deposited onto an oxidised Si wafer and an estimate of the level of exfoliation was determined optically, by observing their colour interference on the substrate. [40, 103, 104] This preparation method yields high quality 2D crystals, however future applications will require the development of new processing options that will overcome the low yield and slow processing associated with this technique.

The next approach that became a viable route to prepare 2D nanosheets of layered TMDs and other layered crystals, like boron nitride (BN) for example, was demonstrated in 2011 by Coleman et al. [13]. This research was an extension of liquid phase

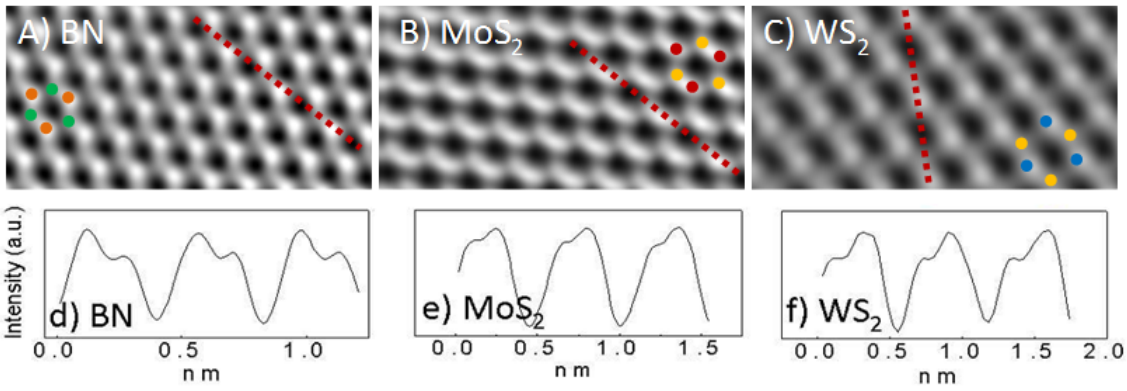

Figure 2.7: Butterworth - filtered HRTEM images of section of a A) BN, B) MoS_2 and C) WS_2 nanosheet and D-F) are their corresponding intensity distributions along their respective dotted lines. Image taken from Coleman et al. [13]

exfoliation of graphene in specific solvents and demonstrates the exfoliation of layered crystals in common solvents. This approach provides a scalable mixture of single and multi layered flakes of various materials. Seen in figure 2.7, are high resolution TEM images of a A) BN, B) MoS_2 and C) tungsten disulphide (WS_2) monolayers, displaying the defect free, hexagonal structure of flakes after exfoliation by ultrasonication in solvent. Further optimisation of liquid phase processing of MoS_2 nanosheets will be discussed in chapter 8.

Since then there have been a number of bottom up processing options to prepare large areas of crystalline MoS_2 thin films. Some of these approaches are more compatible with current device technologies and will result in the integration of MoS_2 into future device applications. For example, they have been grown by thermal decomposition of benzenethiol salts on Cu(111) by Kim et al., producing exclusively monolayer MoS_2, that are typically tens of nms in dimension. [105] Also Liu et al. [106] have demonstrated the growth of large area and highly crystalline MoS_2 thin layers on insulating substrates, by high temperature annealing of thermally decomposed ammonium thiomolbdate layer in the presence of sulphur. Using the same precursor, graphene grown on Cu (111) was shown to act as a good growth template for monolayers of MoS_2, up to several microns long. [107] Chemical vapour deposition (CVD) of MoS_2 onto amorphous SiO_2 substrates has been demonstrated. [108] These films were prepared using MoO_3 and S powder as the reactants and consist of mono to few

layer MoS_2. Large scale vapour phase growth has also been demonstrated, producing mono- and multi layers of MoS_2 on SiO_2 substrates. [109] However similar to graphene, generally these bottom up preparation routes require a lot of chemical reactants, high temperatures, UHV conditions, but to mention a few parameters.

All preparation techniques discussed in this section still require further development to optimise the quality, yield and size of the MoS_2 nanosheets. Of note, some processing options will be more suited to specific industries for specific applications.

2.4.3 *Applications of MoS_2*

MoS_2 has been shown both theoretically [110] and experimentally [13] to have exceptional properties that can be exploited in many fields. A monolayer of MoS_2 has been shown to demonstrate superior performances in nanotribology, hydrogen production, gas sensors and solar energy production. Most recently, the use of a monolayer MoS_2 as the gate channel in a field-effect transistor (FET) with hafnium dioxide as the gate insulator layer was demonstrated. This combination demonstrated some excellent results with channel mobilities of up to 200 $cm^2\ V^{-1}\ s^{-1}$ and on/off ratios of more than 10^8, proving itself as a promising replacement for silicon in a FET. [102] Monolayer MoS_2 also exhibits strong photoluminesence, centred at 676 nm. [91] An increase in luminescence quantum efficiency was observed with decreasing MoS_2 layer thickness, with a 1000 fold increase in luminescence efficiency found for monolayers. [38, 91] MoS_2 also appears to be promising for optoelectronic device, [111] solar cells, and light-emitting diodes. MoS_2 nanosheets with their large intrinsic bandgap can also be useful in flexible semiconducting devices. With their high Youngs modulus and toughness, they can withstand deformations up to tens of nanometers elastically without breaking. [93, 112] Smith et al., [113] also found that by preparing MoS_2 only and MoS_2/single walled nanotubes (SWNTs) hybrid electrodes, they displayed a higher rate capability and higher retained capacity over 100 cycles when compared to MoS_2 only electrodes (100 mAh/g *versus* 200 mAh/g). Du et al. [114] also demonstrated that

restacked MoS_2 exhibited a higher lithium storage capacity of 850 mAh/g at 50 mA/g and good cycle stability as a Li-ion battery electrode.

2.5 LIQUID PHASE PROCESSING, OPPORTUNITIES AND CHALLENGES

Opportunities

The processing option chosen for the duration of this research are based on liquid phase exfoliation by ultrasonciation, of pristine bulk crystals in specific solvents. This approach is straightforward with easily controlled parameters. It is also readily accessible with a low cost. When successful dispersions were prepared, they can be directly mixed or blended with polymers or other nanomaterials to prepare hybrids. It is also very easy to spin or dip coat, filter, print or spray these dispersions. The nanosheets can also be easily post treated, with functionalities for example. This process is also reliable and scalable to meet industrial volume requirements and has proved itself universal for layered crystals, with only slight optimisation required for each different material.

Challenges

The main drawback however, is the lack of control over the level of individual flake exfoliation and unavoidable sonication induced scission. These effects can vary considerably even within a dispersion and can lead to unpredictable results with inferior properties. To try minimise this polydispersity, a centrifugation step can be used to narrow the flake thickness and size distribution. It was also found that by recycling and redispersing the sediment and controlling the centrifugation, groups of flakes dimensions can be isolated from the polydispere dispersion and will be discussed further in chapter 6 and 8. Ultracentrifugation of the dispersion in a density gradient medium has also been demonstrated by Green et al.. [115] This sorts graphene sheets according to their buoyant density and has produced mono-disperse graphene disper-

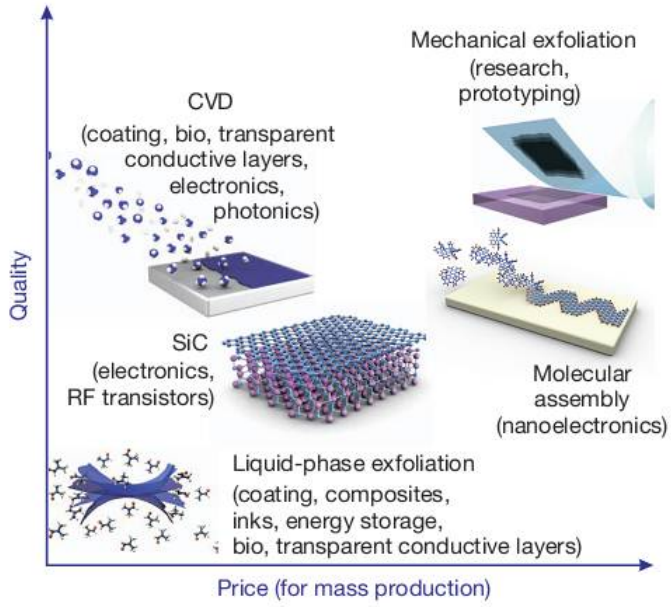

Figure 2.8: Scalable graphene production options [9]

sions. Column chromatography of solution processed nanosheets is also another route to prepare dispersions of flakes with specific lateral dimensions, [66, 116] however this can be quite time consuming.

2.6 CONCLUSIONS

This chapter discusses the unique properties of two dimensional materials. The chapter focuses on discussing graphene, the first two dimensional material and MoS_2, its inorganic analogy. Both materials theoretically and experimentally display unrivaled intrinsic capabilities, and will significantly advance specific material based technologies. The various processing options discussed in this chapter can be summarised in figure 2.8. One can see that although liquid phase exfoliation is a low cost, scalable processing option, it suffers from reduced quality nanosheets. However, this low quality refers to small flake dimensions and increased thickness rather than induced defects, which is promising. This thesis aims to improve upon current solvent exfoliation techniques to improve the overall quality of the two dimensional nanosheets dispersed.

3

DISPERSION THEORY

3.1 INTRODUCTION

Before two dimensional nanomaterials were ever isolated, the liquid phase dispersion of carbon nanotubes had been well explored, in particular the exfoliation of individual carbon nanotubes using solvents. [117–119] It was shown that the driving factor in nanotube exfoliation was the strength of the solvent-nanotube sidewall surface interactions. In particular, it was seen that if the surface energies of nanotube and solvent matched closely, dispersion would be successful, in accordance with the solubility chemistry phrase "like dissloves like". Consequently, since the surface energy of carbon nanotubes is close to that of graphite, it was proposed that successful nanotube solvents could also be used to exfoliate graphene from graphite. Hernandez et al. performed the first experiments to investigate this in 2008. [2] The results indicated that indeed, solvents with similar surface energies to the surface energy of graphite resulted in favourable exfoliation of graphite into graphene. [2, 120]

In 2011, it was seen that this approach could be universally applied when transition metal dichalcogenides (two dimensional nanosheets) were exfoliated in specific solvents with surface energies that matched the surface energy of the solute. [13] This chapter will discuss the theoretical framework for choosing these specific solvents. It will begin by discussing the energetics of mixing nanosheets in solvents, from a thermodynamic perspective. This will lead us into breaking the interactions down and discussing solubility parameters. Then, finally, the theory governing the stability of the solvent-solute mixtures will be discussed, with specific reference to two dimensional nanosheets.

3.2 SOLUTION THERMODYNAMICS

The thermodynamics of a mixture are governed by the Gibbs free energy (ΔG_{mix}), which is a function of enthalpy of mixing (ΔH_{mix}), absolute temperature (T) and entropy of mixing (ΔS_{mix}).

$$\Delta G_{mix} = \Delta H_{mix} - T\Delta S_{mix} \tag{3.1}$$

Mixing is favourable when ΔG_{mix} is negative or close to zero. For this to occur at room temperature, a large entropic and/or a small enthalpic term is required. Assuming that the ΔS_{mix} of the system is low due to the nanosheets being rigid and relatively large, the ΔH_{mix} must therefore be minimised. A calculation for ΔH_{mix} , indicating the factors that can be controlled to minimise ΔH_{mix} was derived for graphene [2], with the following outcome

$$\frac{\Delta H_{mix}}{V_{mix}} \approx \frac{2}{T_{flake}} \left(\sqrt{E_{surf}^{solvent}} - \sqrt{E_{surf}^{solute}} \right)^2 \phi \tag{3.2}$$

where $\sqrt{E_{surf}}$ is the square root of surface energy for the solute or solvent , T_{flake} is the flake thickness and ϕ is the solute volume fraction ($\frac{V_{solute}}{V_{mix}}$). This formula was rederived specifically by Herandez et al.. [2] This analysis showed that the $\triangle H_{mix}$ term was minimised when the surface energy of the solvent was matched to the surface energy of the solute. The surface energy of the solvent can be related to its surface tension (γ) as follows

$$\gamma = E_{surf}^{solvent} - T\, S_{surf}^{solvent} \tag{3.3}$$

where $S_{surf}^{solvent}$ is the surface entropy and is a generic value close to 0.1 $mJ/m^2/K$ for common CNT and graphene amide solvents. [118] Equation 3.2 expresses $\frac{\Delta H_{mix}}{V_{mix}}$ in terms of the difference between $E_{surf}^{solvent}$ and E_{surf}^{solute} . When the surface energy of the solute and solvent are matched, this will result in a minimal net energy cost. And thus a small $\frac{\Delta H_{mix}}{V_{mix}}$ term in equation 3.1, coupled with a small $\triangle S_{mix}$ contribution, suggests in turn that a mixture is thermodynamically favorable.

In the above mentioned approach, matching the solute and solvent surface energy was successful at highlighting good solvents but not all of the solvents whose surface

energy matched that of the solute (68 mJ/m^2) were successful. Perhaps this is because this approach relies on a rather crude summation of energetic terms.

In the 1930s , a theory was developed by Flory and Huggins to describe the solubility of polymers. This theory considered three main interactions which are responsible for determining whether mixing occurs: the solute-solute, solvent-solvent and solute-solvent interactions. [121] Assuming that the solute and solvent molecular volumes are similar and the molecules are small, inter-molecular pairwise interactions, ε, between the solute (A) and the solvent (B) can be accounted for by the so-called Flory-Huggins parameter χ, [122]

$$\chi = -\frac{z}{2}\frac{(2\varepsilon_{AB} - \varepsilon_{AA} - \varepsilon_{BB})}{kT} \tag{3.4}$$

where z is the coordination number for both the solvent and solute. A relationship between the Flory-Huggins parameter χ and the enthalpy of mixing per unit volume $\Delta\bar{H}_{mix}$, can be derived, leading to this expression [122],

$$\Delta\bar{H}_{mix} = \frac{\chi\phi(1-\phi)\,kT}{v_0} \tag{3.5}$$

where χ is dimensionless, ϕ is the solute volume fraction, and v_0 is the solvent molecular volume. The enthalpy of mixing is required to be small or negative for mixing to occur, and equation 3.5 shows that χ must also be small or negative for this condition to hold. Inspecting equation 3.4, it can be seen that this is satisfied when solute-solvent interactions dominate.

It can be noted that χ exactly describes intermolecular interactions (unlike the previous model, which only permitted positive or zero values for mixing), however the drawback is that it is difficult to measure in practice. Therefore in the following section, methods are discussed to improve the accuracy of the original model.

3.3 SOLUBILITY PARAMETERS (δ)

$\Delta\bar{H}_{mix}$ can also be expressed in terms of solubility parameters. Solubility parameters are a means to assess how good a solvent will be at dissolving a specific solute. There

are a range of solubility parameters including, for example surface tension, surface energy, refractive index and Hildebrand solubility parameters, δ_T. The most commonly used solubility parameter is the Hildebrand solubility parameter, which can be derived from the vaporisation energy of the solute or solvent, and is related to the total cohesive density $E_{C,T}$ by

$$\delta_T = \sqrt{\frac{E_{C,T}}{V}} \tag{3.6}$$

where V is the solvent molar volume. Using the expression for $\Delta\bar{H}_{mix}$ in equation 3.5, we can also derive the Hildebrand-Scratchard expression. This expresses $\Delta\bar{H}_{mix}$ in terms of Hildebrand solubility parameters, where $\delta_{T,A}$ and $\delta_{T,B}$ are the Hildebrand solubility parameters of the solute and solvent respectively.

$$\Delta\bar{H}_{mix} \approx (\delta_{T,A} - \delta_{T,B})^2 \phi(1-\phi) \tag{3.7}$$

It should be noted that this has a similar form to equation 3.2, where the difference between the two energetic forms dominates the $\Delta\bar{H}_{mix}$ for the interacting species. δ_T was shown to depend on the dispersive, polar and hydrogen bonding terms by Hansen according to equation

$$\delta_T^2 = \delta_D^2 + \delta_P^2 + \delta_H^2 \tag{3.8}$$

where δ_D, δ_P and δ_H are the dispersive, polar and hydrogen bonding solubility parameters respectively. Based on equation 3.8, equation 3.7 can be expanded for the enthalpy of mixing as follows

$$\Delta\bar{H}_{mix} \approx \phi\,(1-\phi)\left[(\delta_{D,A} - \delta_{D,B})^2 + (\delta_{P,A} - \delta_{P,B})^2 + (\delta_{H,A} - \delta_{H,B})^2\right] \tag{3.9}$$

This implies that all three solubility parameters of the solvent must match those of the solute to minimise the energetic cost of dispersion.

The cohesive energy density and the respective Hansen/ Hildebrand parameters are difficult to measure for solutes, since solids don't vaporise easily. However there are a wide range of experimental and calculated values available for materials such as graphite. [119] However E_{surf}^{solute} was found to have a wide range of values depending

on how measured and calculated. By comparison, there exists a vast collection of these values for solvents.

Solute parameters can however, be estimated by inspecting the correlation between the dispersed solute concentration and the solvent solubility parameters. Intuitively, if successful solvents have parameters matching those of the solute, they should also facilitate the dispersion of material. In fact recently a relationship between the enthalpy of mixing and the maximum dispersed concentration was derived by Hughes et al.[123] to be :

$$C \propto exp\left[-\frac{\bar{v}}{RT}\frac{\delta\left(\Delta H_{mix}/V\right)}{\delta\phi}\right] \tag{3.10}$$

where $\bar{v}$ is the molar volume of the solute. Applying this to disks and substituting equation 3.2 into equation 3.10, this predicts the concentration of dispersed nanosheets to be described by

$$C_{nanosheet} \propto exp\left[-\frac{\pi(L/2)^2}{8\,E_{surf}^{solvent}kT}\left(E_{surf}^{solvent}-E_{surf}^{solute}\right)^2\right] \tag{3.11}$$

where $\frac{L}{2}$ is half the longest axis of the nanosheet. It has been confirmed for both graphene and MoS_2 that successful solvents show a Gaussian dependence on solubility parameters. Sometimes, the data can be quite scattered, with many solvents showing dispersed concentrations below the predicted envelope function. [124]

It was found that good solvents for graphene and MoS_2 are characterised by Hildebrand solubility parameters $\delta_{T,Gr} \approx 23$ MPa$^{1/2}$ [120] and $\delta_{T,MoS_2} \approx 22$ MPa$^{1/2}$. [124] Specific physical interactions between the solvent and graphene were subsequently investigated using Hansen parameters. The effectiveness of the studied solvents was shown to scale with proximity to the calculated Hansen solubility parameters for graphene as $\delta_D \approx 18$ MPa$^{1/2}$, $\delta_P \approx 10$ MPa$^{1/2}$ and $\delta_H \approx 7$ MPa$^{1/2}$ and for MoS_2 as $\delta_D \approx 17.8$ MPa$^{1/2}$, $\delta_P \approx 9$ MPa$^{1/2}$ and $\delta_H \approx 7.5$ MPa$^{1/2}$.

3.3.1 *Trouton's rule*

Trouton's rule is an approximation rule for the derivation of the enthalpy of vaporisation for a liquid $\Delta H^{\ominus}_{vap}$, at its boiling point. Thus it can be seen that the boiling point of the solvent can provide a reasonable indication to how successful it will be at preparing a high concentration, well exfoliated dispersion. Trouton's emperical rule links the boiling point (T_B) of the solvent to the enthalpy of vaporisation;

$$\Delta H^{\ominus}_{vap} \approx \Delta S^{\ominus}_{vap} \times T_B \approx constant \times T_B \tag{3.12}$$

where $\Delta S^{\ominus}_{vap}$= 80 J/K/mol for most solvents. [125] Thus it can be shown that the boiling point provides an indication of the cohesive energy density by

$$\Delta E_{vap} = \Delta H^{\ominus}_{vap} - RT \tag{3.13}$$

and this in turn is related to the Hildebrand solubility parameter, which indicates quantitatively how successful a solvent will be at exfoliating a solute.

3.4 DISPERSION STABILITY

Thermodynamically, all dispersions are unstable and eventually all the dispersed material will sediment under the gravitational field. There is however a measurable period of time where the dispersion demonstrates a quasi-stablility. This quasi-stability is partly controlled by the solute-solvent interactions and can be determined by monitoring the optical transmission through a dispersion as a function of time. This data can be normalised and used to highlight the amount of quasi stable material, their time constants and the number and amount of unstable phases in the dispersion (post-centrifugation). [126]

According to sedimentation theory, [127–129] the concentration of a non-soluble phase sedimenting out of a liquid is given as a function of time t by

$$C(t) \propto C_n exp\left[-\frac{g^2\left(\rho_s - \rho_l\right) mb}{f(\beta - p_f)}t\right] \propto C_n e^{-t/\tau_n} \tag{3.14}$$

where

$$\tau = \frac{f(\beta - p_f)}{g^2(\rho_s - \rho_l)mb} \tag{3.15}$$

C_n is the initial concentration of the solute, g is the acceleration due to gravity, ρ_s is the density of the sedimenting phase, ρ_l is the fluid density, m is the mass per sedimentation particle, b is the buoyancy correction factor $\left(b = 1 - \frac{\rho_l}{\rho_s}\right)$, [130] f is the frictional coefficient given by Stokes' relation, p_f is the fluid pressure, and β is related to the solid-fluid interaction force and has the dimensions of pressure.

In a real dispersion there are more than one distinct sedimenting phase, and each phase can be characterised by its own τ and concentration of that specific phase. [126] There may also be a soluble phase; thus the local time-dependent concentration of a dispersion with n insoluble phases and one soluble phase can be described by

$$C(t) = C_0 + \sum_n C_n e^{-t/\tau_n} \tag{3.16}$$

where C_0 is the concentration of the soluble phase. In addition, conservation of mass dictates that the total initial concentration C_{Tot} should equal the sum of the soluble phase and all of the sedimenting phases.

$$C_{Tot} = C_0 + \sum_n C_n \tag{3.17}$$

3.5 CONCLUSION

This chapter provided a brief overview of the theory behind why specific solvents are better at exfoliating specific 2D materials compared to others. It can be summarised by stating that mixing is favourable when there is a minimal energetic stress between the solute and the solvent. In dispersions generally, the solvent also acts to stabilise the solute against reaggregation, and thus a determination of the quasi-stability of the solute can be related to the solvent's effectiveness. This is measured by monitoring the optical transmission through a dispersion as a function of time. By fitting an

exponential decay to the data, one can determine the percentage of stably dispersed material and the sedimentation time constant, τ.

4

SAMPLE PREPARATION AND CHARACTERISATION TECHNIQUES

4.1 INTRODUCTION

This chapter will discuss the steps involved in liquid phase processing of two dimensional crystals and the various analytical and quantitative techniques used to unambiguously characterise them. The sample preparation procedure can be broken in two main parts: ultrasonication and centrifugation. During the sonication process, energy is added to the dispersion to overcome the van der Waals forces that hold the individual nanosheets together and promote exfoliation. The centrifugation process aims to separate the larger pieces that did not receive complete exfoliation from exfoliated nanosheets. The supernatant was separated from the sediment and stored for further characterisation and experimentation.

The dispersion was initially characterised by absorption spectroscopy. The absorption spectra can confirm the materials' identity and by using the Lambert-Beer law the concentration of material dispersed was determined. Consecutive absorbance measurements over a period of time were used to indicate the temporal stability of the two dimensional crystals in dispersion. The crystals were then isolated from the solvent by dropping or filtering the dispersion onto a porous membrane. Electron microscopy of the deposited material was used to examine the dimension, stoichiometry and level of exfoliation of the crystals. Raman spectroscopy also indicated the flake quality and dimension. Finally, in some cases, atomic force microscopy measurements were performed on crystals that were spray cast onto appropriate substrates, providing a surface profile from which crystal heights were determined.

4.2 SAMPLE PREPARATION

4.2.1 *Ultrasonication*

Ultrasonication of weakly bound layered materials in specific solvents adds sufficient energy to overcome the interlayer interactions between the layers in the crystal. During sonication an electrical signal is converted into a physical vibration. The sonicator is composed of an ultrasonic electric generator which creates a signal to power a transducer. This transducer then converts the electrical input into a mechanical vibration which is amplified by the sonicator and passed through the sonic bath or tip. This transfers the vibration to the sample and causes cavitations. These caviations of forming and collapsing bubbles, induce shockwaves which exfoliate the layered crystals into individual nanosheets. These nanosheets are then dispersed throughout the solvent, which aims to stabilise the nanosheets and minimise aggregation.

Sonication theory and experiments on polymers and low dimensional nanostructures have established that ultrasonication results in both exfoliation and scission. These arise due to the cavitation bubbles, which generate high strain rates in the surrounding solvent. [131] The frictional forces between the moving solvent and solute can lead to bond fractures when the load is sufficient enough. [132] It has been suggested that this is the cause for sonication induced scission, and has been experimentally found to exhibit an inverse power law dependence with sonication time, t, as $L \propto \frac{1}{\sqrt{t}}$, where L is the longest axis of the solute. [131, 133] There are a variety of parameters that can govern the level of sonication induced exfoliation and scission with time. These include the energy density, the vial geometry, the pulsing rate, the frequency of implosion events and the spatial distribution of cavitations, [134] some of which are not easily controlled by the user.

There are two main sonication systems used throughout this research, an ultrasonic bath and an ultrasonic tip. The Branson 1510E-MT ultrasonic bath had a fixed frequency (20 kHz) transducer attached to its base, with a 2 L water capacity. It is a milder form of sonication, typically with a power output of >25 W . The sample was then positioned

and held inside the bath during sonication. This type of sonication exfoliates the layered crystals into their two dimensional counterpart at good yield but requires prolonged periods of time. Heating of the sample and water evaporation in the bath were issues that were overcome by using a chiller system and a siphon. However, sample reproducibility was a problem. Variability was minimised by ensuring the sample was positioned in the center of the same bath, the same sample vessel was re used and the sample height in the water was kept constant.

The other sonication system used was an ultrasonic probe. During this type of sonication the vibrations travel down the probe at a user defined amplitude and cause localised sonication. The power energy density is much higher than that of the bath and so required less time to reach higher concentrations of dispersed material. The probe can either be a point probe or a horn probe sonic tip. During parts of this research a horn probe sonic tip was used, even though the power output was less than that of the point probe. This type of probe allowed for larger volumes of dispersions to be sonicated, typically 100 ml. A VibraCell CVX 750W was the model of sonic probe used throughout experimentation. The sample beaker was also connected to a cooling system that allowed for cold water (5°C) to flow around the dispersion during sonication.

4.2.2 *Centrifugation*

The earth's gravitational field causes materials above 1 μm^3 to sediment rapidly. However for materials below this size, centrifugation of materials in suspersion can speed up this processes by creating a centrifugal force on the nanosheets in dispersion. During centrifugation the unexfoliated material is forced against the wall of the vial and collects at the bottom. The centrifuge used during this research was a Hettich Mikro 22R. This centrifuge had a fixed angle rotor that held up to 6 samples with ~30 ml capacity in each tube. All centrifugation was performed over a 45 minute period and the centrifuge temperature was kept constant at 40°C.

Discussed in chapter 6 & 8, centrifugation also offers a way to size separate the two dimensional crystals. It was observed that after a high centrifugation rate (~5000 rpm) the supernatant contained light, thin and small nanosheets while after a low centrifugation rate, it contained a combination of light, thin and small nanosheets amongst some heavier, thicker and bigger material. By analysis of what remains suspended in the supernatant, one can infer what remains in the sediment. This sediment can also be redispersed and re-centrifuged. In response to the centrifugal forces applied to them, if a high centrifugation rate is initially chosen, the small flakes will be removed in the supernatant leaving behind larger flakes in the sediment. By redispersing this sediment and centrifuging it at a lower centrifugation rate, the resulting flakes in the supernatant will have a larger mean flake dimension in comparison to the first supernatant. If this recycling of the sediment and re-centrifuging at a lower centrifugation rate than the previous one is repeated, one can isolate the flake dimensions into groups; from the smallest flakes to the largest in the dispersion. This method will be discussed in more detail with respect to graphene and MoS_2 in chapter 6 & 8, respectively.

4.3 SAMPLE CHARACTERISATION

4.3.1 *UV-Vis NIR Absorption Spectroscopy*

The samples were characterised by UV-vis-NIR (ultraviolet-visible-near infrared) spectroscopy. UV-vis-NIR spectroscopy was used to measure the absorbance of the two dimensional crystals in dispersion over a range of wavelengths, typically between 1600 and 200 nm. These measurements were taken with a Varian Cary 6000i dual beam spectrophotometer, which uses a monochromator to select light of a specific wavelength from a tungsten halogen lamp source. At specific wavelengths, different materials absorb light differently due their unique band structure. Absorption peaks were observed when the frequency of incident light was matched to an electronic transition. This in turn leads to a drop in transmission which is measured by comparing the intensity of the sample beam (I) to the reference beams (I_0).

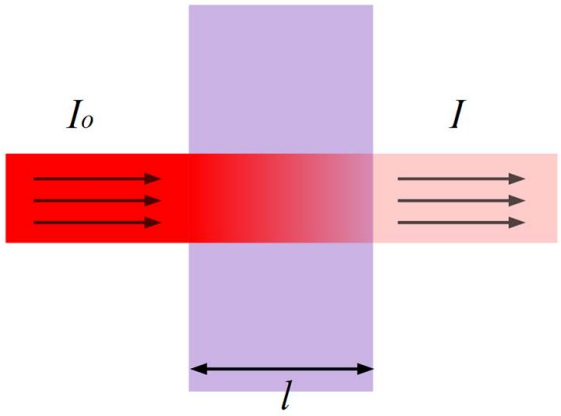

Figure 4.1: Schematic of light attenuation by absorption of the sample

$$T = \frac{I}{I_0} \tag{4.1}$$

This can be related to absorbance by,

$$A = -ln\,(T) = -ln\left(\frac{I}{I_0}\right) \tag{4.2}$$

where the absorption A, is proportional to α, the extinction coefficient of the material, C, the concentration (mg/ml) and the path length, l by

$$A = \alpha C l \tag{4.3}$$

This relationship is referred to as the Lambert-Beer Law and can be used to determine the concentration of the dispersions provided the extinction coefficient is known. A dilution series of the 2D crystals in dispersion was also performed, to ensure all the material in dispersion obeyed this law.

The absorption spectra for graphene were featureless, as expected [135] and A was recorded at 660 nm [2]. The featureless spectra were expected because of graphene's unique band structure, unlike MoS_2 which is a semiconductor with a discrete band gap. With MoS_2 nanosheet dispersions, as the frequency of incident light changes, electrons are allowed to move from one state to another. This is evident by characteristic peaks in the spectra which can provide information on electronic transitions and can be used to

identify the material. For MoS_2 there are two main features at around 679 and 610 nm. The absorbance value at 679 nm was used to determine the concentration of dispersed material.

For both of these materials, the absorption coefficient, α was measured. To do this a known volume, with a measured absorbance per unit cell, A/l, was filtered through a membrane. Next by careful weighting, the concentration, C, could be measured ($C = \frac{m}{V}$) and used to determine an α value in mg/ml/m. This was measured for a range of sonication times and centrifugation rates by preparing large volumes of dispersion. It was found for graphene that α_{Gr} was relatively invariant with processing procedure, as one would expect, with an average value of 3620 ± 575 mg/ml/m. For MoS_2, the absorption spectra were superimposed on a power law scattering background ($\propto \lambda^{-n}$), thus making the absolute value of A/l unreliable. To overcome this, the scattering background was extrapolated from the high wavelength region and subtracted. This gave a mean α_{MoS_2} of 1020 ± 153 mg/ml/m.

4.3.2 *Temporal Stability*

The temporal stability of the dispersions were measured using a home built sedimentation apparatus. [126] The apparatus consisted of four lasers (λ = 650 nm) and four photodiodes stacked vertically opposite each other and the dispersion was housed between them in a 10 mm quartz cuvette. The lasers were set to run, with a synchronised pulse duration of 30 ms for a set period of time, typically weeks. The transmission spectra of the laser light through the dispersion, was then converted to absorbance per unit cell using the Lambert-Beer law. The data across the four lasers was averaged and its respective baseline deducted. The data was then normalised and plotted as normalised absorbance (a.u.) as a function of time (hrs).

4.3.3 *Raman Spectroscopy*

Raman spectroscopy is a non-destructive, fast, characterisation technique that can give crucial information about bulk powders and exfoliated 2D nanosheets. Both graphene and MoS_2 are highly Raman active, with distinct features in their spectra. [136, 137] During this research Raman spectra were measured using a red HeNe 633 nm laser with a Horiba Jobin Yvon LabRAM-HR and a Witec Alpha 300R (532 nm). These systems were operated with a 100x objective lens and diffraction grating with 600 lines mm^{-1}. The acquisition time per pixel varied depending on the signal to noise ratio and the spatial resolution of the laser was ~3-5 µm and 500 nm for the two Raman spectrometers respectively. The technique itself involves a monochromatic light source, which is directed at the sample. During this process, the majority of light is scattered elastically (Rayleigh scattering), while a small portion of light was inelastically scattered. The study of inelastically scattered photons is called Raman spectroscopy and the change in energy of the scattered photons is referred to as the Raman shift. A Raman spectra is a plot of intensity of Raman scattered photons versus the Raman shift in wavenumbers. The peaks in the spectrum can be correlated to a set of vibrational modes that correspond to specific materials.

4.3.3.1 *Raman Spectroscopy of Graphene*

The main features in a typical graphene Raman spectra are the D, G and 2D bands (figure 4.2A). [138] The D band, so called after defects, can be found at ~1350 cm^{-1}. This is associated with breathing modes in sp^2 carbon rings and requires a break in symmetry due to edges or a high density of defects to become active. [139] Pristine graphite or graphene will not display a D band; however any disruption of the graphitic basal plane by chemical functionalities or edges will result in an increased D band. The second main feature is the G band, found at ~1580 cm^{-1}, it is characteristic of sp^2 hybridised carbon atoms and is also found in a graphite spectrum. [140, 141] The G-band is invariant with the number of layers, unlike the third feature, the 2D band which lies ~2700 cm^{-1}. [142] This is a double resonance process of the D band

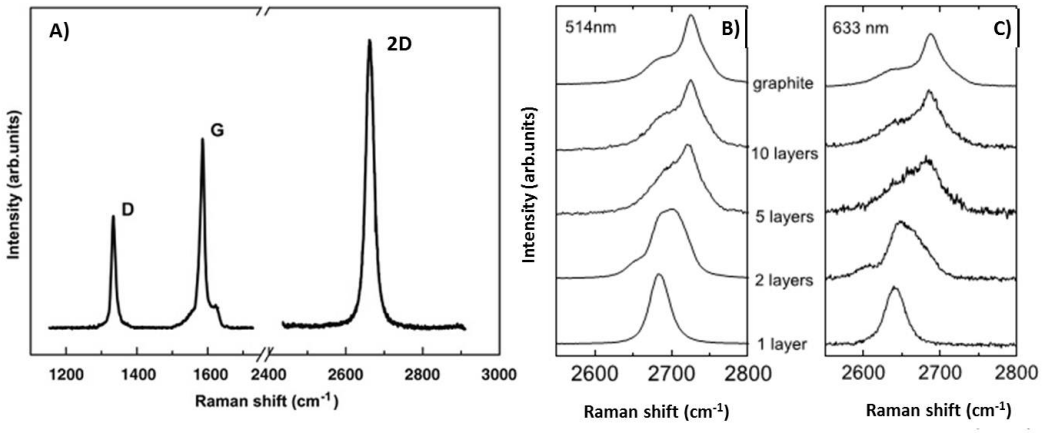

Figure 4.2: A) Raman spectrum taken of a graphene edge showing the main features the D, G and 2D bands. This spectrum was taken with an excitation wavelength of 514 nm.[143] B) Evolution of the 2D band spectra at 514 nm with the number of layers. C) Evolution of the Raman spectra at 633 nm with the number of layers.[136]

and is always there, irrespective of the D band. Ferrari et al. found that the shape of the 2D band can be used to determine if it is a single or multi- layered graphene samples. This band evolves with the number of layers and thus with the evolution of the band structure (figure 4.2B&C). [136] For monolayer graphene, the 2D band is a single Lorentzian peak (FWHM ~30 cm^{-1}) with an intensity ~4 times greater than the G peak. [136]

4.3.3.2 *Raman Spectroscopy of MoS_2*

There are two main bands of interest when examining MoS_2 Raman spectra. [137, 144, 145] The E^1_{2g} and the A_{1g} bands located at 383 cm^{-1} and 409 cm^{-1} respectively. The band located at 383 cm^{-1} is associated with in plane vibrations, while the 409 cm^{-1} band is indicative of out of plane vibrations. Similar to graphene, the number of layers in an MoS_2 nanosheet can be inferred from the spectra.[146, 147] Experimental evidence suggests that a decrease in the frequency of the A_{1g} band and an increase in the E^1_{2g} band occurs with a decreased number of layers, as seen in figure 4.3. An increase in intensity is also observed for the A_{1g} band. The decrease in frequency in the A_{1g} band occurs because there are less van der Waals interactions restricting the

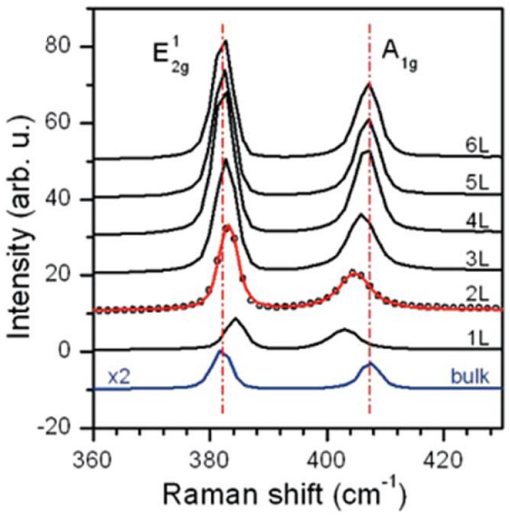

Figure 4.3: Raman spectra for bulk MoS_2 powder and thin (nL) nanosheets. n is labeled on the right side of its corresponding spectrum.[146]

atoms vibrating. These shifts could also indicate the absence of long range Coulombic interlayer interactions that are potentially there when the material is in its bulk state.[146]

4.3.4 *Electron Microscopy*

When imaging an object, the radiation used to observe it must have a wavelength comparable to that of the object. Electrons accelerated at 10 kV or 200 kV have a wavelength of 12.3 pm or 2.5 pm respectively, making them ideal for interacting with 2D nanosheets and thus will contain information about any interaction and ultimately the sample. Transmission electron microscopy (TEM) was chosen to characterise the exfoliation state of the graphene dispersions and the nanosheet dispersions for two main reasons. Firstly the ease of sample preparation and secondly the wealth of information that can be obtained. Furthermore, structural analysis was also obtained using high resolution transmission electron microscopy (HRTEM). Scanning electron microscopy (SEM) of the powders was used to identify the layered strata in the powder

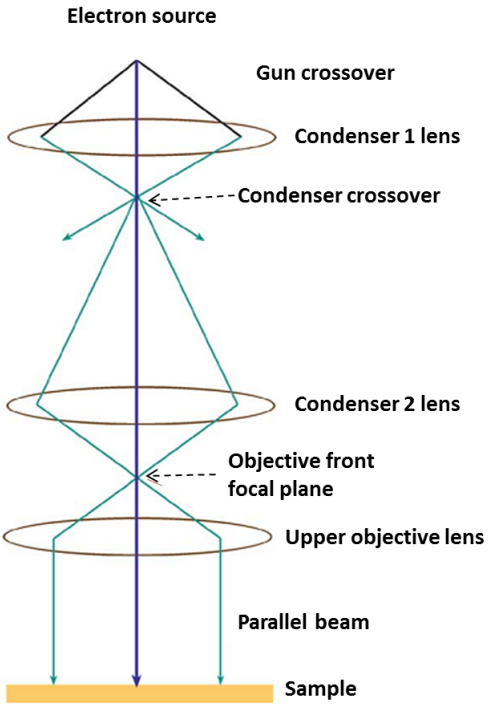

Figure 4.4: Schematic of the illumination system in a TEM

and if there was an impurity phase. SEM of the filtered dispersions allowed for film morphology, density and uniformity to be determined.

4.3.4.1 *Transmission Electron Microscopy (TEM)*

The TEM is made up of an electron source, electromagnetic lens, various apertures and a phosphor screen/CCD camera. The illumination system controls the incident beam on the sample, and is made up of a condenser, aperture and lens. These produce a parallel beam of coherent electrons along the optic axis, to interact with the sample (figure 4.4). [148]

Upon interaction, the beam undergoes transmission or is either scattered elastically or inelastically. After the beam has passed through the sample, the objective aperture only allows the unscattered electrons to travel to the projection lens system, which projects and magnifies the beam onto the phosphor screen/CCD.

The electron source in the microscope is very important and will affect the resolving ability of the electron beam. Two TEM's were used during this research, one with a thermionic LaB_6 filament (JOEL 2100, operated at 200 kV), which was used primarily

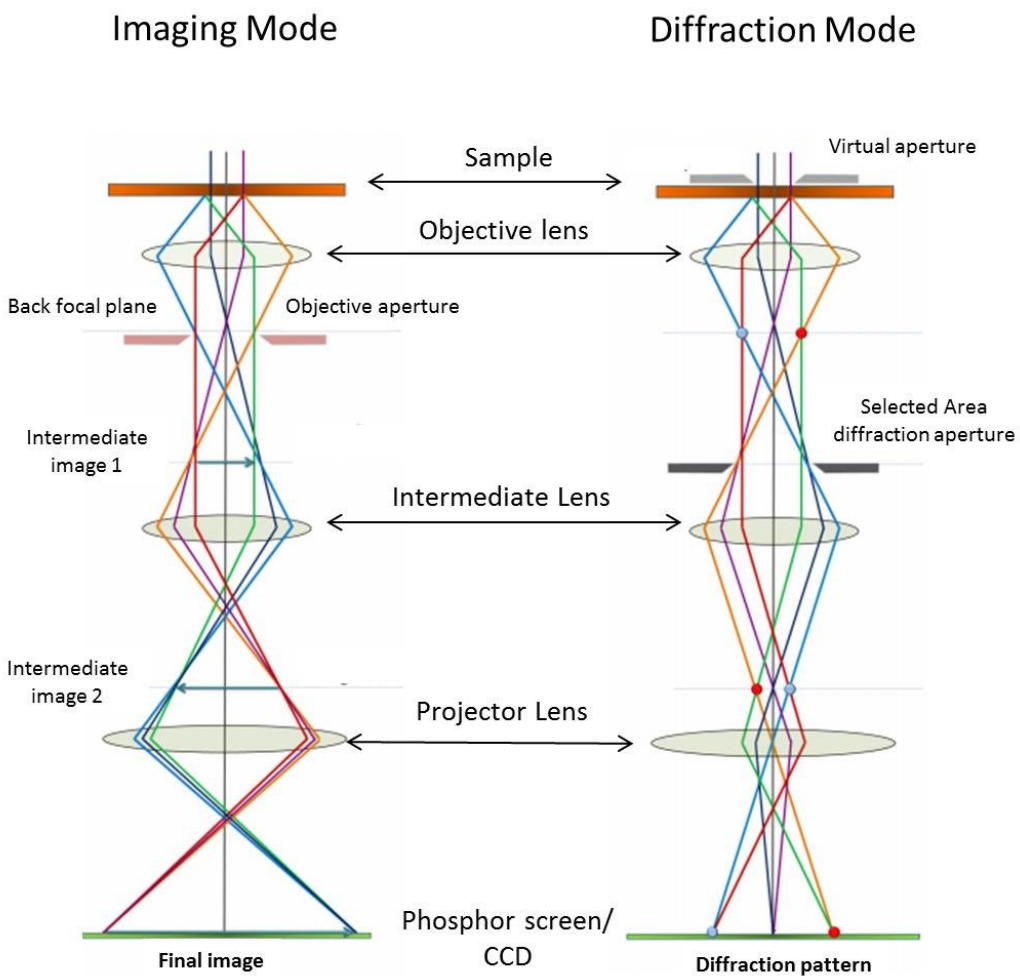

Figure 4.5: Schematic of two of the modes of operation in a TEM, normal imaging mode and diffraction mode. [148]

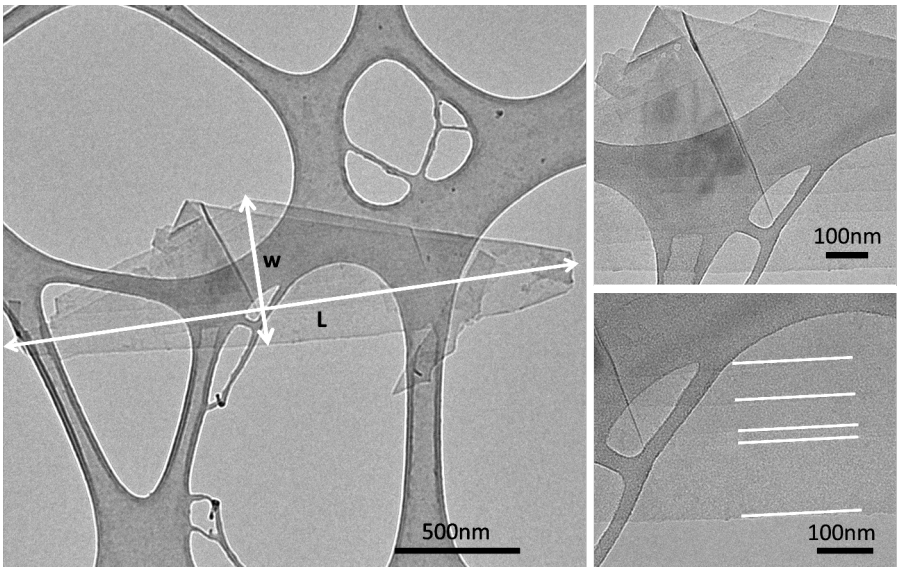

Figure 4.6: Labeling of flake dimensions, L and w and identification of number of layers N.

for bright field imaging. The other TEM used contained a Shottky field emission source (FEI TITAN, operated at 300kV) and was used for high resolution TEM (HRTEM) and diffraction.

During bright field imaging the illumination the apertures in the illumination system produce a coherent wavefront of electrons to interact with the sample and the objective aperture is inserted to achieve better diffraction contrast during imaging (figure 4.5 left side). At magnifications of typically 10,000 and above, the level of exfoliation could be identifed. The flakes' dimensions could also be measured and statistical analysis of the flakes' thickness, length and width could be determined. A flake's lateral dimension was measured by approximating the longest axis as its length, L, and the dimension perpendicular to that at the widest point was its width, w (figure 4.6). The number of layers, N, was estimated by zooming in on the edge of a flake and identifying the strata where possible. As seen in figure 4.6, this flake has five layer edges that can be easily identified. However, this was not always possible for some multi layers and in some cases, it was only possible to estimate N. It is also expected that the errors involved are random and so cancel out when data for many flakes are combined in a histogram.

The TEM samples were prepared by pipetting the dispersion directly onto a holey or lacey carbon support mesh on a copper TEM grid. The TEM grid had an area of ~ 3

mm^2, with a carbon support mesh containing pores, typically ~ 200 nm in dimension. This allowed for the flakes to remain captured while the solvent percolated through. Sometimes the use of a continuous carbon film TEM grid was required to ensure flakes with dimensions > 100 nm could be captured and observed. The volume of dispersion pipetted depended on the concentration of the dispersion and sometimes the dispersion required dilution. The grids were allowed to dry in air or baked in a vacuum oven, depending on the solvent used.

4.3.4.2 *Electron Diffraction*

The electron beam has a wavelength comparable to the crystal lattice and therefore also contains crystallographic information about the samples. When the microscope is set to diffraction mode, an additional selected area aperture is in place (figure 4.5 right side). This ensures that the exit beam only carries information from a localised area of the sample. The diffraction pattern is formed after the exit wave goes through the objective lens, in the back focal plane. This diffraction pattern is then projected onto the phosphor screen/ CCD for analysis. The orientation of the sample, with respect to the beam and the samples thickness, play a strong role in the resultant diffraction pattern. Provided the sample is crystalline, the resultant diffraction pattern will contain spots that can be related to structural information about the crystal's lattice (through Braggs law). The intensity of the diffracted beam is also linked to the position of the atoms in the unit cell through the structure factor. Such patterns can be used to unambiguously identify mono- , bi- or multi- layered graphene. [2, 19, 149] However, this has not been the case for MoS_2, where simulated intensity ratios and structure factor calculations have indicated that there is no distinguishable difference between single and multi-layered nanosheets. [13]

4.3.4.3 *High Resolution TEM (HRTEM)*

When HRTEM information is combined with diffraction information, one can gain a lot of information about two dimensional crystals. To achieve high resolution imaging conditions, the condenser and objective apertures were set to the widest settings. Thus all the diffracted beams can interfere, causing an interference pattern that will contain

phase information. This interference pattern is then projected onto the phosphor screen/CCD and the image is formed by phase contrast, as opposed to diffraction contrast. However, the spatial resolution is still limited by inherent spherical and chromatic aberrations, which can only be alleviated by the inclusion of correctors. These correctors aim to constructively and destructively distort the beam, and thus cancel out aberrations. Unfortunately, correctors were not accessible during this research, however, further digital filtering in digital micrograph was sometimes used to alleviate some of the blurriness.

4.3.4.4 *Scanning Electron Microscope (SEM)*

A scanning electron microscope uses a focused beam of accelerated electrons (~5 kV) to probe the sample, while current carrying coils are used to raster scan the beam across the sample. As the beam interacts with the sample, kinetic energy is transferred and the incident electrons are decelerated. This energy is then dissipated as a variety of beam-sample interactions which are monitored by a variety of detectors inside the chamber. All SEM measurements were made using a Zeiss Ultra Plus SEM. The electron beam generator is a thermal field emission tungsten tip, with a sintered reservoir of zirconium oxide in the shank. Three detectors were used to monitor these interactions, the secondary electron (SE) detector, the back scattered electron detector (BSE) and the Inlens detector. Each detector is positioned at a discrete location to collect electrons from a different interaction volume as seen in figure 4.7. The SE detector collects electrons produced by inelastic scattering events that have low energy and a short mean free path, hence contain good topography information. The BSE detector collects higher energy, elastically scattered electrons from deeper within the interaction volume. These energy of the scattered electrons can be used to identify chemical compositions in multiphase samples. The Inlens detector, which is not labeled in this diagram was also sometimes used. This detector is efficient at collecting scattered electrons from low acceleration voltages, and is placed directly in the beams path, close to the sample, allowing for better surface analysis.

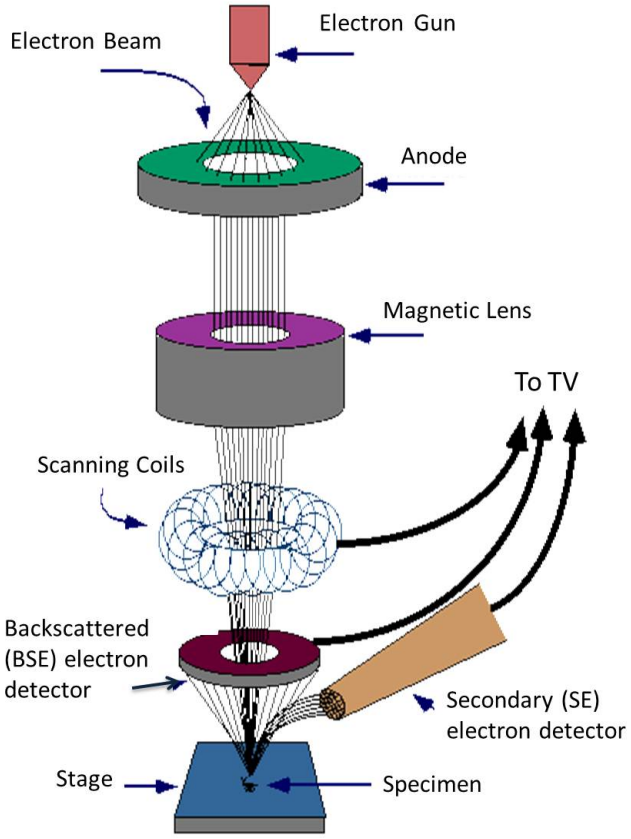

Figure 4.7: Schematic of an SEM, displaying the scanning coils, secondary electron and back scattered electron detectors.

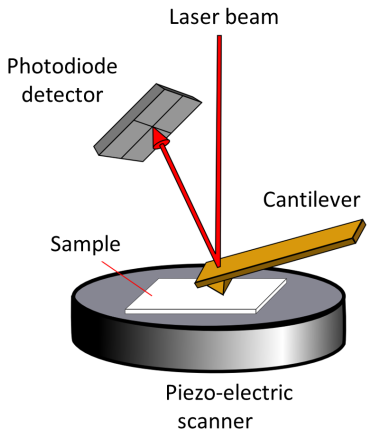

Figure 4.8: Schematic of an AFM

4.3.5 *Atomic Force Microscopy (AFM)*

An AFM is a very sensitive probe microscope, with resolutions up to fractions of a nanometre. The machine used throughout characterisation was a Vecco Dimension V, with a SiN tip. The samples were prepared by spraying the dispersion directly onto silicon dioxide. The principle of operation is based on a microscale cantilever with a very fine tip (< 10 nm), that comes in contact with the sample. This contact causes the tip to deflect according to Hooke's law. The deflection is then measured indirectly by a laser which is directed onto the back of the cantilever (figure 4.8). Any shift is then projected onto a photodiode, where a feedback loop can adjust the height of the sample, which is sitting on a piezoelectric stage. This occurs when the AFM is operating in contact mode. The down side to this mode of operation is that the lateral forces between the tip and the sample can lead to the tip becoming damaged. This was minimised by operating the AFM in tapping mode. During this operation mode the cantilever is oscillated at, or close to, its resonant frequency (300 kHz). When the tip came close or in contact with the sample, the oscillation amplitude fluctuates due to interaction forces. The changes in oscillation are compared to the external reference oscillation, and thus can provide information about the surface topography and the flakes on the surface. The data was then imported in Gwyddion software, where flake heights were determined.

5

HIGH CONCENTRATION SOLVENT EXFOLIATION OF GRAPHENE

5.1 INTRODUCTION

The discovery of graphene and its incredible properties greatly excited the scientific community and many researchers began working on ways to prepare this material at high quality and high yield. Before 2008, efforts made either produced high quality monolayers at very low yield (via micromechanical cleavage) [1] or relatively high yield, mildly defective graphene with degraded properties (reduced graphene oxide). [150] In order to address these issues, this research group [2, 62] and others [77, 78, 115] developed methods to exfoliate pristine graphite powder to give graphene in the liquid phase without oxidation or defect formation. This method relies on the exfoliation and stabilisation of graphene using specific solvents. This solvent-exfoliated graphene has the potential to be useful in a host of applications in both industry and research. However, these methods have one critical disadvantage: the graphene can only be dispersed at relatively low concentration, typically 0.01 mg/ml. Such a low concentration makes many applications completely impractical. This gives graphene oxide a significant advantage as it can be dispersed in some organic solvents at concentrations of up to 1 mg/ml, [67, 74] and in water at concentrations of up to 7 mg/ml. In order to gain full advantage from dispersions of pristine graphene in solvents, it is critical to increase the maximum concentration obtainable while maintaining the quality of the graphene flakes. In this chapter, such a method was demonstrated.

5.2 EXPERIMENTAL PROCEDURE

A set of identical graphene dispersions were prepared by adding powdered graphite (as seen in figure 5.1) (Branwell natural graphite, grade 2369, www.branwell.u-net.com/) to *N*-methyl-pyrrolidone (NMP) (spectroscopic grade, Sigma Aldrich) at a concentration of 3.3 mg/ml (700 mls, round bottomed flask). These dispersions were then bath sonicated for various periods of time from 6 hrs to 462 hrs. It is noted that the true power output (estimated from the measured rate of temperature increase (K/s) when sonicating a known mass of water) tends to vary between even nominally identical sonic baths. Throughout this work, a single sonic bath with a measured output of 23 W was used. After sonication, the dispersions were transferred to vials and centrifuged at 500 rpm for 45 minutes. Following centrifugation, the top 20 mls (out of 28 mls) were carefully removed and retained for further use. The set of centrifuged dispersions appeared darker in colour for longer sonication times, as shown in figure 5.2 inset. The UV-vis-IR absorbance spectra were measured, appearing flat and featureless in all cases. The concentration remaining after centrifugation, C_G, was calculated using the absorbance per unit cell, A_{660nm}/l and the measured mean absorption coefficient of graphene in NMP, α. The absorption coefficient was measured for a range of sonication times and centrifugation rates by preparing large volumes of dispersion, measuring A_{660nm}/l, and then finding the dispersed mass by filtration and weighing. It was found to be relatively invariant with processing procedure, displaying a mean value of $\alpha = 3630 \pm 575$ mg/ml/m, slightly higher than the previous estimate of $\alpha = 2460 \pm 500$ mg/ml/m. [2] Samples for TEM were prepared by pipetting a few millilitres of dispersion onto a holey carbon grid and imaged in bright field mode at 200 kV. All thin films were prepared by vacuum filtering the dispersion onto a porous alumina membrane (Whatman Anodisc 47 mm, pore size = 0.02 μm). Thick films were prepared by vacuum filtering more dispersion onto the alumina membrane, to give between 40 and 80 μm free standing thick graphene films. They were dried for 24 hrs in a 65°C oven to remove any trapped air bubbles, followed by 48 hrs in a vacuum oven at 60 °C.

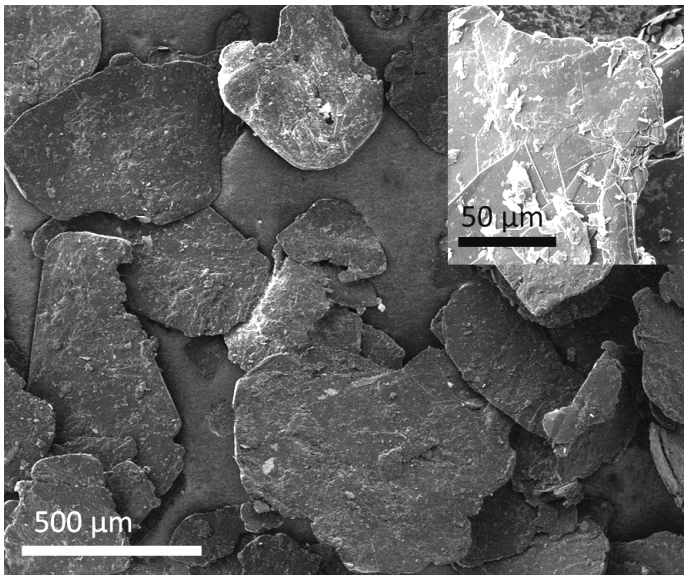

Figure 5.1: Scanning electron microscope image of Branwell natural graphite powder and (inset) a magnified image at the edge of a flake.

5.3 RESULTS AND DISCUSSION

One can hypothesise that the concentration of exfoliated graphene dispersed in solvents such as NMP is limited by the amount of energy added during sonication. This can be rigorously tested by monitoring the dispersion quality, concentration, flake dimension and thickness as a function of sonication time.

5.3.1 *Graphene dispersion optimisation*

Increasing the initial concentration of graphite (from 0.1 mg/ml to 3.3 mg/ml) and prolonging the sonication time resulted in the concentration increasing steadily from 0.06 mg/ml after 0.5 hr to 1.2 mg/ml after 270 hrs, at which point it saturated, this is shown in figure 5.2. This concentration is much larger than the previous maximum concentration of 0.01 mg/ml [2] and is comparable to the best results for graphene oxide in organic solvents. [69] We note that, empirically, the data closely follows a $C_G \propto \sqrt{t}$ trend, illustrated by the red line in figure 5.2.

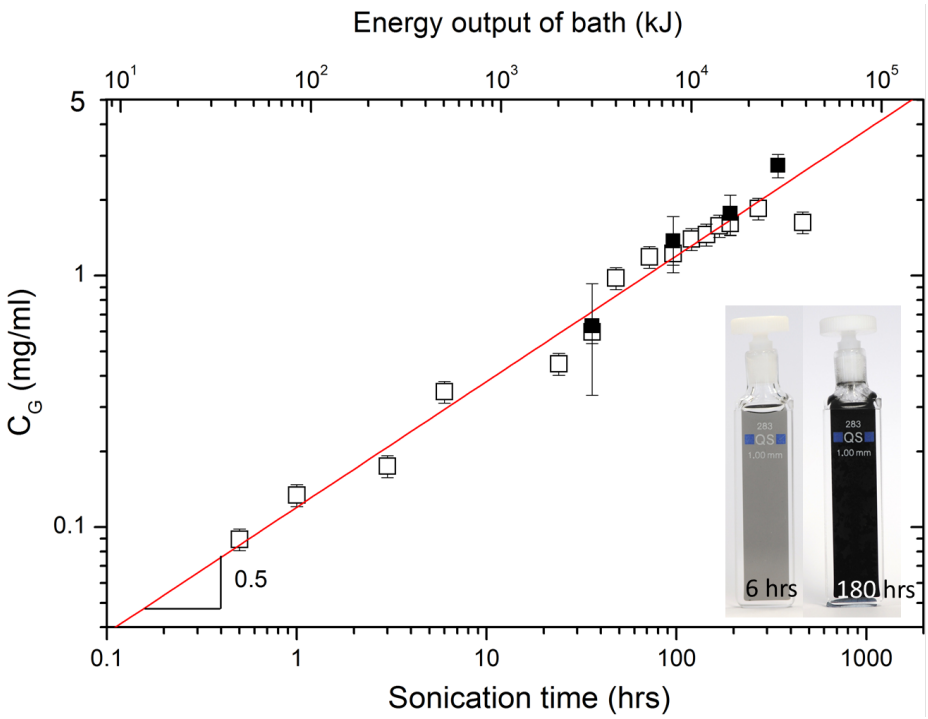

Figure 5.2: Concentration of graphene after centrifugation as a function of sonication time. The upper axis shows the total energy output of the bath, calculated using the measured power output of 23 W. The solid data points represent the samples whose dimensions were used in eqn 5.1 to determine their concentration. Inset: Two 1 mm cuvettes containing graphene dispersion after 6 hrs and 180 hrs sonication, respectively.

5.3.2 *Analysis of dispersion quality*

Increasing the concentration of graphene dispersions is only useful if the dispersion quality is maintained at these higher concentrations. To test this, TEM analysis on a subset of dispersions was performed. A few drops, taken from dispersions sonicated for 36, 96, 192 and 343 hrs respectively, were dropped onto holey carbon grids and analysed using TEM. Shown in figure 5.3 are representative TEM images of the flakes observed. Figure 5.3A shows a graphene monolayer while figure 5.3B shows a multilayer. The monolayer can easily be identified by its well defined edges, while the multilayer is typical of the larger objects observed regularly. Some thick multilayers were observed on rare occasions. These objects are non-transparent to the electron beam but have lateral dimensions similar to the thinner flakes. Of the >400 flakes observed, only 2 were very thick objects. It can be noted that for short sonication times, the grids were sparsely coated by flakes, making the flakes difficult to find using TEM. Shown in figure 5.3D is a wide-field image of a TEM grid prepared from a long sonication time sample (180 hrs). This image is covered by large numbers of flakes and is typical of those observed for longer sonication times.

The large numbers of flakes observed make statistical analysis relatively easy for these samples. The TEM images of the type shown in figure 5.3 were used to generate statistical data on the exfoliation state of the graphene in these dispersions (as discussed in further detail in chapter 4, section 4.3.4.1). For each flake observed, the length, L, and width, w, was measured and an estimate of the number of layers per flake, N, was determined. This was done for approximately 100 flakes for each sonication time. The monolayers were identified by their well defined, straight edges and characteristic diffraction pattern, [2] where the inner spots ($\{1100\}$) are more intense that the outer spots ($\{2110\}$). An example of a graphene bilayer diffraction pattern can be seen in figure 5.3C inset, where the intensity of the $\{1100\}$ reflections are less intense than the $\{2110\}$ reflections.

The statistical results of the flake thickness, length, width and aspect ratio $\left(\frac{L}{w}\right)$ are summarised in figure 5.4. It is worth noting that the distribution of flake thick-

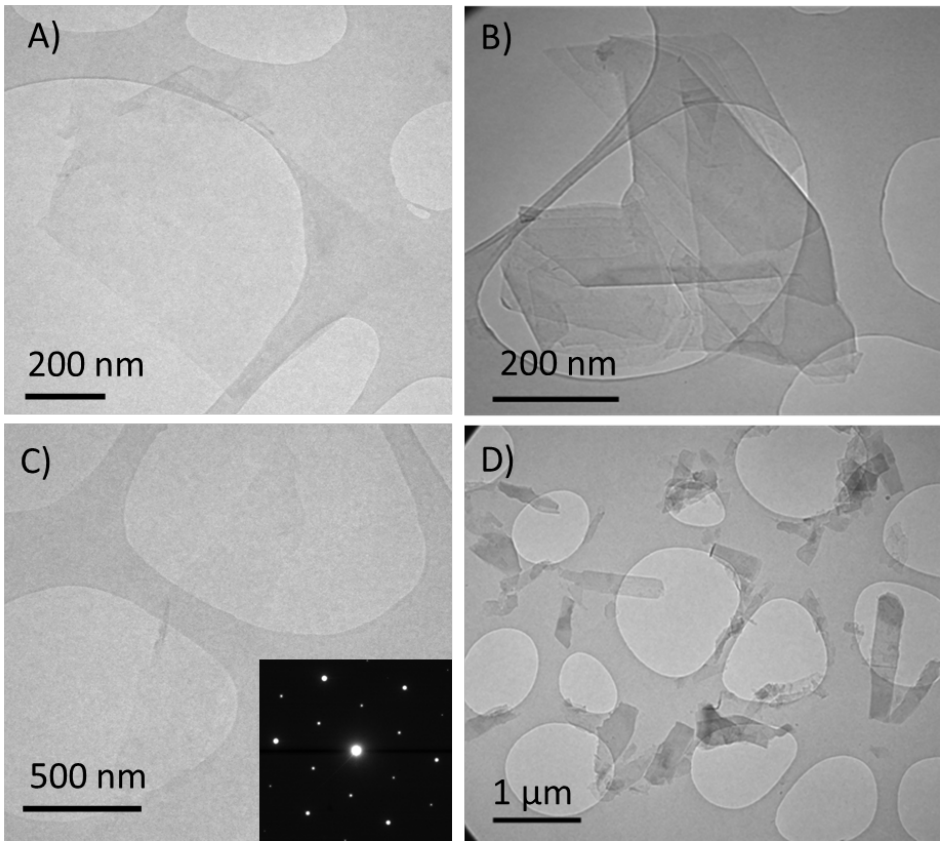

Figure 5.3: TEM images of graphene flakes observed during this work. A) a monolayer, B) a multilayer and C) a bilayer graphene flake with corresponding diffraction pattern, where the intensity of the {1100} reflections are less intense than the {2110} reflections, and D) a wide field image showing the large quantities of flakes observed after long sonication times (180 hrs)

nesses for the most concentrated sample (C_G = 1.2 mg/ml, 343 hrs sonication time) is characteristic of a well-exfoliated sample.

This data shows $< w >, < L >$and $< N >$ the mean width and length of flakes and number of layers per flake as a function of sonication time. The mean number of layers per flake is close to 3 for all sonication times. However, the lateral dimensions of each flake decreased significantly with sonication time, with the mean length falling from $\approx$ 3 μm to $\approx$ 1 μm and the mean width falling from $\approx$ 1 μm to $\approx$ 300 nm. In fact, the data for both flake length and width, scale with the inverse square root of time: $< L > \propto \frac{1}{\sqrt{t}}$ and $< w > \propto \frac{1}{\sqrt{t}}$. This behaviour is expected theoretically and discussed in further detail in chapter 4 section 4.2.1. [151] We note that this time dependence explains a number of aspects of the data outlined in figure 5.4.

The mean flake aspect ratio, $\left\langle \frac{L}{w} \right\rangle$ was also determined and stayed almost constant at 2.5-3 for all sonication times. That $\left\langle \frac{L}{w} \right\rangle \neq 1$ suggests that asymmetric flakes are favoured during the sonication and exfoliation process. From the statistical data, we found that the fraction of flakes with < 5 layers, $\frac{N_{1,2,3,4}}{N_{Total}}$, layers was between 80% and 90% for all samples. In addition the fraction of monolayers, $\frac{N_1}{N_{Total}}$, increased from ~10% for the short sonication times to ~ 20% for the longer times.

5.3.3 *Correlation of concentration and flake size*

This research suggests that the increase in graphene concentration can be correlated to a decrease in flake dimensions, as sonication time is increased. It has been shown for dispersions of nanotubes in NMP, the equilibrium bundle diameter is set by the concentration, such that each bundle has an associated volume of solvent close to the volume of the sphere whose diameter equals the bundle length, as illustrated in figure 5.5, left side. [152] The physical basis of this is that when the bundles are brought closer, by debundling, collisions can occur between rotating adjacent bundles, resulting in aggregation. Given that nanotubes in NMP can spontaneously split from the bundles by desorption, spurred by dilution, [119] resulting in a dynamic equilibrium which sets the relationship between bundle diameter and concentration. If such a correlation

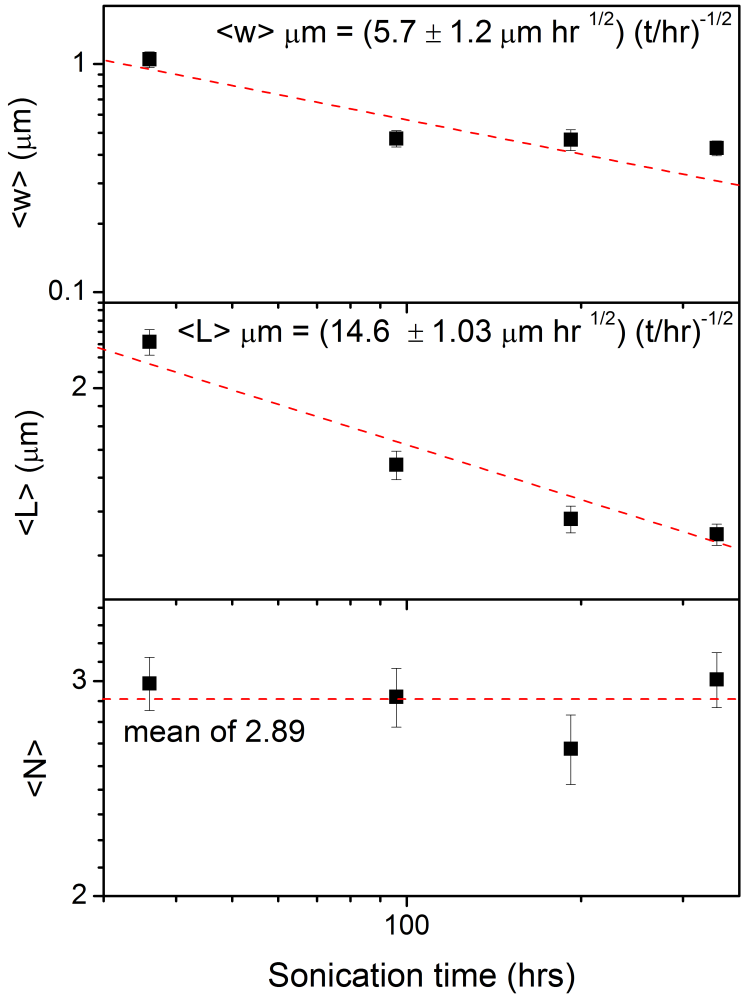

Figure 5.4: $< w >$, the mean width, $< L >$, the mean length and $< N >$, the number of layers as a function of sonication time.

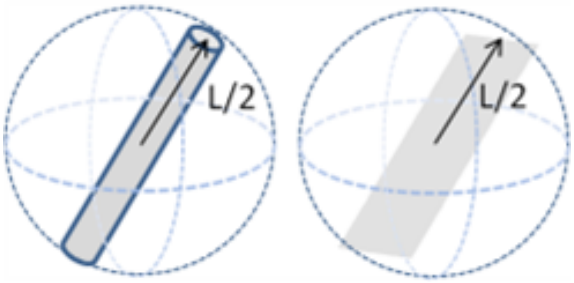

Figure 5.5: Schematic illustrating the hypothesis that the concentration of both nanotube and graphene dispersions are determined by the volume of the solvent sphere defined by the tube or flake dimension

exists here, each graphene flake should reside in a solvent volume equal to the volume of the sphere defined by the flake length, illustrated in figure 5.5, right side.

If this is the case, the dispersed graphene concentration can be expressed as the mass of the average flake divided by the volume of its associated sphere. In this scenario, the concentration is given by:

$$C_G \approx k \frac{\rho_G < L >< w >< N > d}{4\pi \left(\frac{L}{2}\right)^3 /3} \approx k \frac{6\rho_G d}{\pi} \frac{< w >< N >}{< L >^2} \propto \sqrt{t} \qquad (5.1)$$

where k is the proportionality constant, ρ_G is the density of graphite (2200 kg/m^3), and d is the inter layer spacing for individual sheets of graphene in graphite (0.35 nm).

Equation 5.1 also explains the observed scaling of C_G with $\sqrt{t}$. To further investigate this correlation between flake size and concentration, equation 5.1 can also be used to work out the calculated graphene concentration using the data derived from the flake size statistics, $< N >$, $< L >$ and $< w >$. The calculated values are plotted as the red line fit in figure 5.2.

These values (seen as solid data points in figure 5.2) are in good agreement with the measured data (open data points figure 5.2), for $k = 1$. This confirms that the observed concentration is controlled by the flakes' dimensions. Given the invariance of $< N >$ with time and the observed scaling of $< L >$ and $< w >$ with $\frac{1}{\sqrt{t}}$, the $\sqrt{t}$ dependence emerges naturally from equation 5.1. $k = 1$ is not general behaviour and was a surprising result. This represents a state of the system when the concentration is close to the maximum value, set by the flakes' dimensions and also by the fact that

each isolated flake resides in its own sphere of solvent. This is most likely due to the low centrifugation rate of 500 rpm, that was used to centrifuge these samples. This rate was chosen as the lowest rotation rate that was shown to remove all large aggregates in preliminary experiments. Thus this scenario represents the maximum concentration of well dispersed flakes. Higher rotation rates will result in the removal of more material, leading to reduced concentrations and values of $k < 1$.

5.3.4 *Centrifugation rate dependence*

It was also observed that increased rotation rates produced a decrease in dispersed concentration. To test this, a fresh sample was prepared using the experimental method outlined previously and sonicated for 146 hrs. The dispersion was then divided into 4 equal volumes and these were centrifuged at 4 different rates ranging from 500 to 4000 rpm. Following centrifugation, their absorbance was measured and concentration determined and plotted as a function of centrifugation rate, as shown in figure 5.6. Unexpectedly, the decay does not scale off as the inverse square of centrifugation rate. It is also important to point out that this decay does not invalidate equation 5.1; rather it suggests that k is a function of the rotation rate, with $k = 1$ corresponding to the lowest rotation rate.

One might expect that smaller, lighter flakes would remain suspended in the supernatant after higher rotation rates. To test this, TEM analysis was performed on the four dispersions. The measured flake lengths and widths were plotted against centrifugation rates as seen in figure 5.6 inset. Both flake dimensions fell from <L> = 1.02 $\pm$ 0.07 μm, <w> = 0.38 $\pm$ 0.03 μm and <N> = 3.1 $\pm$ 1.6 for the 500 rpm sample to <L> = 0.54 $\pm$ 0.05 μm, <w> = 0.19 $\pm$ 0.01 μm and <N> = 2.9 $\pm$ 0.8 for the 4000 rpm centrifuged sample. This proved that primarily smaller flakes remain dispersed following centrifugation at high rates.

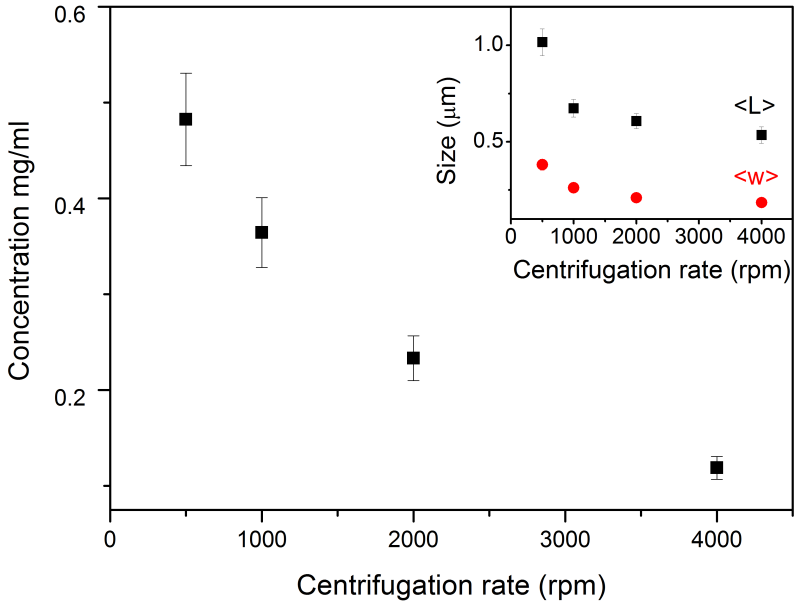

Figure 5.6: Concentration of graphene as a function of centrifugation rate for a constant sonication time of 146 hrs. Inset: $< L >$ *and* $< w >$ as a function of centrifugation rate.

5.3.5 *Defect analysis*

Thus far, we have seen that highly exfoliated graphene dispersions can be produced at reasonably high concentrations. However, as this procedure requires sonication for long times, the possibility of defect formation must be considered. To test this thin films ($\approx$ 50 nm thick) were prepared by filtering a number of graphene dispersions through porous alumina membranes. Their Raman spectra were measured at 10 different spots on each film before normalising and averaging the spectra. The resultant spectra for the 36 and 192 hrs sonication films are shown in figure 5.7. Also shown is a spectrum of the graphite powder. There are three bands of note, as discussed in chapter 4, section 4.3.3.1. These are [136] : the D band ($\approx$ 1350 cm^{-1}), the G band ($\approx$ 1600 cm^{-1}) and the 2D band ($\approx$ 2700 cm^{-1}). The D band gives evidence of the presence of defects due to either edges [139] or topological defects in the sheet. We note that the starting powder displays a small defect population. We can quantify the defect level by the D to G band intensity ratio, I_D/I_G. As shown in figure 5.7 left inset, I_D/I_G increases gradually with sonication, prompting investigation as to whether this increase was due to the

formation of basal plane defects or new edges. It was known from statistical TEM, that as the flakes get smaller with sonication time, the total edge length increases. This is consistent with the data in figure 5.7.

We can further quantitatively test this by noting that for edge defects, I_D should scale with the flake-edge length, while I_G should scale with the flake area. Approximating the flakes as rectangular, this means the ratio should scale as:

$$< \frac{I_D}{I_G} > \propto \left[\frac{1}{< L >} + \frac{1}{< w >} \right] \tag{5.2}$$

As shown in figure 5.8, this is indeed seen to be the case, for both sample prepared for different sonication times and centrifugation rates. It is interesting to see that both sample sets sit on the same straight line. This supports the idea that the increase in the intensity of the D band can be attributed to the introduction of new edges as the larger graphitic crystallites are broken down.

Given the the data in figure 5.8 and the observed time dependences of <L> and <w>, it can then be shown that $<I_D/I_G>$, should scale with $\sqrt{t}$, which is approximately the case, as illustrated by the dashed line in figure 5.7 right side inset. This validates the use of long sonication times, as the presence of basal plane defects would be undesired and expected to significantly degrade the electronic properties.

The shape of the 2D band must also be considered. The shape of this band is indicative of the number of layers per flake. [136, 153] For flakes thicker than ≈ 5 layers, the Raman spectrum is considerably different from that of graphene. None of the 70 spectra measured for the thin films described above displayed graphite-like character. Rather, all spectra were consistent with flakes of 3-5 layers in good agreement with the TEM data. Of note, this also suggests that the graphene does not revert back to AB stacked graphite during film formation. Thus the films consist of a disordered arrangement of randomly re stacked but weakly interacting few layer graphene flakes.

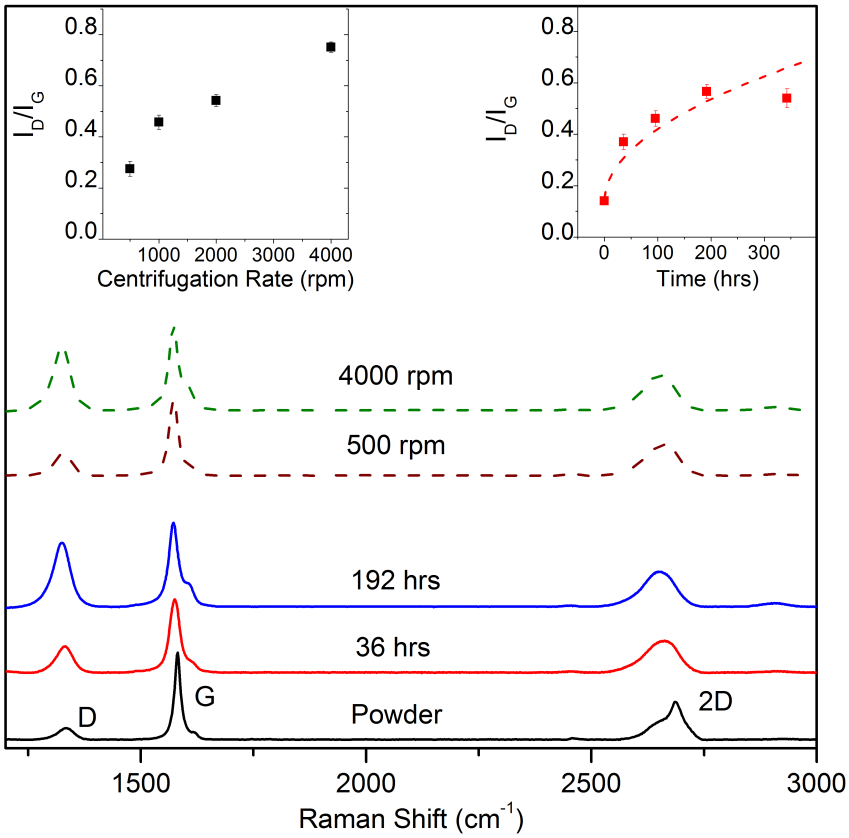

Figure 5.7: Raman Spectra of starting graphite powder and of thin filtered films prepared after 36 hrs and 192 hrs sonication (500 rpm) and after 146 hrs sonication but centrifuged at 500 rpm and 4000 rpm. Inset on left side: D band to G band intensity ratio as a function of centrifugation rate. Inset on right side: D band to G band intensity ratio as a function of sonication time. The errors are standard errors of the distribution of >20 I_D/I_G values. The dashed line shows the behaviour expected if the change in D - band intensity is due to edge formation.

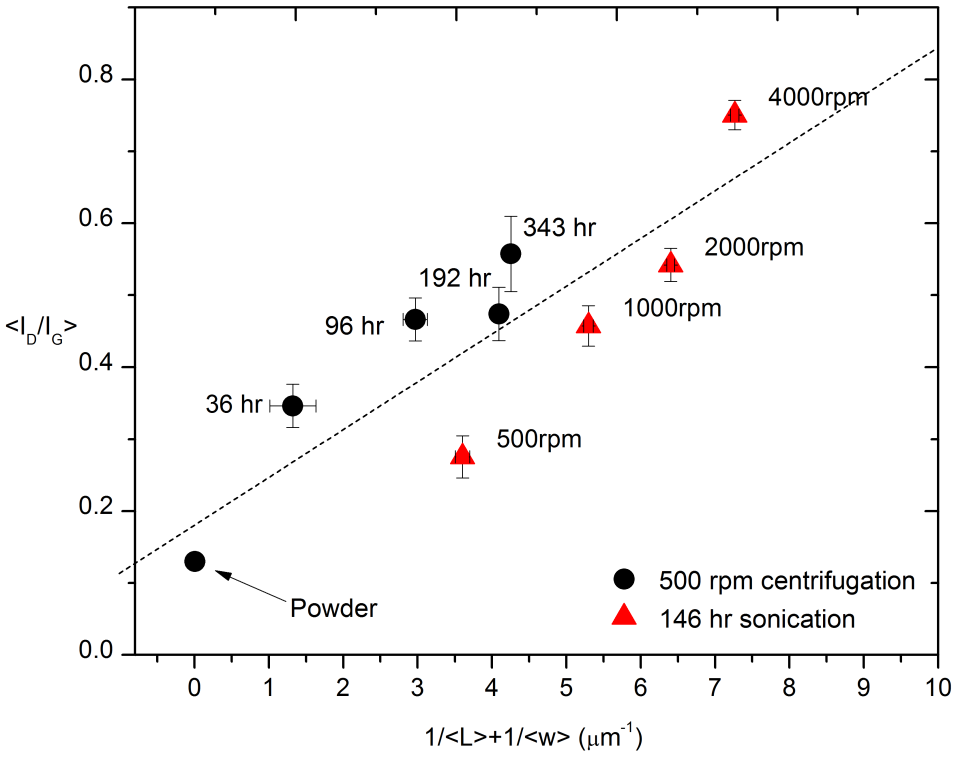

Figure 5.8: Mean Raman D:G band ratio as a function of edge-length to flake area ratio, $\frac{1}{<L>} + \frac{1}{<w>}$. If the D band increase is due to the formation of new flake edges, a straight line would be expected in this graph. The errors in $< \frac{I_D}{I_G} >$ are standard errors of the distribution of > 20 $\frac{I_D}{I_G}$ values while the errors in $\frac{1}{<L>} + \frac{1}{<w>}$ are calculated from the standard errors of the flake length and width distributions. Note that the data point at the bottom left of the this graph represents the graphite powder.

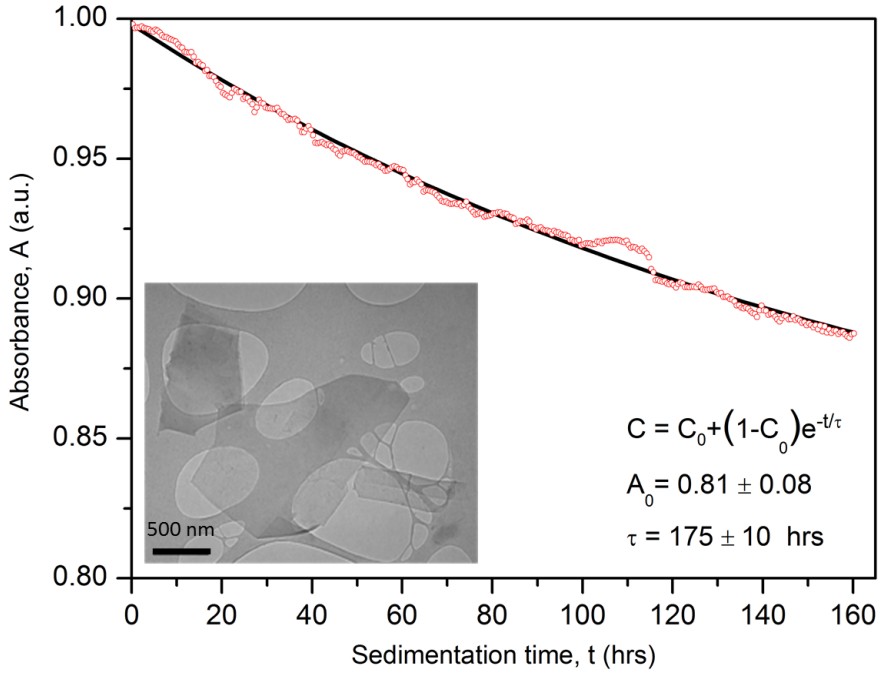

Figure 5.9: Sedimentation behaviour for graphene dispersions (diluted from 1 mg/ml to 0.01 mg/ml) in NMP. The data can be fitted well by an exponential decay (red) described by the parameters shown. Inset: A TEM image of a graphene flake following dilution.

5.3.6 *Temporal stability*

To check that these highly concentrated dispersions were stable, their stability was measured using the sedimentation apparatus previously described in chapter 3. The stock dispersion was however too concentrated to measure directly and required a dilution to allow adequate light through for a reliable transmittance measurement. The dispersion was diluted 100× with NMP, then bath sonicated for 15 mins to homogenise it. The sedimentation was measured by tracking the optical absorbance over a week (168 hrs). As one can see from figure 5.9, the dispersion was very stable showing < 15% sedimentation. The sedimentation curve could also be fitted to an exponential decay, where C_0 represents the fraction of graphene stable against sedimentation and was calculated to be $\approx 80 \pm 10$ % for this sample, with a time constant $\tau = 175 \pm 10$ hrs.

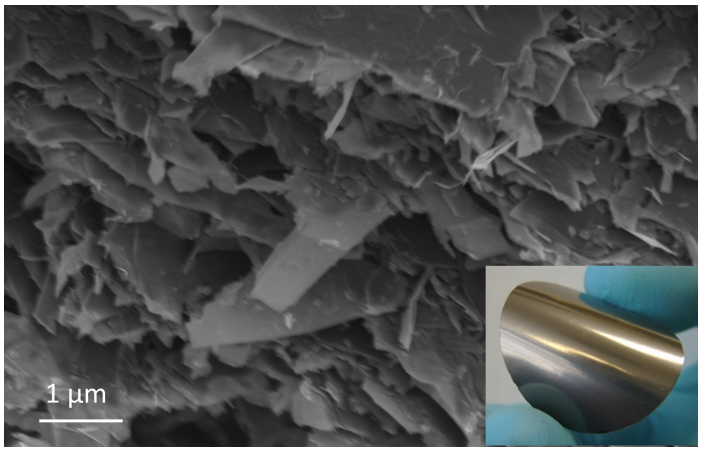

Figure 5.10: An SEM profile image of a free standing graphene film. This particular dispersion was sonicated for 96 hrs. Inset: A photograph of the free standing film.

5.3.7 *Free standing film formation*

Access to high quality, high concentration graphene dispersions facilitates a number of areas of research such as composite and film formation. This can be illustrated by preparing thick, free-standing films from dispersions sonicated for a range of times. The films were prepared by vacuum filtering the dispersions onto alumina membranes to give films $\approx$ 40 - 80 μm thick with densities of between 1200-1350 kg/m^3 (and so porosities of between 40 and 45 %) They were dried for 24 hrs in a 65°C oven followed by 48 hrs in a vacuum oven at 60°C. No annealing, washing or post treatment was performed on these films, and they were easily removed from the membrane substrate by slightly bending it. In all cases, the films displayed a shiny metallic sheen as seen in figure 5.10 inset, which was consistent with what has been observed for previously reported films of reduced GO. [71] SEM imaging of the film edge showed it to display a well defined layered morphology (figure 5.10). The flakes also are reasonably well packed, even though the porosity was relatively high.

5.4 CONCLUSIONS

In this chapter a method to prepare dispersions of graphene in NMP at concentrations of up to 1.2 mg/ml by extended sonication was demonstrated. The flake dimensions decreased with sonication time as $\frac{1}{\sqrt{t}}$, while it was found that the concentration can be directly related to the flake size. The intensity of the Raman D band increases with time as $\sqrt{t}$, and can be attributed to the formation of new edges rather than basal plane defects. These dispersions can be formed into free standing films. It is believed that this method will greatly facilitate the preparation of materials such as composites or transparent films.

6

SIZE SELECTION OF GRAPHENE FLAKES BY CONTROLLED CENTRIFUGATION

6.1 INTRODUCTION

Solvent or surfactant exfoliated graphene gives defect-free flakes but with a relatively low monolayer content. Each method results in dispersions with concentrations of up to a few mg/ml, and can be produced up to liter quantities. [69] However both methods have one very serious weakness; they tend to produce small flakes. Dispersed GO is generally produced as flakes with lateral size ~100s of nm, while solvent or surfactant exfoliated graphene is usually characterised by flake size ~1 micron. This is a significant problem. Liquid exfoliation of graphene is usually presented as a method to produce graphene in large quantities for applications such as in composites or films. However, many of these applications require flakes which are considerably larger than those currently available. For example, Gong et al recently showed that in order to produce effectively reinforced graphene-polymethylmethacrylate composites, the flake length would have to be a few microns or greater. [4] Currently available exfoliated graphene is usually significantly smaller than this, which partly explains why most graphene composite papers describe reinforcement values much lower than the theoretical limit [154] of $dY/dV_f \sim 1$ TPa where Y is the composite modulus and V_f is the graphene volume fraction. [155–164]

Alternatively, conducting graphene networks have been mooted as potential transparent electrodes or supercapacitor electrodes. However, the conductivity of such networks is limited by interflake junctions. [165] Smaller flakes result in more junctions and thus lower conductivity. [166] Thus, there is a real need to increase the size of the dispersed flakes. Ideally, optimisation of the dispersion/exfoliation process to give larger flakes would be most suitable. However, while some progress has been made

in this area, it is worth exploring methods to post-treat existing dispersions to select flakes by size. Green et al have already demonstrated that surfactant-exfoliated flakes can be sorted by thickness using density gradient centrifugation. [115] However to our knowledge, size selection has not been demonstrated for lateral size i.e. flake length. In this chapter, a method is demonstrated to take an existing dispersion of graphene in a solvent and separate flakes by size, using controlled centrifugation. A set of dispersions with mean flake lengths varying from 1 to 3.5 microns were prepared. The method is versatile and can easily be applied to surfactant stabilised graphene or indeed any exfoliated layered compound. [13]

6.2 EXPERIMENTAL PROCEDURE

1.65 g of graphite powder (Sigma Aldrich) was sonicated in 500 ml of NMP (C_I= 3.3 mg/ml) in a sonic bath for 168 hrs. This was the stock dispersion used for all experiments. After each centrifugation, 80% of the supernatant was pipetted off. TEM measurements were made on samples prepared by drop casting a few drops of dispersion on to a holey carbon grid. Thin films for Raman analysis were prepared by vacuum filtration of the dispersion through a porous membrane (PVDF, pore size of 0.45 µm). Raman measurements were performed using a 633 nm wavelength laser.

6.3 RESULTS AND DISCUSSION

While liquid phase exfoliation generally results in flakes which are small on average, < 500 nm, the flake size distribution can be quite broad. In this chapter, methods to post-treat dispersions of exfoliated graphene to predominately select flakes from the upper end of the distribution is demonstrated. However, to achieve this, the baseline flake size distribution achieved was determined by using the standard dispersion techniques.

6.3.1 *Normal dispersion properties*

A stock volume of graphene-NMP dispersion was prepared as detailed in the experimental section above. As a baseline, 20 mls of dispersion was centrifuged at 500 rpm for 45 minutes. The concentration of the supernatant was measured by optical absorption to be 0.45 mg/ml. [3] TEM analysis showed the supernatant to be rich in multilayer graphene flakes with a typical example shown in figure 6.1. From the TEM images, the length for ~90 flakes was measured. In addition, the flake thickness was estimated (i.e. the number of stacked monolayers per flake, N) using the edge counting method. [3] These data are summarised in the histograms in figure 6.2. The flake length varied from ~150 nm to ~4 μm (mean 1.1 μm), while the flake thickness varied from 1 to 6 monolayers (mean 2.8) and is typical of what is found for sonicated solvent-exfoliated graphene. [2, 3, 7, 120] Taking these as the baseline, we aimed to increase the dimensions of the flakes .

However, it is important to point out that these are not absolute limits because such a small sample is extremely unlikely to contain the largest and smallest flakes in the distribution. Thus, small populations of flakes outside these limits probably exist, although they were not observed during the statistical analysis. In addition Raman analysis of a film prepared by vacuum filtration of this dispersion gave a spectrum typical of graphene. The I_D/I_G band ratio was larger than that of the starting powder by ~0.2, a result which is consistent with small defect free flakes. [3, 62, 80]

6.3.2 *Controlled centrifugation*

While size selection can be achieved by chromatography, [167] this method usually gives limited quantities of size selected material. Thus, for practical reasons, a controlled centrifugation approach was adopted. As seen in chapter 5, for centrifuged graphene dispersions, the average lateral flake size decreased as the centrifugation rate (rpm) was increased. [3, 80] This meant that centrifugation at a high rate results in the separation of small flakes which remain dispersed from large flakes that sediment

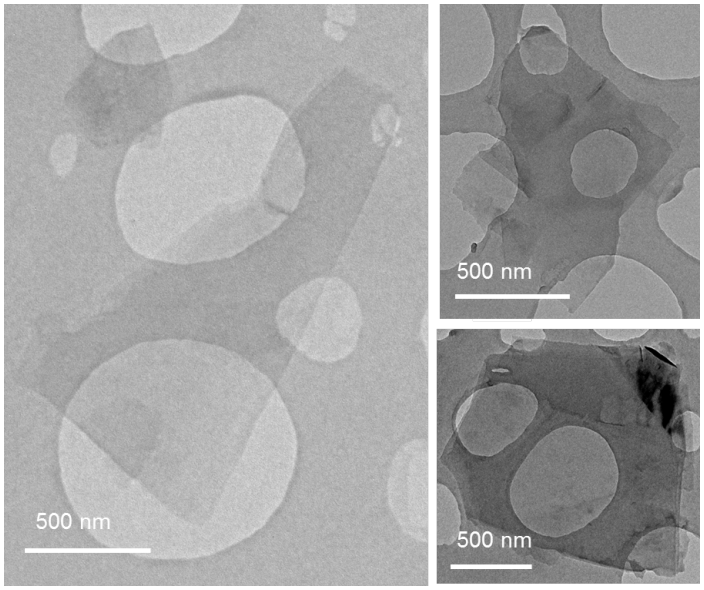

Figure 6.1: TEM images of exfoliated flakes prepared by bath sonication and centrifuged at 500 rpm without size selection.

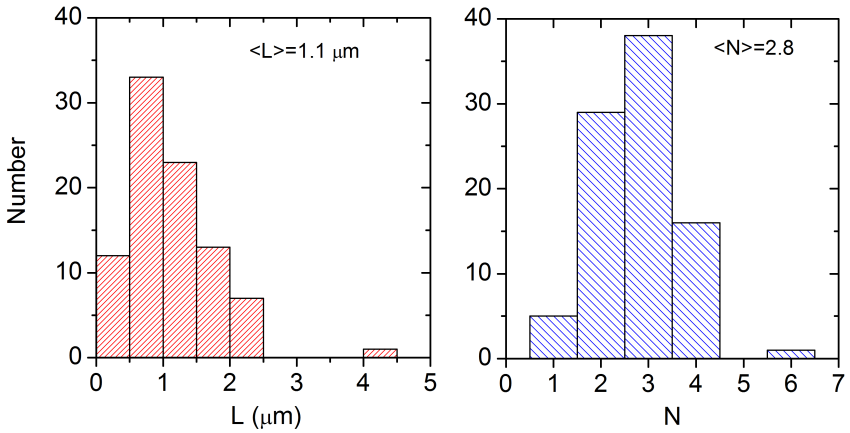

Figure 6.2: Histrograms of flake lengths, L, and flake thicknesses for the flakes, N, which is expressed as the number of stacked monolayers per flakes. These distributions represent the flakes found in the normal dispersion dicsussed above (figure 6.1).

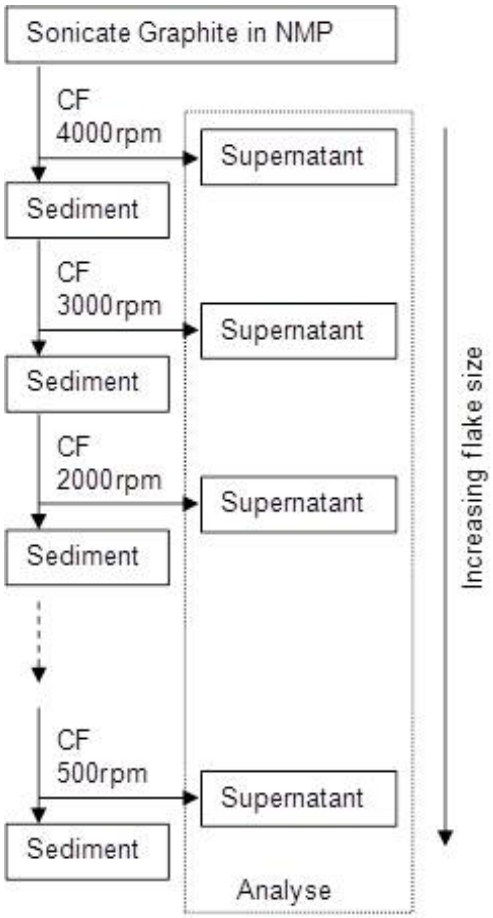

Figure 6.3: Schematic of controlled centrifugation process.

out. The sediment can be redispersed resulting in the flakes being separated by size into two different dispersions. It is noted that the dispersions of sonicated graphite always contain some unexfoliated graphitic crystallites. [2] These must be removed by a centrifugation step, with 500 rpm usually enough to remove the graphitic crystallites while leaving the flakes dispersed. Thus, when redispersing the sediment it is always necessary to centrifuge. However, one can choose the centrifugation rate. If one chooses 500 rpm to remove only the crystallites, the result will be that the initial supernatant will contain small flakes, the redispersed centrifuged sediment with medium sized flakes, and a second sediment containing large flakes and crystallites. This suggests that controlled centrifugation can potentially act as a size selection mechanism. To test this, a controlled centrifugation-based, size selection procedure was designed and is summarised in figure 6.3.

To begin, a stock dispersion was prepared using the same conditions mentioned in the experimental procedure, except we centrifuged the sample at 4000 rpm (all samples were centrifuged for 45 mins). The supernatant was set aside and the sediment redispersed in 16 mls NMP by bath sonication for 15 mins. This redispersed sediment was then centrifuged at 3000 rpm, the supernatant was decanted and set aside, and the sediment again redispersed in 16 mls NMP. This procedure was repeated a further four times, centrifuging the redispersed sediment at 2000, 1000, 700 and 500 rpm, each time collecting the supernatant. After the 500 rpm centrifugation, the procedure was stopped, as it was found that 500 rpm was the minimum centrifugation rate required to remove unexfoliated graphitic crystallites.

6.3.3 *Analysis of dispersion quality*

Each of the supernatants were then analysed by absorption spectroscopy to measure the dispersed concentration. It is worth noting that to achieve a range of size separated samples, it was necessary to centrifuge at successively lower rates. It was found, that if the procedure was attempted with the same centrifugation rate at each step, the same flake size will be achieved in all supernatants, albeit at a reduced concentration. Shown in figure 6.4 are the dispersed concentrations as a function of final centrifugate rate experienced by the sample. The concentration falls from a high value of ~0.17 mg/ml for the 4000 rpm sample to a constant value of ~0.05 mg/ml. The final sample, centrifuged for the last time at 500 rpm displayed a slightly higher concentration of ~0.1 mg/ml.

6.3.4 *Defect analysis*

In addition, the supernatants were vacuum filtered to form thin films which were analysed by Raman spectroscopy. A typical Raman spectrum measured on a film prepared from the sample whose final CF rate was 500 rpm is shown in figure 6.5 inset. These spectra have the D, G and 2D bands typical of graphitic material. Similar

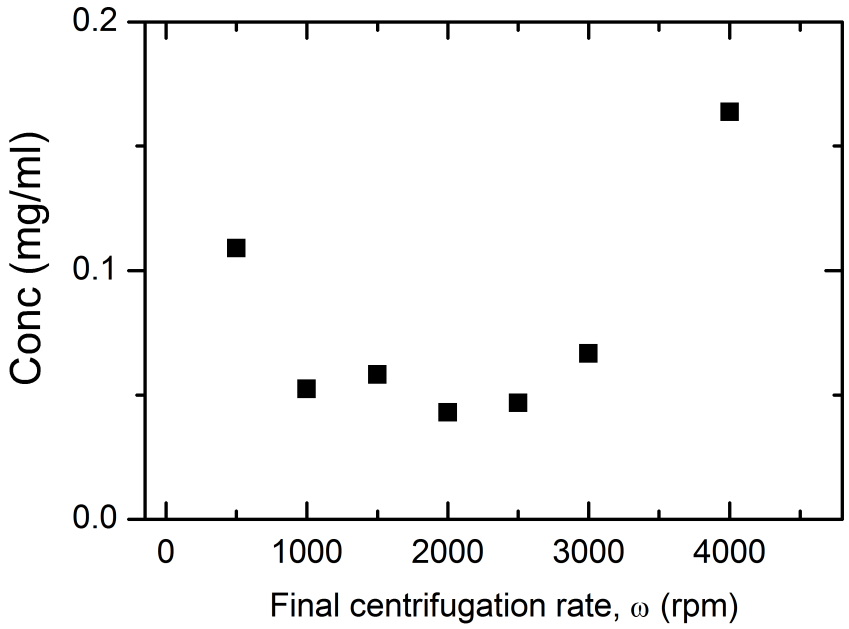

Figure 6.4: Dispersed concentration measured by absorption spectroscopy as a function of final centrifugation rate.

to chapter 5, the ratio of the intensities of the D and G bands, I_D/I_D can give some information about the sample. This ratio decreases from ~0.22 to ~0.08 as the final CF rate is decreased from 4000 to 500 rpm. For solvent exfoliated graphene flakes, this band is thought to be associated with the presence of flake edges and so is linked to the flake length by

$$I_D/I_G - (I_D/I_G)_{powder} = k/L \tag{6.1}$$

where k is a constant. [3, 7] Thus the decrease in I_D/I_G with decreasing rpm is a manifestation of increasing flake size.

6.3.5 *Measurement of flake dimension with centrifugation rate*

The increase in flake length with decreasing (final) rpm can be confirmed by TEM analysis of the 3000, 1000 and 500 rpm samples. Shown in figures 6.6A-E are typical TEM images for the 3000 and 500 rpm samples. It is immediately clear from the images that the 3000 rpm flakes are much smaller than the 500 rpm ones. To confirm this, the individual flake length, L, and the individual flake thicknesses, N, for ~50-100 flakes

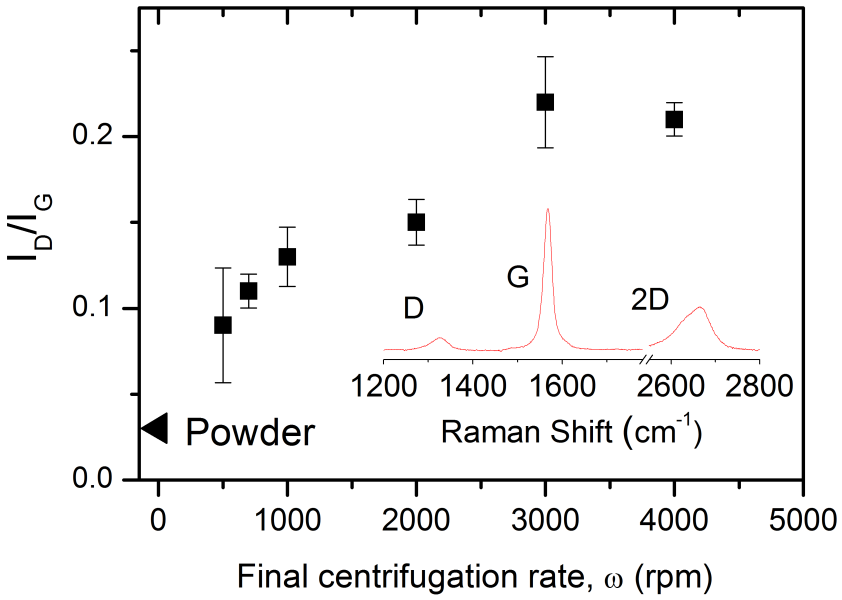

Figure 6.5: Ratio of Raman D:G bands measured on films prepared from size selected dispersions as a function of final centrifugation rate. Inset: Raman spectra for the film of size selected flakes prepared after a final centrifugation at 500 rpm.

for each CF rate was measured and is shown in figure 6.7. It is clear from this data that L increases as the final CF rate decreases. The mean values of L were measured to be 3.3 ± 1.2, 1.6 ±0.2 and 0.94 ± 0.1 μm for the 500, 1000 and 3000 rpm samples respectively as shown in figure 6.8.

6.3.6 *Correlation of flake dimension with I_D/I_G and centrifugation rate*

This data, in combination with the Raman data, can be used to estimate k (in equation 6.1) by plotting I_D/I_G versus $\frac{1}{<L>}$ (figure 6.8). This gives a value of k = 0.17 ± 0.05, slightly different to the previously found value of 0.26, in chapter 5 figure 5.8. [3, 7] This fit also gave a band intensity ratio for the powder of $(I_D/I_G)_{powder}$ = 0.037, which is in good agreement with the measured value of 0.03. The reason for this discrepancy is unclear although it is noted that different graphite was used here (Aldrich) compared with the previous work (Branwell).

Equation 6.1 can also be used to estimate the flake length from the Raman data as shown in figure 6.9. This data shows a continuous increase from ~1 μm for the 4000

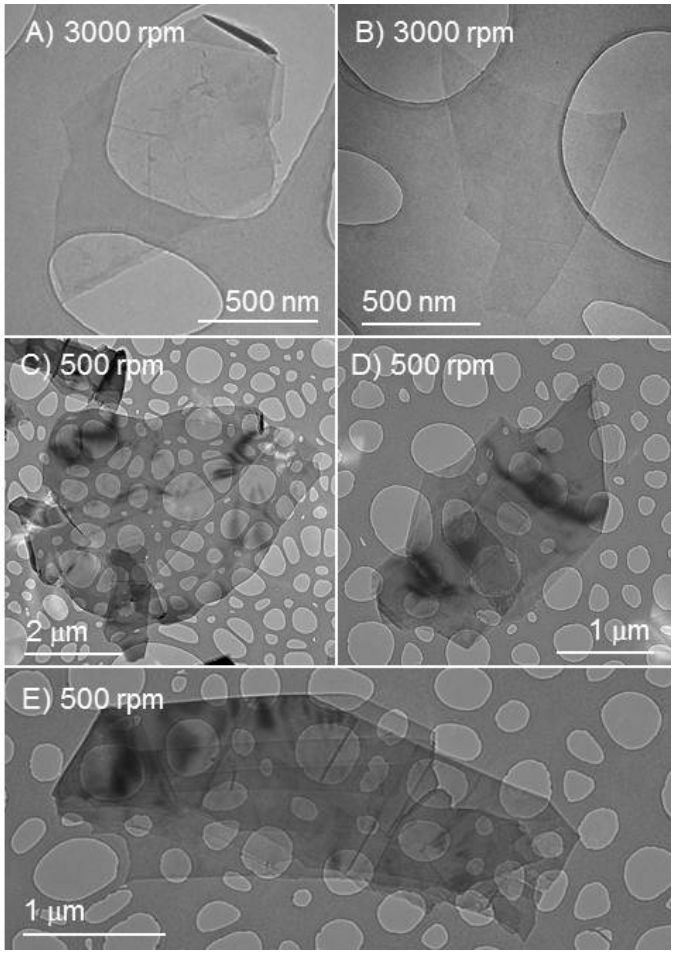

Figure 6.6: TEM images of flakes prepared during the controlled centrifugation process shown in figure 6.3. The final centrifugation rate was 3000 rpm for A & B) and 500 rpm for C-E).

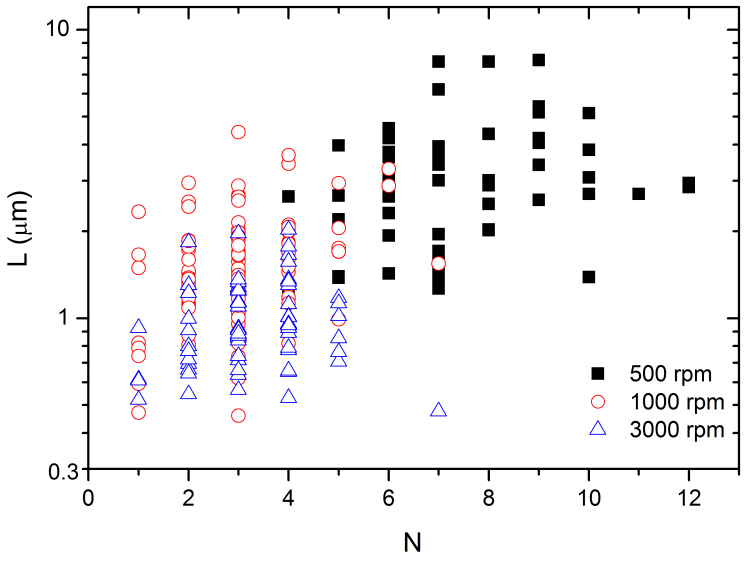

Figure 6.7: Individual flake length plotted versus estimated flake thickness (number of monolayer, N) for dispersion with final centrifugation rates of 500, 1000 and 3000 rpm

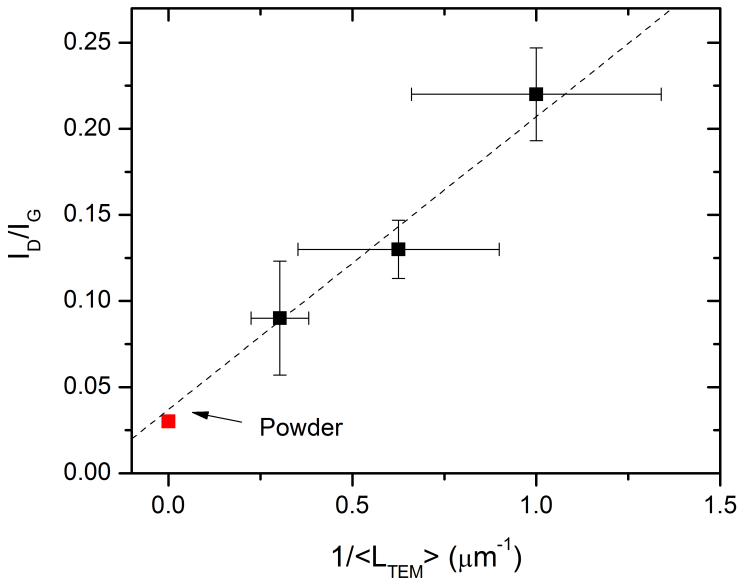

Figure 6.8: The Raman D/G band intensity ratio plotted versus inverse mean flake length for the bath sonicated 3000, 1000 and 500 rpm samples. The dashed line represents $I_D/I_G - (I_D/I_G)_{powder} \approx 0.17/L$. The error associated with the slope is $\pm$ 0.05. N.B. this slope differs from the previously reported value of 0.26. [3]

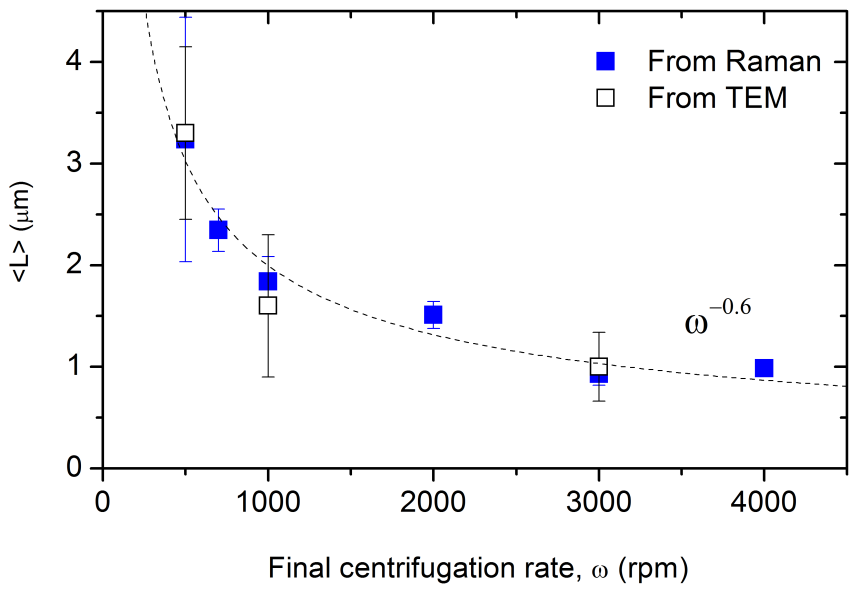

Figure 6.9: Mean flake length as measured from TEM and as estimated from both Raman and TEM. The dashed line indicates an empirical scaling behaviour of $\omega^{-0.6}$.

rpm sample to ~3.5 μm for the 500 rpm sample. It can be noted empirically, that the flake length scales with final CF rate as $\omega^{-0.6}$.

While the mean values of N were 3.2 $\pm$ 0.6 and 3.0 $\pm$ 0.4 respectively for the 3000 and 1000 rpm samples, similar to the normal dispersion, <N> was 7.3 $\pm$1.1 for the 500 rpm sample, which is considerably larger. This means that the flake aspect ratio (here defined as length/thickness i.e. L/(N $\times$ 0.35nm)) does not necessarily increase monotonically with final CF rate. In fact the measured aspect ratios were 990 $\pm$ 150, 1680 $\pm$ 270 , 1310 $\pm$ 140, 1180 $\pm$ 240 for the 3000 rpm, 1000 rpm, 500 rpm and normally dispersed samples respectively. In spite of the slightly increased thickness of the 500 rpm flakes, their increased length will be advantageous for a range of applications from mechanical composites [4] to conducting thin films [168]. Their thickness varied in the range 6 $\leq$ N $\leq$ 12 while their length varied in the range 1.2 μm $\leq$ N $\leq$ 7.8 μm. It is noted that the smallest flake observed in this sample were larger than the mean for the normal dispersion. In addition, it should be possible to use this size-selected sample as a starting point for further centrifugation-based treatment in order to refine the sample and narrow the length distribution.

6.4 CONCLUSIONS

This chapter demonstrated that controlled centrifugation can be used to separate graphene flakes by size. Centrifugation at high rates resulted in small flakes being dispersed but larger ones sedimenting out. The sediment was collected and redispersed. Centrifugation at a lower rate then resulted in a dispersion of slightly larger flakes and the rejection of the rest. Repeating this procedure a number of times resulted in the separation of the original dispersion into a number of fractions each with different mean flake lengths, in this case from ~1 to ~3.5 μm. Although it has been demonstrated for solvent exfoliated graphene, it can be easily extended to surfactant exfoliated graphene or indeed any exfoliated layered compound. This will be demonstrated later in chapter 8.[13]

7

GRAPHENE EXFOLIATION AND DISPERSION IN LOW BOILING POINT SOLVENTS

7.1 INTRODUCTION

Recent developments in liquid phase exfoliation of graphite to produce graphene mean that it is now possible to prepare large quantities of dispersed graphene cheaply and easily. There are two main methods to exfoliate graphene; using high surface tension solvents [2, 3, 77, 78, 120, 169] or in water using surfactants [62, 80, 115] or polymers [170] as stabilisers. These methods have been very successful and have led to a number of advances including the preparation of polymer-graphene composites, [170] facile production methods for transparent conductors [171] and the sorting of graphene by layer number. [115] However, these methods still face some problems. For example, when processing graphene from surfactant dispersions it can be difficult to remove residual surfactant. [62] Alternatively, the best solvents tend to be non-volatile [120] causing problems with processing. This is because the energetic cost of exfoliation falls as the solvent's Hildebrand solubility parameter approaches 23 $MPa^{1/2}$ (which is equivalent to saying that the surface tension approaches 40 mJ/m^2). [2, 118, 120] As discussed in chapter 3, section 3.3.1, Trouton's rule links the solubility parameter to the boiling point (T_B) through the enthalpy of vaporisation. This generally means that the best solvents tend to have high boiling points. This can make it difficult to remove solvents when processing graphene into films or composites. [2] In particular, it is virtually impossible to deposit individual flakes from solvent exfoliated graphene as aggregation tends to occur during the slow solvent evaporation. [2] While graphene dispersions in high boiling point solvents have been transferred into low boiling point solvents by solvent exchange, [172] it would be preferable to have a method which allows the direct exfoliation of graphite to give stable dispersions of graphene in low

boiling point solvents. Such a method would greatly simplify graphene exfoliation and significantly expand the number of applications of liquid exfoliated graphene.

It is noted, that if good solvents such as N-methyl-pyrrolidone (NMP) have solubility parameters of around 23 $MPa^{1/2}$ and boiling points close to 200 °C, then the logical corollary of this is that mediocre solvents have lower solubility parameters and lower boiling points. The cost of mediocrity is generally low concentration and possibly poor exfoliation quality and stability. The research presented in this chapter explores if it possible that such issues can be addressed by the optimisation of processing procedures to give good quality, high concentration, stable dispersions in low boiling point solvents.

7.2 EXPERIMENTAL PROCEDURE

All solvents used were of Chromosolv grade and were purchased from Sigma Aldrich: Acetone (product number 34850), Chloroform (product number 366919), Isopropanol (CAS 67-63-0), Cyclohexanone (product number 398241), N-methyl pyrrolidone (product number 69120) and Dimethylformamide (product number 15440). The concentration was determined using UV-vis-IR spectroscopy. Thin films were prepared by filtering the dispersion onto porous polyvinylidene fluoride (PVDF) membranes with a nominal pore size of 0.22 μm. Individual flakes were deposited onto SiO_2 using an airbrush spray gun (Evolution Airbrush, www.graphicsdirect.co.uk). The gun was held approximately 2 cm from the substrate and the graphene flakes in dispersion were carried to the substrate by an injection of nitrogen at 2 Bar pressure. The spraying was pulsed (5 second intervals) to allow for solvent evaporation. No additional heat or silanisation of the surface was required. A palladium grid reference with dots > 20 nm, was sputtered onto freshly cleaved SiO_2 (300 nm thermally grown oxide) allowing the flake positions to be recorded for subsequent characterisation. The substrate was also cleaned for 10 minutes in an oxygen plasma (Diener barrel asher) before spraying. All sonication was performed in the same low power sonic bath with a nominal power output of ~16 W.

7.3 RESULTS AND DISCUSSION

7.3.1 *Dispersion of graphene in low boiling point solvents*

Previous work in this group has demonstrated that chloroform, isopropanol (IPA) and acetone can disperse graphene at low concentration (3.4, 3.1, 1.2 µg/ml respectively). [120] While, these concentrations are far too low for most applications, such solvents have the significant advantage of having relatively low boiling points (61, 82, and 56 °C respectively). Earlier in chapter 5 it was shown that the concentration of graphene dispersed in NMP can be increased dramatically by sonicating at low power for very long periods of time. [3] Thus, in order to attempt to produce high concentrations of exfoliated graphene in these low boiling point (BP) solvents, graphite powder (initial concentration 3.3 mg/ml) was sonicated for 48 hrs in a low power sonic bath. Each dispersion was then split into three and each portion centrifuged at three different rates; 500, 2000 and 5000 rpm. The top 6 mls (out of 10 mls) was then removed by pipette. In addition, graphite powder was dispersed using identical procedures in three high BP solvents - NMP, DMF and cyclohexanone – all of which are known to exfoliate graphite. [120] In all cases, the dispersed concentration after centrifugation (CF) was measured using UV-vis-IR spectroscopy (taking the absorption coefficient to be α = 3620 mg/ml/m). The concentration of dispersed graphene for all six solvents was calculated, at three rotation rates, and was plotted in figure 7.1. Previous work has shown that higher rotation rates result in the retention of smaller flakes. [3, 80] The data for the three high BP solvents is similar with concentrations of ~1, ~0.5 and ~0.2 mg/ml obtained for CF rates of 500, 2000 and 5000 rpm. These concentrations are much higher than those originally reported for good solvents (typically ~10 µg/ml) [2, 120] and compare well to recent reports of high concentrations of graphene dispersed in NMP. [3] Likewise, the data for isopropanol and chloroform are similar with surprisingly high concentrations observed: ~0.5, ~0.2 and ~0.07 mg/ml for CF rates of 500, 2000 and 5000 rpm. Acetone gave poorer results: ~0.08, ~0.025 and ~0.01 mg/ml for CF rates of 500, 2000 and 5000 rpm. However, all three solvents show significant improvement

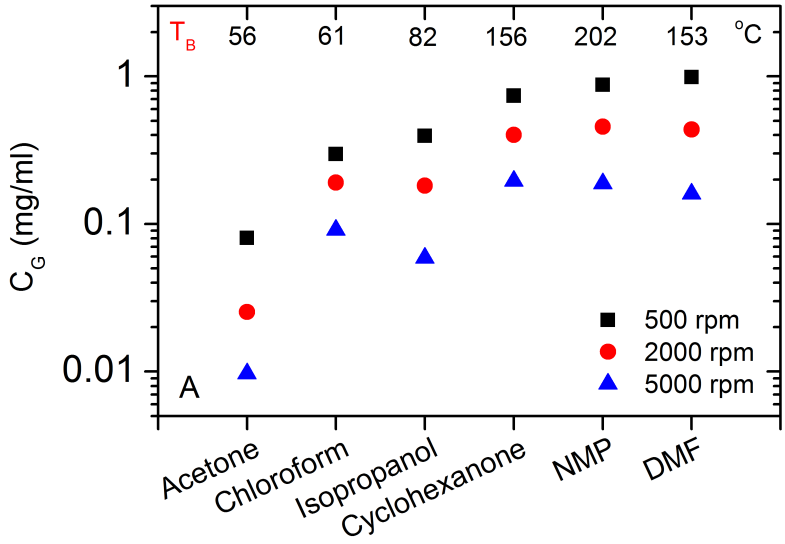

Figure 7.1: Concentration of dispersed graphene as a function of centrifugation rate for three high boiling point and three low boiling point solvents. The boiling points are shown at the top of the figure.

on previous results which gave concentrations of graphene in chloroform, IPA and acetone of 3.4, 3.1, 1.2 µg/ml respectively (all obtained with much shorter sonication time; ~30 minutes and lower initial graphene concentration, ~0.1 mg/ml). [120]

It is important to check if these relatively high concentrations are compatible with the postulated dispersion mechanism discussed in chapter 3. Previously, it was suggested that good solvents are those whose Hansen solubility parameters match reasonably well to those suggested for graphene. [118, 120] These parameters represent the dispersive, polar and hydrogen bonding contributions to the cohesive energy density of the material and measure the energy required to disperse one phase in another. [122, 173] For both carbon nanotubes [117] and graphene [120] dispersed in solvents, dispersion quality is particularly sensitive to the dispersive Hansen parameter, δ_D; successful dispersions are only achieved for solvents with 15 $MPa^{1/2} < \delta_D <$ 21 $MPa^{1/2}$. [120] Conversely reasonable dispersions can be achieved for a much wider range of polar, δ_P, and H-bonding, δ_H, Hansen parameters (from 2-3 $MPa^{1/2}$ to 17-18 $MPa^{1/2}$ in each case). [120] This suggests that the concentrations achieved in the present study should be controlled primarily by δ_D. In figure 7.2 the graphene concentration was plotted for the 5000 rpm dispersions against the solvent δ_D. The dashed curve represents the

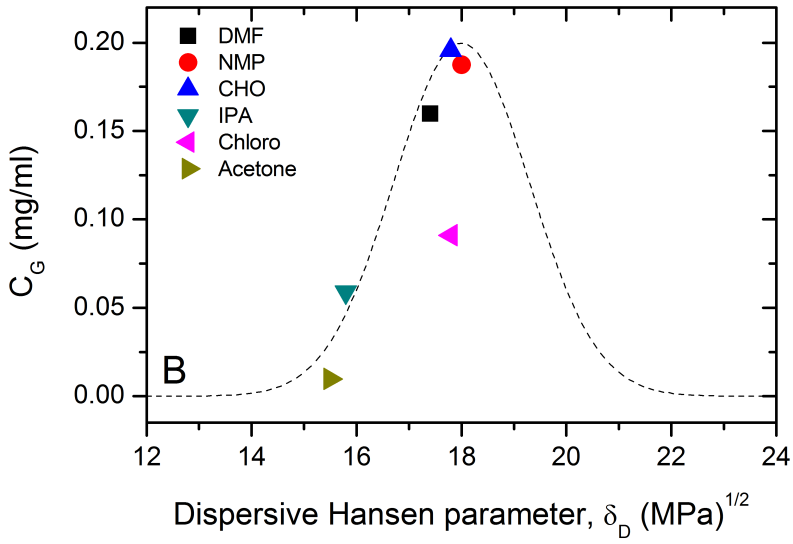

Figure 7.2: Graphene concentration (5000 rpm) as a function of dispersive Hansen parameter for the solvents shown in figure 7.1. The dashed line illustrates the behaviour found by Hernandez et al, [2] rescaled to match the data for cyclohexanone.

envelope of the data reported previously for graphene, dispersed at low concentration in a wide range of solvents. [120] With the exception of chloroform, all solvents match very well to the dashed line. We suggest that the chloroform data is significantly below the dashed line because its δ_P value of 3.1 $MPa^{1/2}$ is at the very edge of the allowed range (2-3 $MPa^{1/2}$ to 17-18 $MPa^{1/2}$). [120] This results in the reduction of the concentration of graphene in chloroform, below what would be expected by analysis of δ_D alone. By contrast the δ_P and δ_H values of the other solvents are much closer to the center of the accepted Hansen parameters range for graphene, which also shown in table 7.1.

7.3.2 *Graphene dispersion optimisation*

As discussed in chapter 5, the concentration of dispersed graphene can be achieved by increasing the sonication time, t. [3, 80] Longer sonication times result in smaller flakes which can be dispersed at higher concentrations. [3] Thus, dispersions of graphene in IPA and chloroform (initial graphite concentration of 3.3 mg/ml, 250 ml, round bottomed flask, sonic bath) were prepared for a range of sonication times followed by

Solvent	δ_D(MPa)$^{1/2}$	δ_P(MPa)$^{1/2}$	δ_H(MPa)$^{1/2}$
DMF	17.4	13.7	11.3
NMP	18	12.3	7.2
cyclohexanone	17.8	8.4	5.1
IPA	15.8	6.1	16.4
chloroform	17.8	3.1	5.7
acetone	15.5	10.4	7
graphene	18 (15-21)	9.3 (3-17)	7.7 (2-18)

Table 7.1: Dispersive, polar and Hydrogen bonding Hansen parameters for the solvents used in this work. The Hansen parameters of graphene are also shown. The bracketed figures are the approximate range of acceptable values for graphene exfoliating solvents.

centrifugation (2000 rpm for 45 minutes) and calculated their concentrations. For both solvents, the concentration increased significantly, saturating at ~0.4 and ~0.5 mg/ml for chloroform and IPA respectively (figure 7.3). As shown by the dashed lines, this increase is consistent with the $\sqrt{t}$ behaviour previously observed for NMP dispersions. [3] This suggests that the concentration is partly controlled by flake size which is, in turn, controlled by sonication time. [3] Of note, the concentration of 0.5 mg/ml is relatively high, comparing favorably with the highest concentrations observed for graphene in NMP and surfactants (1.2 and 0.3 mg/ml respectively). [3, 80]

7.3.3 *Analysis of low boiling point solvent dispersion*

Analysis of exfoliation using TEM

Subsequently, the quality of the dispersion was assessed using TEM. Shown in figure 7.4A is a TEM image of a large number of graphene flakes deposited on the TEM grid. A higher magnification image of a folded bilayer, with some smaller flakes attached is shown in figure 7.4B. Figure 7.4C shows a HRTEM image of a flake, with well defined edges, that appears to be a monolayer. Electron diffraction analysis was also

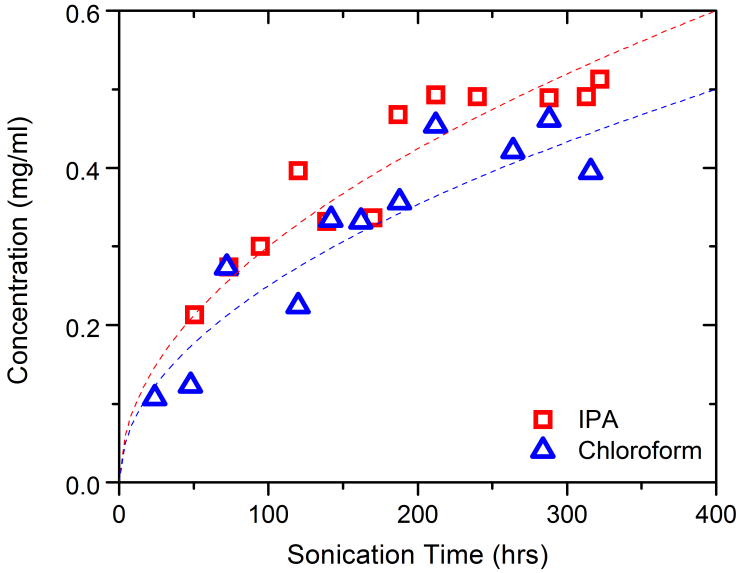

Figure 7.3: Concentration of graphene dispersed in isopropanol and chloroform as a function of sonication time. The dashed lines illustrate $\sqrt{t}$ behaviour.

performed. A diffraction pattern for a monolayer of graphene is shown in figure 7.4D to test this. It is clear that the inner set of spots ({1100}) is more intense than the secondary set ({2110}), confirming that this flake consists of a single graphene layer. [2] All the observed flakes were found to have reasonably well defined edges and appear to be of good quality with no observable holes or other damage. Both the aggregation state and the flake size distribution can be estimated by careful analysis of the TEM images. [2, 3, 80, 120] By analysis of the flake edges, an estimation of the number of layers per flake, N, for ~80 flakes, was measured. These were used to give flake thickness histograms as shown in figure 7.5. Although very few monolayers are observed in either solvent, all the flakes had 7 or less layers, demonstrating the quality of exfoliation (with <N> $\approx$ 3.2 in both solvents). The mean flake length, L, and width, w, can be measured and histograms of these quantities plotted. This data is shown in figure 7.5 for both chloroform and IPA. In chloroform, the mean flake length and width were $< L > = 0.84 \pm 0.22$ μm and $< w > = 0.36 \pm 0.9$ μm respectively. Similarly, in IPA the mean flake length and width were $< L > = 1.1 \pm 0.3$ μm and $< w > = 0.35 \pm 0.52$ μm respectively. These sizes are typical of exfoliated graphene. [2, 3, 80, 120] In addition the flakes were asymmetric with an average aspect ratio of $\left\langle \frac{L}{w} \right\rangle = 2.6 \pm 0.7$ and 3.4 ± 0.6 for chloroform and IPA respectively.

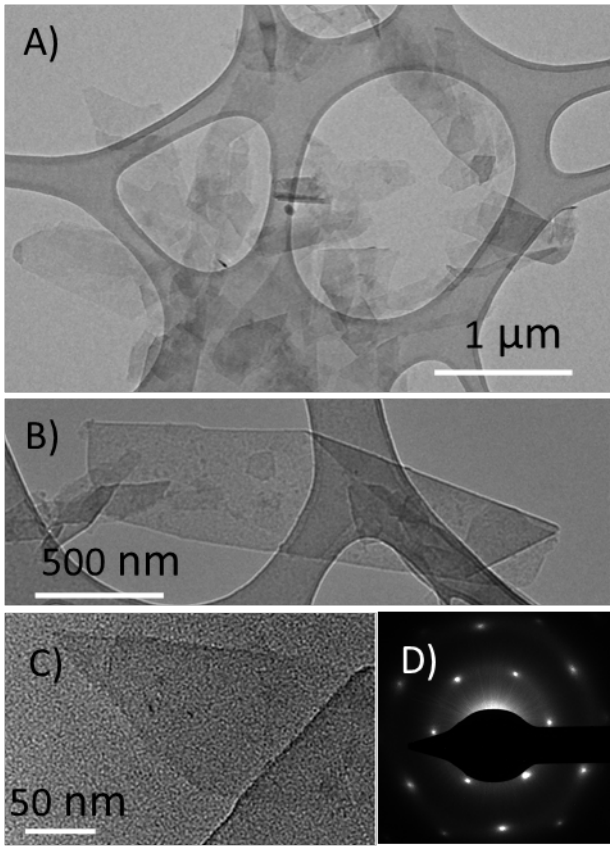

Figure 7.4: TEM analysis of graphene dispersed in IPA and chloroform. A) A TEM image of a grid coated with a large number of few-layer graphene flakes exfoliated in isopropanol. B) A TEM image of a folded bilayer graphene C) A HRTEM image of a monolayer as confirmed by the electron diffraction pattern in D).

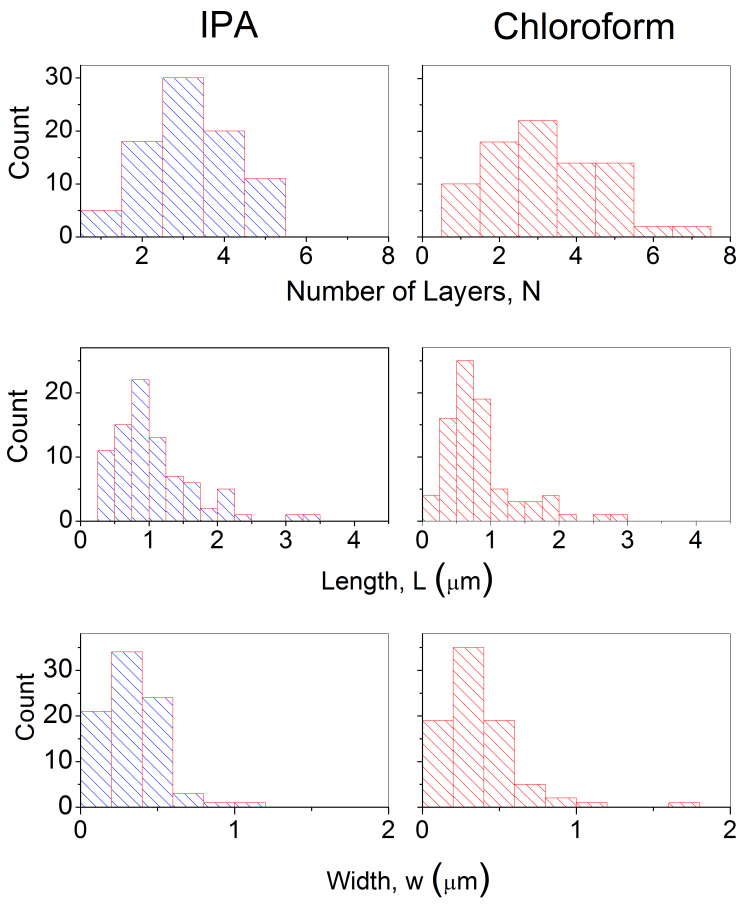

Figure 7.5: Statistical analysis of TEM images showing histograms of the number of layers per flake, N, flake length, L, and flake width w, for graphene dispersed in both IPA and chloroform.

Analysis of flake quality using Raman spectroscopy

It is also important to check for the formation of basal plane defects during sonication. Raman spectroscopy on thin films prepared by vacuum filtration of both IPA and chloroform based dispersions after 22 and 70 hrs sonication indicated their quality. Their averaged Raman spectra are shown in figure 7.6, with the graphite powder spectrum shown for comparison. The defect content is generally characterised by the ratio of the intensity of the defect band (D band, ~1300 cm^{-1}) to that of the G band (~1300 cm^{-1}), I_D/I_G. From the data one can see that this ratio increased with sonication time. While such behaviour is indicative of defect formation, such defects can be in the basal plane or can represent new edges formed as the average flake size is reduced by continuing sonication. It is believed that the latter case can be identified by the time dependence of the difference between I_D/I_G for exfoliated graphene versus graphite powder. [3, 80] We denote this difference as $\Delta I_D/I_G(t) = I_D/I_G(t) - (I_D/I_G)_{powder}$. $(I_D/I_G)_{powder}$ was measured to be 0.14 for the graphite used in this study. The formation of edges is characterised by $\Delta I_D/I_G(t) \propto (t)^{1/2}$, [3] which is illustrated in the inset of figure 7.6. This can be checked by noting that earlier in chapter 5, it was shown that for solvent dispersed graphene, the relationship between I_D/I_G and flake size is known: $\Delta I_D/I_G$= 0.065 $\left[< L >^{-1} + < w >^{-1}\right]$, where the dimensions are measured in microns. [3] From the TEM analysis we know that $\left\langle \frac{L}{w} \right\rangle \approx 3$, allowing us to approximate: $\Delta I_D/I_G \approx 0.26 \ / < L >$. Combining this with the fit in the inset of figure 7.6 inset gives $< L > = 8.7 \ /(t)^{1/2}$, where L is in μm and t in hrs (this is reasonably close to the known expression for NMP dispersions: $< L >$ =14.6/$(t)^{1/2}$). [3] This allows an estimate of the flake length for the 48 hrs sample to be 1.25 μm, which is consistent with the measured value of 1.0 μm. Thus the Raman data strongly suggests that the newly created defects are new flake edges rather than body defects. This therefore implies that the exfoliation process is not overly destructive and yields good quality flakes.

In addition, the shape of the Raman 2D band (~ 2700 cm^{-1}) is different from that of graphite and is consistent with few-layer graphene as discussed earlier in chapter 4

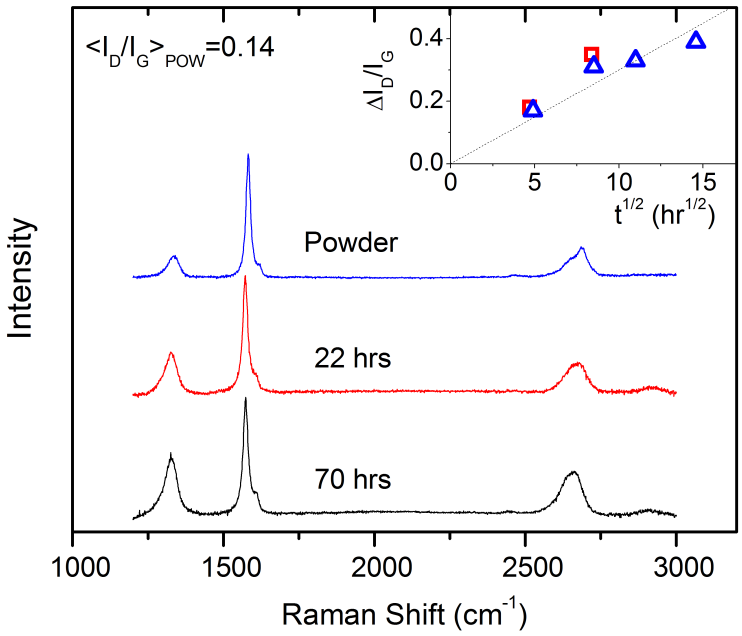

Figure 7.6: Raman spectra of the starting powder and of the films of graphene (IPA) deposited on PVDF membranes for sonication times of 22 and 70 hrs. Inset: The increase in I_D/I_G compared to that for the graphite powder, $\Delta I_D/I_G$, as a function of the square root of sonication time for both IPA (squares) and chloroform (triangles) dispersions. A straight line indicates that the defects being formed are associated with new edges.

figure 4.2. [136] This indicates that while flakes must aggregate during film formation, the resultant stacking is not ordered AB stacking but random. [143]

7.3.4 *Dispersion stability*

The rate of sedimentation of these dispersions was measured by monitoring the dispersion concentration optically, due to the fact that any unstable material sediments out (NB this is performed after centrifugation). [126] When dispersed in good solvents such as NMP, graphene is particularly stable. [3, 120] However, when dispersed in mediocre solvents, one expects some degree of sedimentation. Sedimentation measurements were carried out for a number of graphene/IPA dispersions (7 independent dispersions) and graphene/chloroform dispersions (4 independent dispersions). Typical sedimentation curves for graphene dispersed in IPA and chloroform are shown in

figure 7.7. For chloroform, an initially rapid sedimentation had saturated after ~100 hrs with ~75% of the graphene remaining stable. In the case of IPA a slow steady sedimentation was observed (see curve IPA-1). This tended to saturate after >200 hrs with 96% of the graphene stably dispersed. However, it can be noted that occasionally (2 out of 7) sedimentation curves like that labelled IPA-2 are observed for graphene dispersed in IPA. In such cases, a steady decrease in concentration was observed with no saturation observed after hundreds of hours. Such behaviour seems to be associated with wet or aged IPA and can be avoided by using fresh solvent and molecular sieves to remove any water. It has been shown that, during sedimentation, the concentration remaining dispersed can be approximated by,

$$C(t) = C_0 + (C_T - C_0)e^{-t/\tau} \tag{7.1}$$

for a system with one stable phase (concentration, C_0) and one sedimenting phase (concentration, C_T - C_0 where C_T is the total initial concentration). [126] Equation 7.1 fits extremely well to both data sets (dashed lines figure 7.7). The chloroform dispersions were characterised by values of C_0/C_T in the range 0.67 - 0.96 (mean 0.80) and values of τ between 11 and 19 hrs with an outlying value of 88 hrs (overall mean 34 hrs). The stable IPA dispersions were characterised by values of C_0/C_T in the range 0.93 - 0.97 (with one outlying value of 0.69, overall mean 0.92) and values of τ between 45 and 221 hrs (overall mean 126 hrs). In addition, the unstable IPA dispersions (IPA-2) were characterised by C_0 = 0 and τ ~880 hrs.

Discounting the unstable dispersions which can be attributed to impure solvent, the C_0/C_T values tell us that these dispersions are extremely stable with the vast majority of graphene remaining dispersed over very long time scales. The main difference between solvents is in the time constants. These were tens of hrs for chloroform and hundreds of hours for IPA. Short time constants suggests that the amount of sedimenting material is relatively large. [126] This suggests the unstable phase in the chloroform dispersions to be large graphitic flakes which were not fully removed after centrifugation. Such large objects would tend to sediment with a short time constant. However, for IPA the time constants are much longer suggesting smaller sedimenting objects. Here, we suggest the sedimenting phase are small graphene flakes.

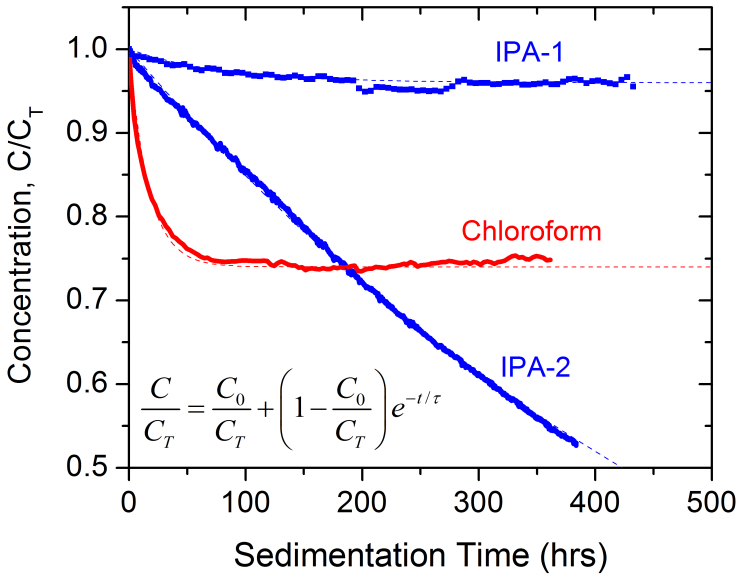

Figure 7.7: Sedimentation curves for graphene dispersed in isopropanol and chloroform after centrifugation. C/C_T is the concentration normalised to the total initial concentration. The dashed lines are fits to the inset equation.

This hypotheses can be tested by performing TEM on the sediment formed after the sedimentation experiments (~360 hrs). These data sets are shown in figure 7.8 and confirm that relatively large graphitic flakes sediment out of chloroform while the unstable objects in the isopropanol dispersions are smaller multilayer graphene flakes.

7.3.5 *Deposition of graphene onto substrates*

One of the biggest problems with graphene exfoliation in high boiling point solvents is the difficulty associated with the deposition of individual flakes. The reason for this is that during the slow evaporation of the solvents, there is plenty of time for flake aggregation. This work addresses this issue by exploiting the ease of solvent removal from graphene exfoliated in volatile systems such as IPA. The samples were prepared by spraying the concentrated dispersion directly onto oxygen plasma cleaned SiO_2 with an airbrush spray gun. The substrate was analysed after deposition by AFM.* A widefield image of the substrate is shown in figure 7.9A. This image shows large numbers of flakes distributed reasonably uniformly over the substrate. Under these

* AFM measurements were performed by Peter N. Nirmalraj

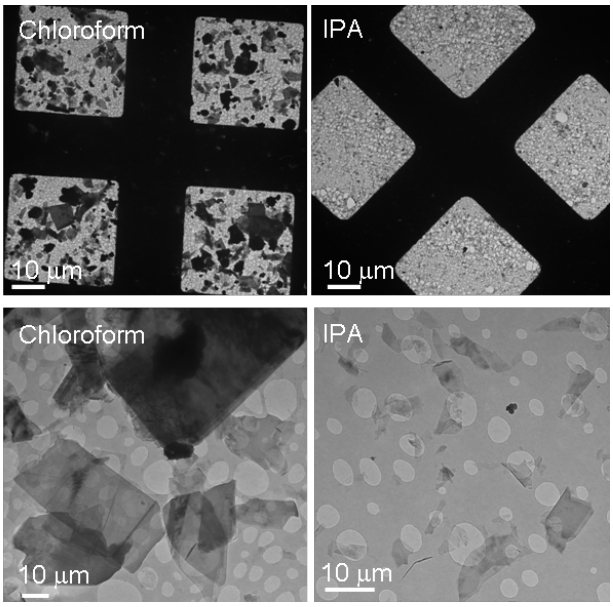

Figure 7.8: TEM images of the sediment formed after a sedimentation experiment performed on dispersions prepared with Chloroform and IPA. Note how the flakes in the chloroform sediment are significantly larger then those in the IPA sediment.

conditions, >10 flakes of length ~1 μm are deposited per 10 μm x 10 μm square. Figure 7.9B shows a higher magnification image of this substrate. The flakes are well defined but show some evidence of aggregation, which likely occured during the spraying process. Analysis of the flake heights showed them to be typically between 2 and 10 nm, corresponding to multiple layers. The fact that these heights are significantly greater than the thicknesses suggested by the TEM analysis confirms that, as indicated by the AFM images, aggregation occurs on deposition. However, it can be noted that this aggregation is much less than what was observed when depositing from NMP or other high boiling point solvents. It was confirmed that these flakes were few-layer graphene by Raman mapping. The Raman spectra were recorded from spots (~1 μm in diameter) that were arranged in the grid with a separation of 0.5 μm. Analysis of individual Raman spectra showed them to be compatible with few layer graphitic material. By integrating between 1200 and 2800 cm^{-1} and plotting the integrated value as a function of position, a Raman map was generated as shown in figure 7.9C. This area corresponds to that measured by AFM in figure 7.9B. The agreement between

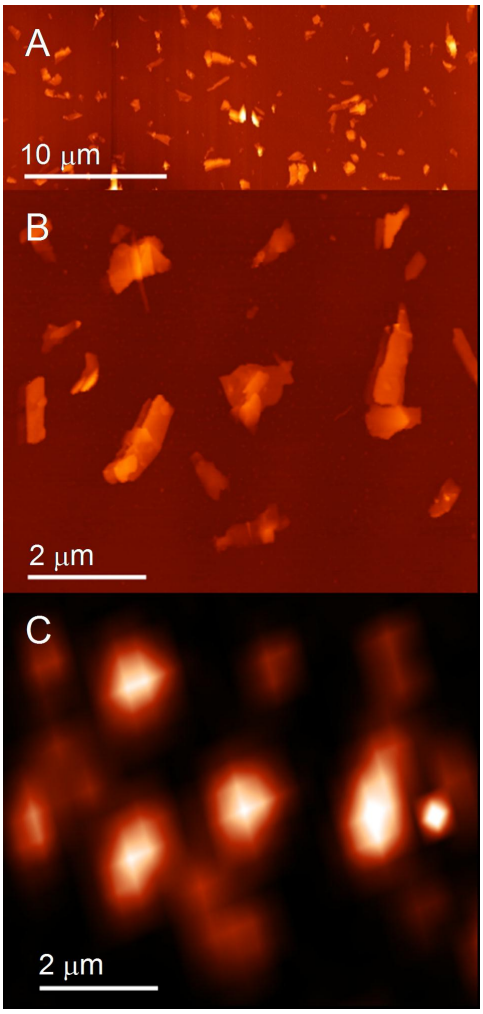

Figure 7.9: A) Wide angle AFM scan of graphene flakes spray deposited onto SiO_2 from IPA. B) A zoom in to a portion of this image. C) A Raman map of the region in B). This map plots the integral of the Raman scan between 1200 and 2800 cm^{-1} plotted on a point by point basis.

figures 7.9B and C is extremely good confirming that the objects analysed by AFM are indeed graphene.

7.3.6 *Correlation of flake dimension and Raman spectroscopy*

Finally, the data contained in the Raman map can be used to further study the correlation between flake size and Raman D:G ratio. This was done for 23 flakes that were contained in the 10 μm x 10 μm region seen in figure 7.9B. Their flake size and

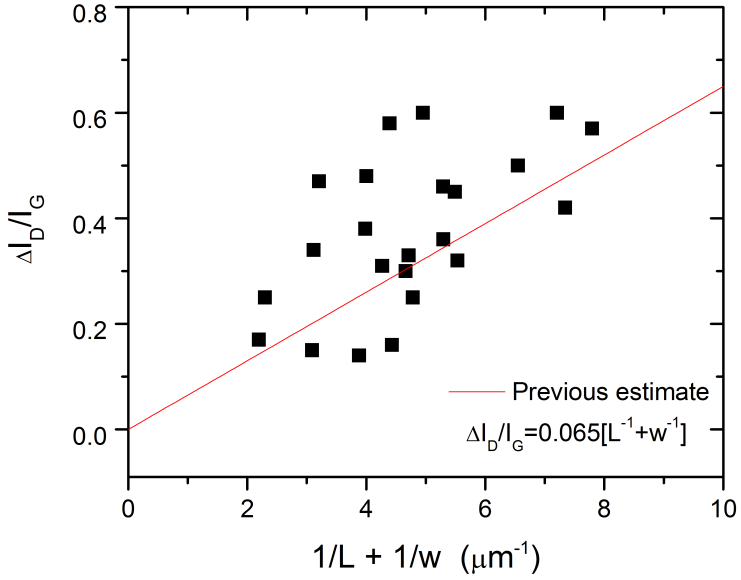

Figure 7.10: $\Delta I_D/I_G$ for individual flakes deposited on SiO_2 from IPA plotted as a function of $< L >^{-1} + < w >^{-1}$. A straight line on this plot indicates that the defects responsible for the D band are predominately edge defects. We note that this data is consistent with our previous data (measured on graphene films) as indicated by the solid line. The scatter of the data above the line is indicative of aggregation.

the Raman D:G band ratio was measured and plotted as $\Delta I_D/I_G$ versus $\frac{1}{L} + \frac{1}{w}$, and shown in figure 7.10. Although there is considerable scatter, it is clear that $\Delta I_D/I_G$ does indeed scale with $\frac{1}{L} + \frac{1}{w}$. As described above, previous measurements on graphene films showed that $\Delta I_D/I_G = 0.065\left[\left\langle\frac{1}{L}\right\rangle + \left\langle\frac{1}{w}\right\rangle\right]$. This curve has been superimposed on the graph and is consistent with the data (red line in figure 7.10). It can be noted that much of the scatter comes from data with values of which are considerably higher than expected. This can be explained by aggregation effects. In many cases figure 7.9B shows small flakes adsorbed on top of lager flakes. However, while L and w were measured for the overall aggregate size, the Raman signal includes contributions from all flakes in the aggregate. The contribution from the smaller adsorbed flakes will increase the D band intensity meaning that $\Delta I_D/I_G$ will be larger than expected for large individual flakes alone.

7.4 CONCLUSIONS

To conclude it has been demonstrated that dispersion of graphene in volatile solvents such as acetone, chloroform and isopropanol can be optimised. At moderate centrifugation rates, concentrations as high as 0.5 mg/ml were achieved. These dispersions are reasonably stable with >80% of dispersed phase remaining after 100 hrs. The dispersed concentration increases with the square root of sonication time. This behaviour is indicative of sonication induced scission and suggests that the concentration is controlled by flake size. The exfoliation state is good; isopropanol dispersions display only flakes with less than 5 layers. Raman measurements show the flakes to be relatively free of basal plane defects. Of note, dispersion in volatile solvents facilitates the deposition of graphene flakes onto substrates by spraying. While some aggregation was observed, the deposited flakes tend to be more numerous and thinner than for flakes deposited with high boiling point solvents. This research will make solvent exfoliation of graphene viable in a much wider variety of situations.

8

PREPARATION OF HIGH CONCENTRATION DISPERSIONS OF EXFOLIATED MOS_2 WITH INCREASED FLAKE SIZE

8.1 INTRODUCTION

In this chapter, this research aims to overcome three main shortcomings in preparing MoS_2 dispersions by liquid phase exfolaition. From the literature, it it noted that both solvent [13] and surfactant-exfoliated [113] transition metal dichalcogenides (TMD) tend to exist as multilayer stacks with few, if any, individual nanosheets. This is in contrast to ion intercalation and exfoliation methods which have recently been shown to give reasonably large, monolayer populations. [100] Secondly, the dispersed concentrations tend to be well below 1 mg/ml, which is too low for applications requiring large quantities of exfoliated material. And finally, the lateral flake size is relatively small, typically between 200 - 400 nm. This is probably due to sonication induced scission but can limit the potential of these materials in a range of applications from composites to transistors or sensors. Thus, it will be important to find ways to modify solvent (and surfactant) exfoliation methods to improve the exfoliation state (i.e. decrease the average flake thickness) and increase both the dispersed concentration and the flake size. In this chapter, two of these problems will be addressed. It will be shown that the sonication conditions can be controlled to give relatively large flakes at relatively high concentration. In addition, it is shown that the flakes can be further size selected to give dispersions with a range of mean flake sizes.

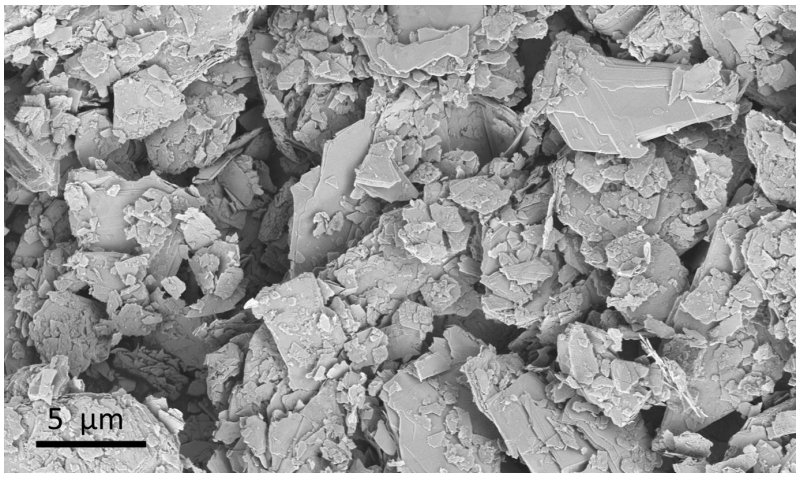

Figure 8.1: SEM image of the starting MoS_2 powder

8.2 EXPERIMENTAL PROCEDURE

The MoS_2 powder and NMP used throughout these experiments were purchased from Sigma Aldrich (CAS 69860 and CAS M79603). The initial MoS_2 concentration experiments were performed by adding the powder to 20 mls of NMP in a 100 ml capacity, flat bottomed beaker. These samples were sonicated continuously for 60 minutes using a horn probe sonic tip at 25 % amplitude (of 750 W). They were then centrifuged at 1500 rpm. For the concentration versus sonication time experiments, 100 mls of NMP was added to 10 g of MoS_2. The sonic tip was pulsed for 8 seconds on and 2 seconds off, to avoid damage to the processor and reduce solvent heating and thus solvent degradation. During sonication, 5 mls aliquots were removed at certain time intervals and centrifuged. All samples for TEM were diluted and prepared by pipetting a few mls of the dispersion onto the holey carbon grid. Statistical analyses of the flake dimensions was performed for 50 nanosheets. High resolution imaging of the flakes was also performed to ensure the quality of the nanosheets was preserved.

8.3 RESULTS AND DISCUSSION

In order to maximise the concentration of dispersed MoS_2 nanosheets, it will be necessary to optimise the dispersion parameters. Throughout this chapter the solvent

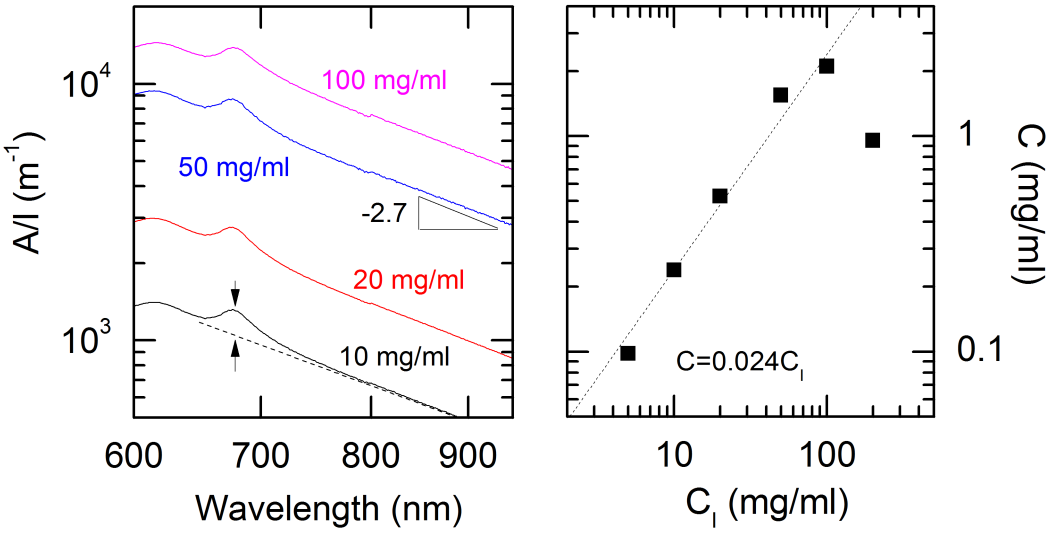

Figure 8.2: Absorption spectra of MoS_2 dispersions prepared with various starting concentrations. Note that each spectrum is superimposed on a scattering background. The concentration was estimated from the absorbance above an extrapolated background as shown by the arrows using an absorption coefficient of 1020 ml/mg/m. The dispersed concentration is also plotted as a function of initial MoS_2 concentration.

N-methyl-pyrrolidone (NMP) was used as it is known to be an excellent solvent, not only for MoS_2 [13, 124, 174], but also for carbon nanotubes [119] and graphene. [2, 3]

8.3.1 *Exfoliation and dispersion of MoS_2*

To begin, dispersions of varying initial concentration (C_I) of MoS_2 powder from 5-200 mg/ml (in 20 mls of solvent) were prepared. The dispersions were probe sonicated for 60 min and then centrifuged at 1500 rpm to remove any unexfoliated material. The supernatants were decanted and their optical absorption spectra were measured (figure 8.2). TEM of these dispersions also indicated that the material was exfoliated and of high quality.

Optical characterisation of the MoS_2 dispersion

The spectra for the MoS_2 dispersions consisted of an excitonic feature at 679 nm and other resonant features at lower wavelengths, superimposed on a power law scattering

background ($\propto \lambda^{-n}$). It was immediately clear that the magnitude of the absorbance varied considerably with C_I. However, because the scattering exponent, n, is thought to depend on flake size, [13, 113] the absolute value of absorbance per cell length (A/l) cannot be used to reliably measure the concentration. To estimate the concentration, the scattering background was extrapolated from the high-wavelength region (dashed line in figure 8.2A) and the value of A/l solely due to resonant absorption, $(A/l)_R$, was estimated for each sample (679 nm, illustrated by arrows in figure 8.2A). The concentration of dispersed material can be determined using $(A/l)_R$, provided the resonant absorption coefficient, α_R , is known. To measure α_R , a known volume of dispersion was filtered through a membrane. By careful weighing, the concentration, C, could be measured and α_R estimated from the measured $(A/l)_R$ [$(A/l)_R = \alpha_R C$] to give α_R = 1020 ml/mg/m. In most cases, this allowed us to determine the concentration of MoS_2 dispersions regardless of the value of the scattering exponent. The measured concentration as a function of C_I is shown in figure 8.2B to increase from $C \approx 0.1$ mg/ml for C_I = 5 mg/ml to $C \approx 2$ mg/ml for C_I = 100 mg/ml before falling off at higher initial concentrations. The initial increase is linear as indicated by the dashed line. The slope of this line gives the yield of the dispersion procedure which was 2.4 % under these circumstances.

8.3.2 *Dispersion optimisation*

Increasing the concentration of dispersed MoS_2 nanosheets

It has been discussed in chapter 5&7, that prolonged sonication results in increased dispersion concentrations. [3, 7] To test if this applies to MoS_2, 100 mls of NMP was added to 10 g of MoS_2 (C_I = 100 mg/ml) in a beaker and probe sonicated for up to ~200 hrs. At various time intervals aliquots were removed, centrifuged (1500 rpm, 45 min), decanted and the absorption spectrum recorded (figure 8.3 left side). The scattering exponent varied from n = 2.7 to n = 4.2 as the sonication time increased suggesting a variation in flake size. [113] The concentration was determined from the spectra as before and is plotted as a function of sonication time in figure 8.3 right

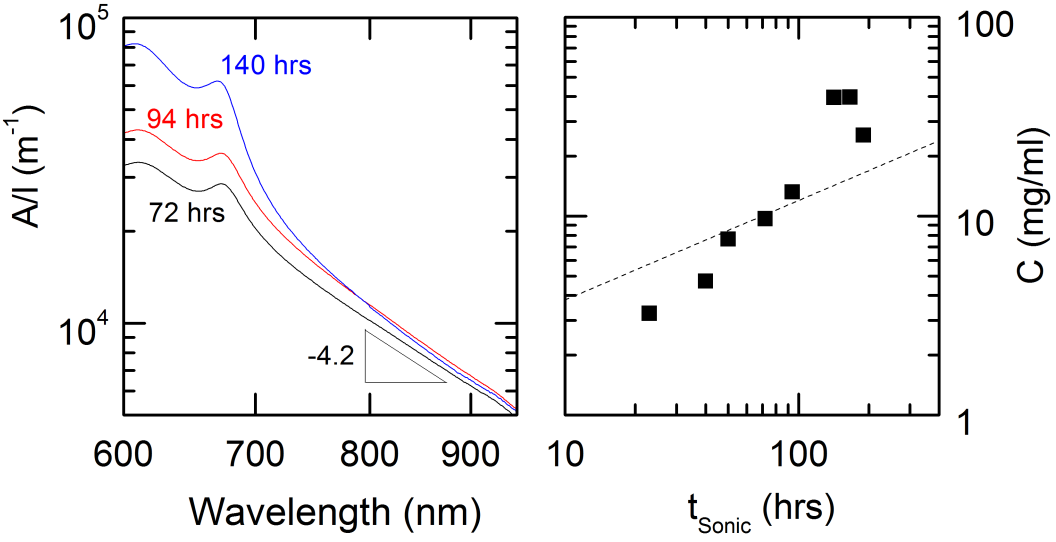

Figure 8.3: Absorbance spectra for various sonication times. Note that the background appears to vary with sonication time. Dispersed concentration as a function of sonication time. The dashed line illustrates $\sqrt{t_{sonic}}$ behaviour.

side. The concentration increased from 3.2 mg/ml after 23 hours sonication to 40 mg/ml after 140 hours before falling off slightly. These concentrations are extremely high and compare favourable to the highest concentration graphene dispersions. [175] Of note, the highest concentration achieved implied a yield of 40% demonstrating the efficiency of this dispersion process. However, unlike the situation for graphene, [3, 7] the concentration of the dispersion did not scale well with the square root of sonication time (illustrated by the dotted line in figure 8.3 right side), suggesting that the exfoliation kinetics may vary between layered materials.

TEM of MoS_2 dispersion to determine quality and nanosheet dimension

The ability to produce such highly concentrated MoS_2 dispersions will be useful provided the flake quality is preserved. To test this, a subset of dispersions was examined using transmission electron microscopy (TEM). Generally, the flakes appeared well exfoliated (figure 8.4A&B) with some very thin sheets, perhaps even monolayers observed (figure 8.4C). Further examination of the flake quality was performed by high resolution TEM imaging (figure 8.4D&E). These images illustrated that prolonged sonication did not appear to damage or disrupt the hexagonal structure of MoS_2.

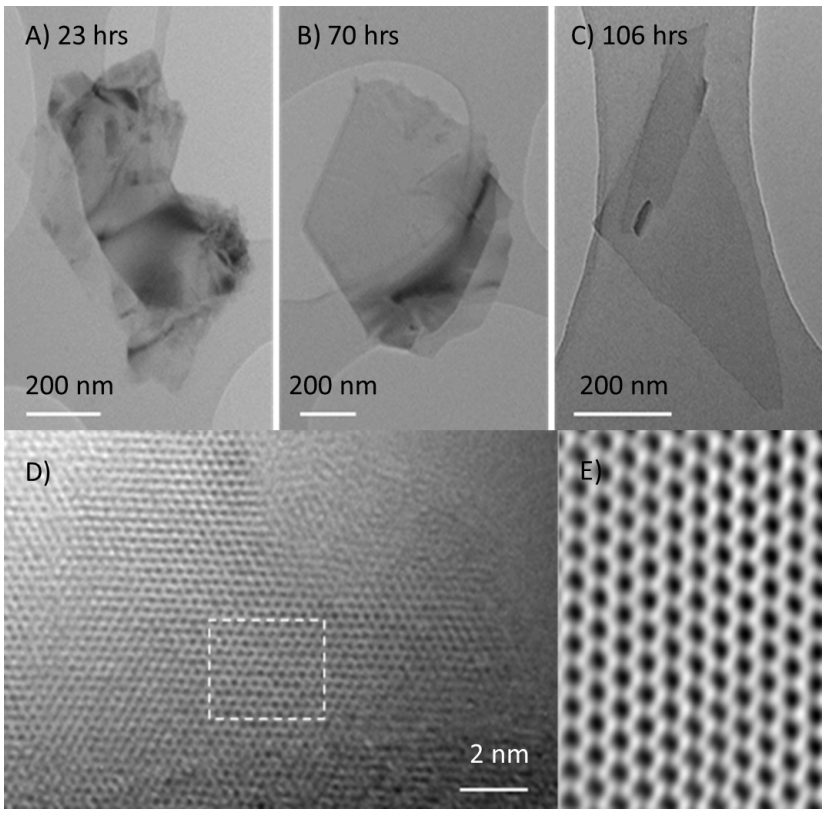

Figure 8.4: A), B) and C) sample images of MoS_2 flakes prepared with sonication times of 23, 70 and 106 hrs respectively. D) A HRTEM image of an MoS_2 flake. Note the well-defined hexagons in the dashed box. E) A digitally filtered image of a portion of the flake within the dashed box.

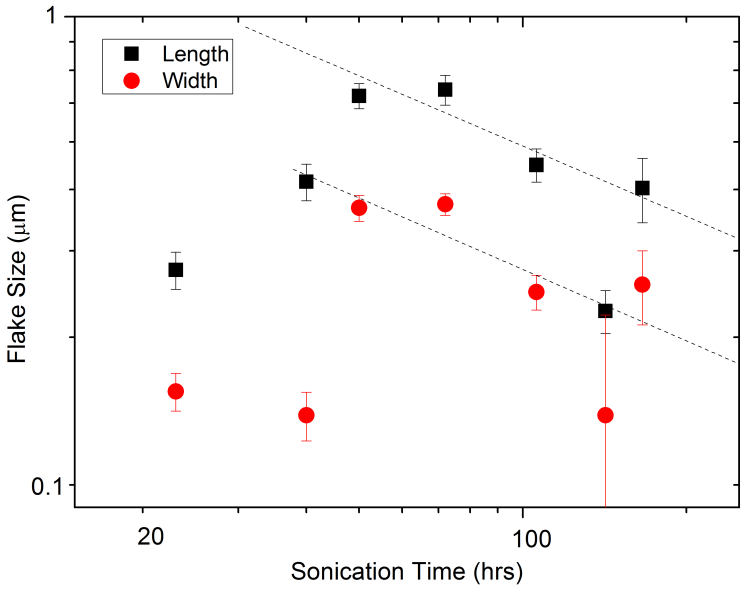

Figure 8.5: Mean flake length and width (calculated from 50 measurements) as a function of sonication time. The dashed lines represent $1/\sqrt{t_{sonic}}$ behaviour.

Unlike graphene, [3] the level of exfoliation of MoS_2 is not easily quantified by edge counting. Further analysis of TEM intensity profiles, coupled with electron diffraction data and electron energy loss spectroscopy can indicate whether the MoS_2 is exfoliated, however a quantitative method to indicate the exact number of layers is still required. [13] Statistical analysis of the lateral flake dimensions (i.e. length, L and width, w) was performed. Shown in figure 8.5 are the mean values of L and w plotted versus sonication time. Both dimensions increase from relatively low values [$< L > \approx 0.3$ μm, $< w > \approx 0.17$ μm] after 23 hrs sonication, to a maximum [$< L > \approx 0.7$ μm, $< w > \approx 0.4$ μm] after 60 hrs sonication. This increase in size after sonication is very interesting and unintuitive and may reflect the preferential exfoliation of MoS_2 crystallites by size. However, after 60 hrs, the flake dimensions decrease to $< L > \approx 0.2$ μm and $< w > \approx 0.15$ μm after 142 hrs of sonication. In the second regime the data is consistent with an inverse square root dependence with sonication time (i.e. $\propto t^{-1/2}$, dashed line). This suggests the flakes are cut by sonication induced scission [151] as observed previously for graphene dispersions in chapter 5&7. [3]

Although these MoS_2 flakes are laterally larger than previously reported [~0.7 μm compared to ~0.3 μm reported by Coleman et. al. and Smith et. al.], [13, 113]

they are still smaller than the graphene flakes obtained using similar sonication and centrifugation (CF) regimes. [3, 80] This may be due to two things, firstly the size of crystallites in the initial starting MoS_2 powder [~10 μm], is much smaller than that of the graphite used in earlier studies [~700 μm]. [2] However, perhaps more likely, sonication induced scission should give a flake size which is determined by the material tensile strength. [133] Lucas has suggested that for rods cut by sonication induced scission, the terminal length, L_t , scales with strength, σ_B , as $L_t \propto \sqrt{\sigma_B}$. [133] While we cannot be sure the flakes described in figure 8.5 have reached their terminal size, we nevertheless compare their length after the longest sonication time (440 nm after 166 hours) to graphene flakes sonicated in NMP which appear to have reached terminal length (~800 nm after 350 hours). [3] Taking the known strengths of graphene and MoS_2 (130 and 23 GPa, $\sqrt{130/23}$= 2.4) [34, 112], we and applying Lucas's expression predicts $L_{t,G}/L_{t,MoS_2} \geq 800/440 = 1.8$ (the inequality is because the MoS_2 flakes have probably not reached their terminal length). This is reasonably close to our estimate from the experimental data. This good agreement suggests the relative flake sizes observed for graphene and MoS_2 are consistent with sonication induced scission.

8.3.3 *Flake size separation by controlled centrifugation*

In chapter 6, it was shown that graphene flakes can be selected by size by controlled centrifugation coupled with sediment recycling. [6, 126] To test if this could be extended to MoS_2 dispersions, an MoS_2/NMP dispersion which had been sonicated for 50 hrs followed by centrifugation at 1500 rpm, was selected. This was chosen based on its relatively high concentration (7.6 mg/ml) and relatively large flakes [$< L > \approx 0.7$ μm]. Similar to graphene controlled centrifugation and size separation demonstrated in chapter 6, the flakes in the stock dispersion were separated by centrifuging at the high rate of 5000 rpm for 45 min (centrifugation time remained constant throughout this study). This acted to separate the smaller flakes which remained in the supernatant from the medium and larger flakes in the sediment. [6] After centrifugation, 8 mls of supernatant was decanted and stored for further analysis, after which 8 mls of

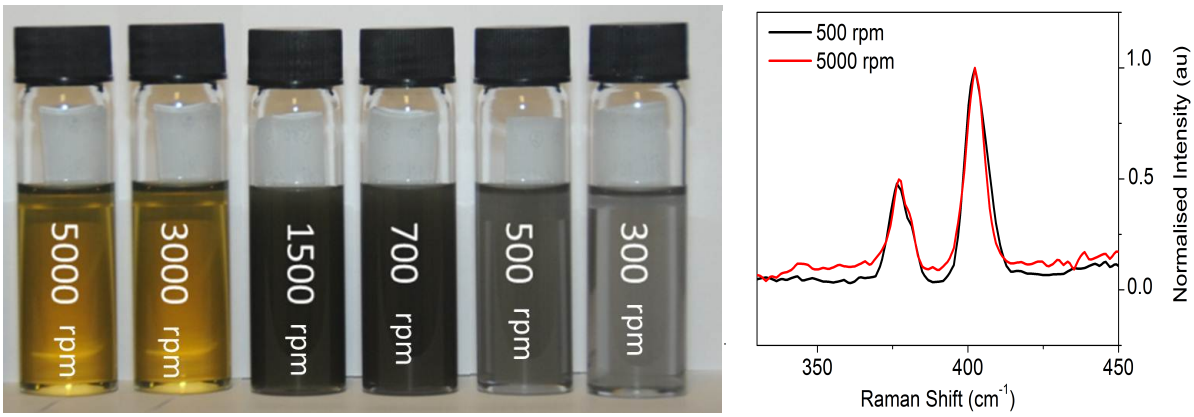

Figure 8.6: Photograph of the dispersions after size selection (these dispersions have been diluted by a factor of 100 to emphasis the colour change). Also shown are typical Raman spectra observed for MoS_2 films, one prepared by vacuum filtration of the the 500 rpm dispersion and the other of the 5000 rpm dispersion. Note there is no difference in the spectra.

fresh NMP were added to the sediment in the same vial. The mixture was stirred and sonicated for 15 min before re centrifuging it at the lower rate of 3000 rpm again separating flakes by size. The supernatant was decanted and fresh NMP was once again added to the sediment. This procedure was repeated another 4 times for 1500, 750, 500 and 300 rpm. By analogy with research discussed in chapter 6, the flake size was expected to increase as the final centrifugation rate decreases. [6] The colour of the resultant dispersions varied strongly with final centrifugation rate indicating that the nature of the nanosheets had indeed changed (figure 8.6).

After each centrifugation step absorption spectroscopy was performed. For high centrifugation rates the spectra were superimposed on a scattering background similar to that observed previously (figure 8.2). However for lower rotation rates the spectra changed significantly, appearing flatter and more featureless as the rotation rate fell (figure 8.7). This may be partly due to dependence of the scattering exponent on flake dimension. To test this, an estimation of the scattering exponent from the high wavelength region, was plotted as a function of centrifugation rate in figure 8.7 inset. The scattering exponent was close to 4 for high rotation rates. This is what might be expected for Rayleigh scattering which would be consistent with the retention of small flakes at high centrifugation rates. [6] In addition, the scattering exponent decreased

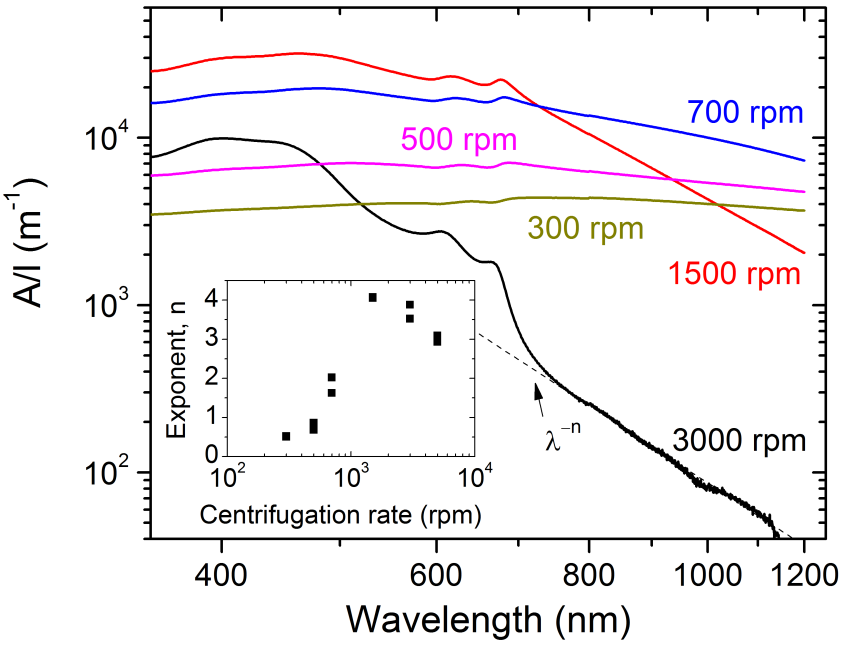

Figure 8.7: Absorption spectra for the dispersions in figure 8.6. The spectra are labelled by their final centrifugation rate. Note how the exponent of the scattering background changes with final centrifugation rate (inset)

with decreasing rotation rate, that is, with increasing flake size. However, this does not entirely describe the spectral changes; as at lower rotation rates the absorption spectra appeared distorted such that background subtraction was impossible. This means that optical measurements of concentration was no longer possible after the controlled CF of the dispersions. The reasons for these distortions are unknown.

TEM on each supernatant to determine the quality and dimension of the flakes during the controlled centrifugation regime (figure 8.8) was also performed. The TEM micrographs illustrated that the MoS_2 was well exfoliated for high rotation rates, however as the rotation rate decreased the electron transparency of the flakes also reduced indicating an increase in flake thickness. In addition, it was noticed that size-selected flakes tended to have smaller flakes adsorbed in many cases.

The lateral size of the flakes could also readily be determined from these images as plotted in figure 8.9. The maximum and minimum flake dimensions normally achieved for the starting dispersions were also indicated by the horizontal lines. After the initial 5000 rpm centrifugation the flakes had a mean length and width of $< L > \approx 0.3 \pm 0.05$ μm and $< w > \approx 0.15 \pm 0.02$ μm. However as the final rotation rate decreased, the

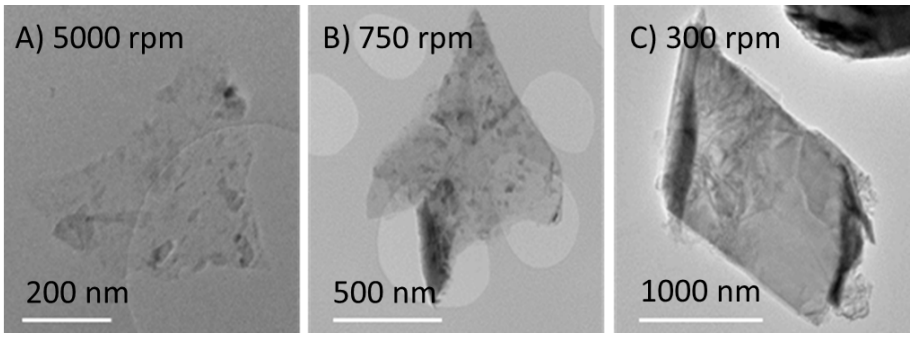

Figure 8.8: A), B) and C) Sample images of flakes after size selection for different final centrifugation rates.

flake dimensions increased, reaching $< L > \approx 2 \pm 0.3$ μm and $< w > \approx 1.2 \pm 0.2\mu$m for the 300 rpm sample. The lengths of the largest flakes observed after each CF was also plotted, and reached ~5 μm for the 500 rpm sample. Once the flake dimensions were known the scattering exponent was plotted as a function of flake length (figure 8.9, inset). Flakes with lengths below 1 μm have exponents between 3 and 4, while longer flakes have lower exponents. This is consistent with the earlier prediction that the scattering component is changing due to changing flake dimension.

8.3.4 *Dispersion sedimentation*

The dispersion stability was also measured by the absorbance and hence concentration as a function of sedimentation time. Data was collected over a 3 week period (figure 8.10). The results indicated that small flakes, found in the 3000 rpm dispersion remained dispersed over the entire measurement period. In contrast, for the 1500 and 300 rpm samples, the concentration fell off steadily with time. As already discussed in chapter 3, modelling the sedimentation as an exponential decay of concentration with time [126] gave the sedimentation time constant, τ, and the percentage of stably dispersed material for each sample. The fit curves predicted that ~45 % and ~22 % are stable indefinitely and gave values of τ of 190 hrs and 33 hrs, for the 1500 and 300 rpm samples respectively.

Taken together, this suggests that sedimentation occurs at a rate defined by the nanosheet size, until a stable concentration is reached. This stable concentration

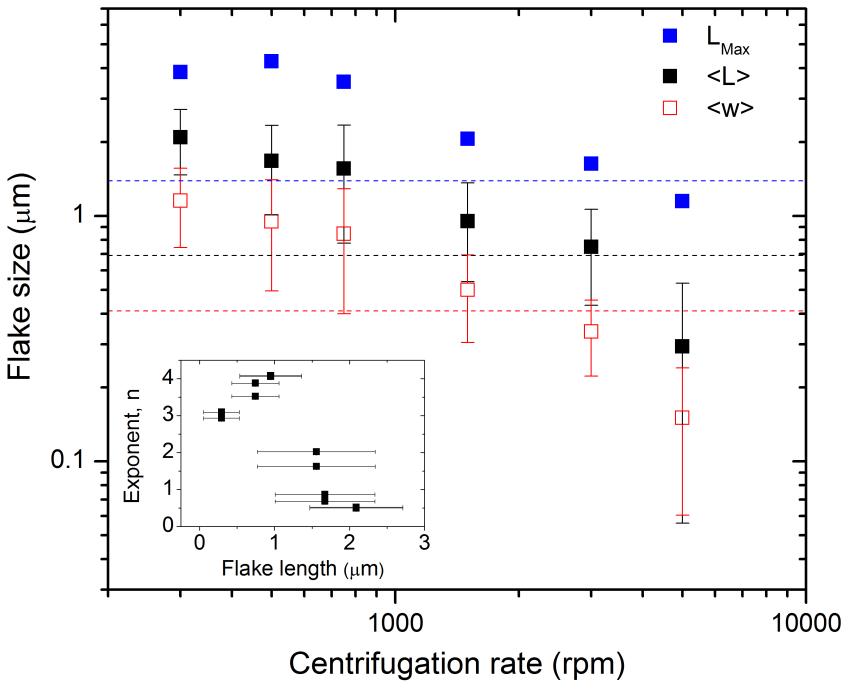

Figure 8.9: Flake size as a function of final centrifugation rate. The data points are the average of 50 measurements. Shown is data for the mean flake length and width as well as the maximum flake length observed. The dashed lines represent the sizes of the flakes in the normal starting dispersion, which has been sonicated for 50 hr and centrifuged at 1500 rpm for 45 min. Inset: Scattering exponent as a function of mean flake length.

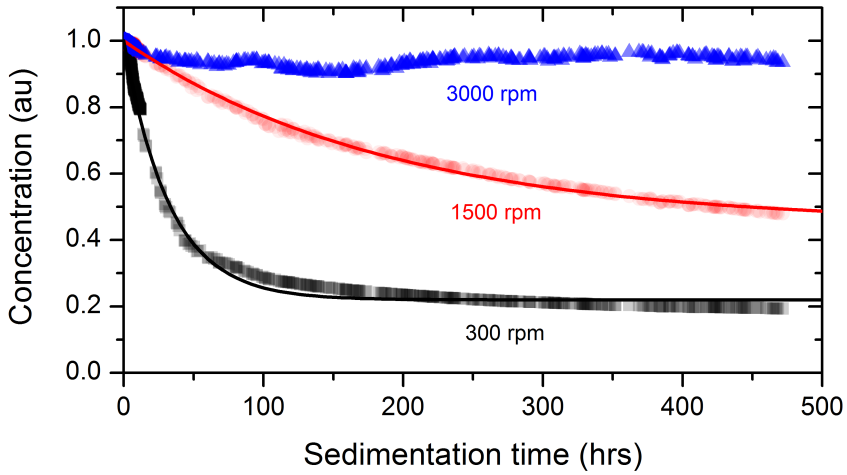

Figure 8.10: Concentration as a function of sedimentation time for size selected flakes of three different final centrifugation rates (see labels). Inset: Sedimentation time constant versus $\langle L \rangle^{-2}$, where L is the mean flake length at the start of the sedimentation experiment.

appears to be size dependent such that higher concentrations are attainable for smaller flakes. This might explain the thickening of the observed flakes as their size increased. Shown in figure 8.11A is a widefield image of a sample of the largest flakes attained (300 rpm). It is clear that most of the flakes are relatively thick. While thinner flakes were observed (figure 8.11 inset), they only represent 10-15 % of the total population.

8.3.5 *Optimisation of flake separation regime*

It was confirmed that the controlled centrifugation regime successfully isolates MoS_2 flakes of different dimensions; however the process is complex and can take up to 6 hrs of centrifugation. In order to reduce the number of centrifugation steps, the same stock dispersion described above was taken (sonicated for 50 hrs) and centrifuged at the low rotation rate of 500 rpm, with the aim of separating the larger flakes into the sediment while leaving the smaller flakes in the supernatant. The supernatant was decanted and fresh NMP was added to the sediment. The mixture was stirred and sonicated for 15 min before centrifuging it again at 300 rpm to remove any remaining large aggregates. The process was similar to before but with four fewer centrifugation steps, thus greatly

reducing the experimental time. TEM imaging of the dispersions gave the flake size for this truncated size selection procedure to be $< L > \approx 1.9$ μm and $< L > \approx 1.2$ μm which is virtually identical to the results for the 300 rpm sample prepared by the longer procedure. A TEM image of the flakes produced by this shortened procedure is shown in figure 8.11B. The flakes look very similar to the ones shown in figure 8.11A. As before, most flakes are relatively thick with a small population (10-15 %) relatively thin (inset).

It may be possible to explain the correlation between flake size and thickness as follows. At high concentrations, large flakes will have a relatively small solvent volume per flake. This may drive aggregation until the volume of solvent per flake increases to an appropriate level. It can be noted that a similar phenomenon has been observed for carbon nanotubes dispersed in solvents where the aggregation state (manifested by the bundle diameter) varied reversibly as the concentration was cycled from high to low. [152, 176]

For such a system, it has been shown in chapter 5, that there is a relationship between the dispersed concentration, C, and mean flake dimensions for exfoliated graphene: $C \propto < w >< t > / < L >^2$ (length, L, width, w, and thickness, t). [3] This implies that large flakes, dispersed at relatively high concentration, as is the case here, should be relatively thick. This suggests that thinner flakes might be obtained by reducing the concentration. To test this, the 300 rpm sample described above was diluted by a factor of 100 by addition of NMP followed by 30 min of probe sonication. TEM analysis (figure 8.11C) suggested the flakes to be marginally thinner (higher electron transparency). However, they were also slightly smaller ($< L > \approx 1.6$ μm and $< w > \approx 0.9$ μm), probably as a result of the additional sonication. Thus, it is not clear if dilution results in a net improvement.

However, it is worth noting that a modest increase in flake thickness may not actually be too high a price to pay for large flakes. The effect of aggregation on the electronic properties of MoS_2 is considerably different to the situation for graphene. In graphene, the electronic properties depend sensitively on the number of layers per flake (for flakes with < 5 layers). [177] However, for MoS_2 the effect is considerably less significant. It is true that a large change occurs going form a monolayer to bilayer. However as the

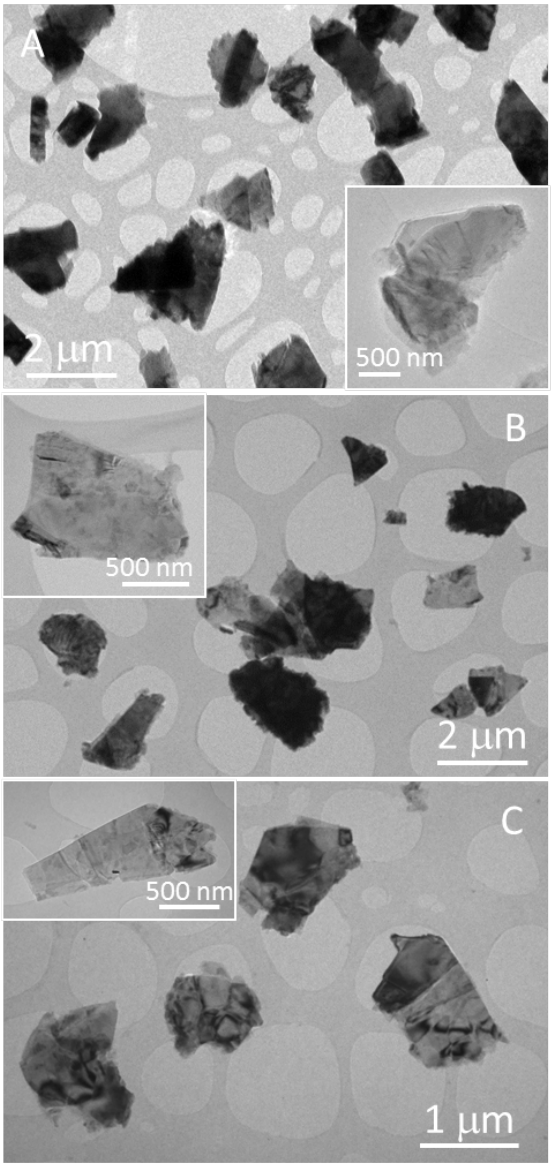

Figure 8.11: TEM micrographs of size selected dispersions produced by centrifugation at 300 rpm as part of A) the normal regime, B) the reduced centrifugation regime and C) the reduced centrifugation regime followed by a 100 fold dilution in NMP. The insets show examples of thinner flakes observed in each case.

number of layers is increased beyond 2 the properties change slowly; going from two to six layers, the bandgap changes from 1.6 to 1.4 eV. [38] Increasing to bulk changes the bandgap only to 1.3 eV. [38] In all cases multilayers have an indirect bandgap. This means the electronic properties of MoS_2 multilayers are relatively insensitive to nanosheet thickness. It is unlikely that the thickness increases observed during size selection procedure result in changes in the bandgap of more than 0.1 - 0.2 eV.

8.4 CONCLUSIONS

In conclusion, the effect of processing parameters on the dispersion and exfoliation of MoS_2 in the solvent NMP was explored. It was found that the dispersed concentration is maximised for an initial MoS_2 concentration of 100 mg/ml. The dispersed concentration can be increased to ~40 mg/ml by increasing the sonication time to 200 hrs. However, the lateral flake size peaks at $\approx$ 700 nm after 60 hrs, after which it falls off due to sonication induced scission. These dispersions generally contain relatively broad flake size distributions. Such dispersions can be separated in fractions with different mean size by controlled centrifugation. Using this technique, it was possible to prepare samples with mean flake length of ~2 μm and maximum length of 4-5 μm. However, larger flakes tend to be thicker than smaller ones, a factor that can be mitigated slightly by dilution and sonication.

9

CONCLUSIONS AND FUTURE WORK

CONCLUSIONS

There is little doubt that two dimensional materials and their unrivaled properties will play an important role in the next generation microprocessors, energy storage capabilities and ultra strong and light composites, to mention a few examples. The research presented in this thesis aims to explore and optimise the preparation of these 2D crystals in the liquid phase. The research began by addressing the need for increased concentrations of graphene in dispersion. In chapter 5 a method was demonstrated to prepare dispersions of graphene in NMP at concentrations of up to 1.2 mg/ml by extended sonication. It was found that the flake dimensions decreased with sonication time as $\frac{1}{\sqrt{t}}$, and that the concentration was directly related to the flake size. Raman spectroscopy indicated that an increased D band was attributed to new edges forming rather than defect formation. Vacuum filtration of these concentrated dispersions demonstrated for the first time that free standing pristine graphene networks can be prepared.

Although high concentrations of graphene dispersions were prepared, their lateral dimensions were too small (<1 μm) for many applications. For example, it was shown for graphene, that the required flake length to reinforce a composite was a few microns or greater. [4, 5] The aim of chapter 6 was to address this, by increasing the lateral dimension of the graphene flakes by a controlled centrifugation process. It was found that centrifugation at high rates resulted in a dispersion of small flakes, while the larger flakes and graphite crystallites sedimented out. Re-dispersion of this sediment in fresh solvent aimed to isolate these larger flakes of different sizes. Successive centrifugations at lower rates then resulted in dispersions of larger flakes. Repeating the procedure a number of times resulted in the separation of the original dispersion into a number

of fractions, each with different mean flake lengths, in this case from ~1 to ~3.5 μm. These flakes were laterally the largest ever demonstrated for liquid phase exfoliation.

Next in chapter 7, dispersions of graphene in low boiling point solvents like chloroform and isopropanol, were optimised. At moderate centrifugation rates, concentrations as high as 0.5 mg/ml of graphene in isopropanol and 0.4 mg/ml in chloroform were achieved. These dispersions were reasonably stable with >80% of the dispersed phase remaining after 100 hrs. Similar to what was observed in chapter 5, the dispersed concentration increased with the square root of sonication time. This behaviour was indicative of sonication induced scission and suggested once again that the concentration was controlled by the flake size. The exfoliation state of the graphene flakes was also good with isopropanol dispersions displaying only flakes with less than 5 layers. Raman measurements showed that the flakes were relatively free of basal plane defects. The versatility of this approach was demonstrated by spray casting the graphene flakes onto an SiO_2 substrate. While some aggregation was observed, the deposited flakes tended to be more numerous and thinner than for flakes deposited with high boiling point solvents.

Graphene liquid phase exfoliation research was extended to its inorganic analogue MoS_2, and others, for the first time in 2011. [13] That research proved the universality of the liquid phase exfoliation approach for layered materials, however further dispersion optimisation was required to improve the yield and size of the 2D nanosheets. In chapter 8, the effects of processing parameters on the dispersion and exfoliation of MoS_2 in the solvent NMP were explored. It was found that the dispersed concentration was maximised for an initial MoS_2 concentration of 100 mg/ml. Similar to graphene dispersions in chapter 5 and 7, prolonged sonication resulted in highly concentrated dispersions up to ~40 mg/ml of MoS_2. However, it was found that the lateral flake size peaked at $\approx$ 700 nm after 60 hrs, attributed to sonication induced scission. These dispersions generally contained relatively broad flake size distributions. As with graphene and demonstrated in chapter 6, 2D material dispersions can be separated into fractions with different mean sizes, by controlled centrifugation. Using this technique, it was possible to prepare samples with mean flake length of ~2 μm and maximum

lengths of 4-5 μm. However, larger flakes tended to be thicker than smaller ones, a factor that was mitigated slightly by dilution and sonication.

The research presented here has succeeded in exploring the preparation parameters for optimising liquid phase exfoliation of graphene and MoS_2 in solvents. It is believed that all knowledge gained throughout this research can be extended to a range of other layered crystals. [124]

FUTURE WORK

The research presented in this thesis addresses two of the three main shortcomings of liquid phase processing of graphene and MoS_2. These are increased concentrations and increased lateral flake sizes, as discussed in chapter 5, 6 & 8. However, further research is required to address the third shortcoming, to increase the overall monolayer population. Ideally, this would be achieved for large nanosheets, without any compromise of their increased dimension.

This may be addressed by further centrifugation of the size separated dispersion in a density gradient medium like iodixanol. If a size selected dispersion with a mean flake length of 2 μm, is centrifuged in a density gradient medium, the majority of flakes within the dispersion should separate by number of layers, as the density should increase with each layer. Also, further optimisation of the dilution with new avenues for agitation rather than sonication may result in flake thinning. There may also be an optimum frequency, dilution, energy density and time at which some extra mild agitation, post centrifugation, will incur flake thinning. This can be tested with a variable frequency sonic bath or perhaps by agitation with a magnetic stirrer which may induce shear stresses on the flakes, thus aiding exfoliation without inducing sonication induced scission. Thorough TEM analysis of the flakes in both cases will be required to quantitatively verify if either results in a nanosheet thickness separation.

Also as already discussed liquid phase exfoliation is a universal technique that can be applied to a wealth of layered materials, as demonstrated by exfolition of graphene from graphite and 2D nanosheets of MoS_2. The next extension of this research will be

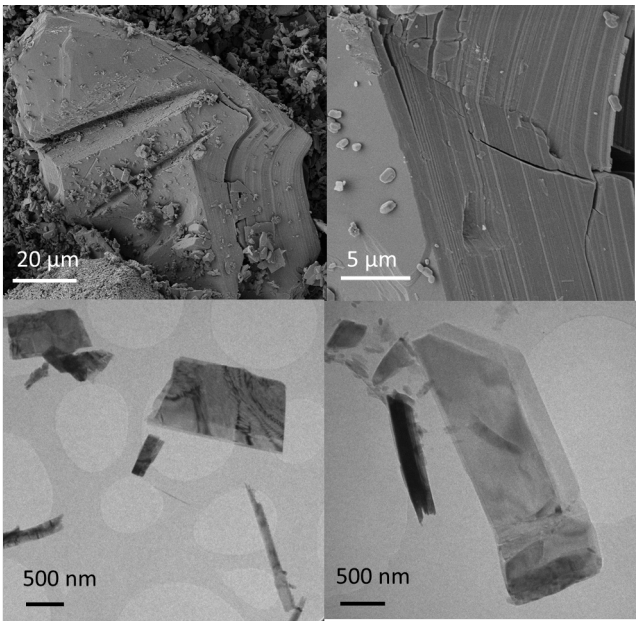

Figure 9.1: Top: SEM image of α-MoO_3 bulk crystal with a zoom in at the edge on the right. Bottom: Are TEM images of exfoliated MoO_3 nanosheets, dispersed in IPA.

applying all gained knowledge to transition metal oxides, TMOs. TMOs comprise of a transition metal sandwiched between oxygen atoms. There are dozens of different oxide nanosheets. By using the liquid phase exfoliation approach, it will be possible to investigate dozens of different 2D oxide nanosheets in search of new phenomena and applications. Oxide nanosheets are structurally diverse and have interesting electronic properties. They have potential applications in a range of areas such as gas sensing, [178, 179] electrochromics devices, [180, 181] molecular electronics [94] and lithium ion batteries [182]. Taking molybdenum trioxide, MoO_3 as the model TMO structure, a full liquid phase exfoliation study will be performed. α-MoO_3 is an orthorhombic layered material and was purchased from Sigma Aldrich (CAS: 1313275). The layered structure can been seen in the SEM images in figure 9.1. To begin, suitable dispersing solvents will be selected based on the materials Hildebrand solubility parameters. Next, the level of exfoliation will be rigorously tested by monitoring the dispersion quality, concentration, flake dimension and thickness as a function of sonication time. Some exfolaited nanosheets are also shown in the bottom of figure 9.1. These samples were prepared by sonicating 5 mg/ml of MoO_3 in IPA, for 1 hr in the point probe sonic tip at 25 % amplitude. These preliminary results look very promising.

BIBLIOGRAPHY

[1] Novoselov, K., Geim, A., Morozov, S., Jiang, D., Zhang, Y., Dubonos, S., Grigorieva, I., and Firsov, A. (2004) Electric field effect in atomically thin carbon films. *Science 306*, 666–669.

[2] Hernandez, Y. et al. (2008) High yield production of graphene by liquid-phase exfoliation of graphite. *Nature Nanotechnology 3*, 563–568.

[3] Khan, U., O'Neill, A., Lotya, M., De, S., and Coleman, J. N. (2010) High-Concentration Solvent Exfoliation of Graphene. *Small 6*, 864–871.

[4] Gong, L., Kinloch, I. A., Young, R. J., Riaz, I., Jalil, R., and Novoselov, K. S. (2010) Interfacial Stress Transfer in a Graphene Monolayer Nanocomposite. *Advanced Materials 22*, 2694.

[5] May, P., Khan, U., O'Neill, A., and Coleman, J. (2012) Approaching the theoretical limit for reinforcing polymers with graphene. *Journal of Materials Chemistry 22*, 1278–1282.

[6] Khan, U., O'Neill, A., Porwal, H., May, P., Nawaz, K., and Coleman, J. N. (2012) Size selection of dispersed, exfoliated graphene flakes by controlled centrifugation. *Carbon 50*, 470–475.

[7] O'Neill, A., Khan, U., Nirmalraj, P. N., Boland, J., and Coleman, J. N. (2011) Graphene Dispersion and Exfoliation in Low Boiling Point Solvents. *The Journal of Physical Chemistry C 115*, 5422–5428.

[8] O'Neill, A., Khan, U., and Coleman, J. N. (2012) Preparation of High Concentration Dispersions of Exfoliated MoS2 with Increased Flake Size. *Chemistry of Materials 24*, 2414–2421.

[9] Novoselov, K., Fal, V., Colombo, L., Gellert, P., Schwab, M., and Kim, K. (2012) A raodmap for graphene. *Nature 490*, 192–200.

[10] Binnig, G., and Rohrer, H. (1986) Scanning tunneling microscopy. *IBM Journal of Research and Development 30*, 355–369.

[11] Kroto, H. W., Heath, J. R., O'Brien, S. C., Curl, R. F., and Smalley, R. E. (1985) C60: Buckminsterfullerene. *Nature 318*, 162–163.

[12] Iijima, S. (1991) Helical microtubules of graphitic carbon. *Nature 354*, 56–58.

[13] Coleman, J. N. et al. (2011) Two Dimensional Nanosheets Produced by Liquid Exfoliation of Layered Materials. *Science 331*, 568–571.

[14] Peierls, R. (1935) Quelques proprietes typiques des corps solides. *Ann. Inst. Henri Poincare 5*, 117–222.

[15] Landau, L. (1937) Zur theorie der phasenumwandlungen II. Phys. *Z. Sowjetunion 11*, 26–35.

[16] Venables, J. A., Spiller, G. D. T., and Hanbucken, M. (1984) Nucleation and growth of thin films. *Reports on Progress in Physics 47*, 399.

[17] Zinkeallmang, M., Feldman, L. C., and Grabow, M. H. (1992) Clustering on surfaces. *Surface Science Reports 16*, 377–463.

[18] Mermin, N. D. (1979) Crystalline order in two dimensions. *Phys Rev B 20*, 4762.

[19] Meyer, J. C., Geim, A., Katsnelson, M. I., Novoselov, K. S., Booth, T. J., and Roth, S. (2007) The structure of suspended graphene sheets. *Nature 446*, 60–63.

[20] Brivio, J., Alexander, D. T. L., and Kis, A. (2011) Ripples and Layers in Ultrathin MoS2 Membranes. *Nano Letters 11*, 5148–5153.

[21] Katsnelson, M. (2007) Graphene: carbon in two dimensions. *Materials today 10*, 20–27.

[22] Wilson, M. (2006) Electrons in atomically thin carbon sheets behave like massless particles. *Physics Today 59*, 21.

[23] Novoselov, K., Morozov, S., Mohinddin, T., Ponomarenko, L., Elias, D., Yang, R., Barbolina, I., Blake, P., Booth, T., and Jiang, D. (2007) Electronic properties of graphene. *Basic Solid State Physics 244*, 4106–4111.

[24] Tan, Y., Zhang, Y., Bolotin, K., Zhao, Y., Adam, S., Hwang, E., Das Sarma, S., Stormer, H., and Kim, P. (2007) Measurement of scattering rate and minimum conductivity in graphene. *Physical review letters 99*, 246803.

[25] Fal'ko, V. I., and Geim, A. K. (2007) Graphene: Emerging matter in two dimensions. *European Physical Journal-Special Topics 148*, 1–3.

[26] Geim, A. K., and MacDonald, A. H. (2007) Graphene: Exploring Carbon Flatland. *Physics Today 60*, 35–41.

[27] Geim, A., and Kim, P. (2008) Carbon wonderland. *Scientific American 298*, 68–75.

[28] Katsnelson, M. I., and Novoselov, K. S. (2007) Graphene: New bridge between condensed matter physics and quantum electrodynamics. *Solid State Communications 143*, 3–13.

[29] Bolotin, K., Sikes, K., Jiang, Z., Klima, M., Fudenberg, G., Hone, J., Kim, P., and Stormer, H. (2008) Ultrahigh electron mobility in suspended graphene. *Solid State Communications 146*, 351–355.

[30] Geim, A. K., and Novoselov, K. S. (2007) The rise of graphene. *Nature Materials 6*, 183–191.

[31] Novoselov, K. S., Geim, A. K., Morozov, S. V., Jiang, D., Katsnelson, M. I., Grigorieva, I. V., Dubonos, S. V., and Firsov, A. A. (2005) Two-dimensional gas of massless Dirac fermions in graphene. *Nature 438*, 197–200.

[32] Zhang, Y., Tan, Y.-W., Stormer, H. L., and Kim, P. (2005) Experimental observation of the quantum Hall effect and Berry's phase in graphene. *Nature 438*, 201–204.

[33] Partoens, B., and Peeters, F. (2006) From graphene to graphite: Electronic structure around the K point. *Physical Review B 74*, 75404.

[34] Lee, C., Wei, X., Kysar, J., and Hone, J. (2008) Measurement of the elastic properties and intrinsic strength of monolayer graphene. *Science 321*, 385–388.

[35] Booth, T. J., Blake, P., Nair, R. R., Jiang, D., Hill, E. W., Bangert, U., Bleloch, A., Gass, M., Novoselov, K. S., Katsnelson, M. I., and Geim, A. K. (2008) Macroscopic Graphene Membranes and Their Extraordinary Stiffness. *Nano Letters 8*, 2442–2446.

[36] Balandin, A., Ghosh, S., Bao, W., Calizo, I., Teweldebrhan, D., Miao, F., and Lau, C. (2008) Superior thermal conductivity of single-layer graphene. *Nano Letters 8*, 902–907.

[37] Nair, R., Blake, P., Grigorenko, A., Novoselov, K., Booth, T., Stauber, T., Peres, N., and Geim, A. (2008) Fine structure constant defines visual transparency of graphene. *Science 320*, 1308.

[38] Mak, K. F., Lee, C., Hone, J., Shan, J., and Heinz, T. F. (2010) Atomically Thin MoS2 A New Direct-Gap Semiconductor. *Physical Review Letters 105*, 4.

[39] Ruoff, R. (2008) Calling all chemists. *Nat Nanotechnol 3*, 10–11.

[40] Novoselov, K. S., Jiang, D., Schedin, F., Booth, T. J., Khotkevich, V. V., Morozov, S. V., and Geim, A. K. (2005) Two-dimensional atomic crystals. *Proceedings of the National Academy of Sciences of the United States of America 102*, 10451–10453.

[41] Moser, J., Verdaguer, A., Jimenez, D., Barreiro, A., and Bachtold, A. (2008) The environment of graphene probed by electrostatic force microscopy. *Applied Physics Letters 92*, 123507.

[42] Allen, M., Tung, V., and Kaner, R. (2010) Honeycomb Carbon: A Review of Graphene. *Chemical Reviews 110*, 132–145.

[43] de Heer, W., Berger, C., Wu, X., First, P., Conrad, E., Li, X., Li, T., Sprinkle, M., Hass, J., and Sadowski, M. (2007) Epitaxial graphene. *Solid State Communications 143*, 92–100.

[44] Novoselov, K. (2007) Graphene: Mind the gap. *Nature materials 6*, 720–721.

[45] Zhou, S. Y., Gweon, G. H., Fedorov, A. V., First, P. N., de Heer, W. A., Lee, D. H., Guinea, F., Castro Neto, A. H., and Lanzara, A. (2007) Substrate-induced bandgap opening in epitaxial graphene. *Nat Mater 6*, 770–775.

[46] Ueta, H., Saida, M., Nakai, C., Yamada, Y., Sasaki, M., and Yamamoto, S. (2004) Highly oriented monolayer graphite formation on Pt (111) by a supersonic methane beam. *Surface Science 560*, 183–190.

[47] Busse, C., Wall, D., Buckanie, N., zu Heringdorf, F., van Gastel, R., Poelsema, B., and Michely, T. (2009) Growth of graphene on Ir (111). *New Journal of Physics 11*, 22.

[48] Sutter, P., Flege, J., and Sutter, E. (2008) Epitaxial graphene on ruthenium. *Nature materials 7*, 406–411.

[49] Li, X., Cai, W., An, J., Kim, S., Nah, J., Yang, D., Piner, R., Velamakanni, A., Jung, I., and Tutuc, E. (2009) Large-area synthesis of high-quality and uniform graphene films on copper foils. *Science 324*, 1312.

[50] Kumar, S., McEvoy, N., Lutz, T., Keeley, G., Nicolosi, V., Murray, C., Blau, W., and Duesberg, G. (2010) Gas phase controlled deposition of high quality large-area graphene films. *Chemical communications 46*, 1422.

[51] Reina, A., Jia, X., Ho, J., Nezich, D., Son, H., Bulovic, V., Dresselhaus, M., and Kong, J. (2008) Large area, few-layer graphene films on arbitrary substrates by chemical vapor deposition. *Nano Letters 9*, 30–35.

[52] Kim, K. S., Zhao, Y., Jang, H., Lee, S. Y., Kim, J. M., Ahn, J. H., Kim, P., Choi, J. Y., and Hong, B. H. (2009) Large-scale pattern growth of graphene films for stretchable transparent electrodes. *Nature 457*, 706–710.

[53] Bae, S., Kim, H., Xu, X., Balakrishnan, J., Lei, T., Song, Y., Kim, Y., Ozyilmaz, B., Ahn, J., and Hong, B. (2010) 30-Inch Roll-Based Production of High-Quality Graphene Films for Flexible Transparent Electrodes. *Nature Nanotechnology 5*, 574–578.

[54] Gutman, I., and Cyvin, S. *Introduction to the theory of benzenoid hydrocarbons*; Springer, 1989.

[55] Clar, E. *The aromatic sextet*; John Wiley & Sons, 1972.

[56] Wu, J., Pisula, W., and Mullen, K. (2007) Graphenes as potential material for electronics. *Chemical Reviews 107*, 718–747.

[57] Simpson, C., Brand, J., Berresheim, A., Przybilla, L., Raeder, H., and Muellen, K. (2002) Synthesis of a giant 222 carbon graphite sheet. *Chemistry -Weinheim-European journal 8*, 1424–1429.

[58] Yang, X., Dou, X., Rouhanipour, A., Zhi, L., Rader, H. J., and Mullen, K. (2008) Two-Dimensional Graphene Nanoribbons. *Journal of the American Chemical Society 130*, 4216–4217.

[59] Hughes, J. M., Hernandez, Y., Aherne, D., Doessel, L., Mullen, K., Moreton, B., White, T. W., Partridge, C., Costantini, G., Shmeliov, A., Shannon, M., Nicolosi, V., and Coleman, J. N. (2012) High Quality Dispersions of Hexabenzocoronene in Organic Solvents. *Journal of the American Chemical Society 134*, 12168–12179.

[60] Niyogi, S., Bekyarova, E., Itkis, M. E., McWilliams, J. L., Hamon, M. A., and Haddon, R. C. (2006) Solution properties of graphite and graphene. *Journal of the American Chemical Society 128*, 7720.

[61] Hummers Jr, W., and Offeman, R. (1958) Preparation of graphitic oxide. *Journal of the American Chemical Society 80*, 1339–1339.

[62] Lotya, M., Hernandez, Y., King, P. J., Smith, R. J., Nicolosi, V., Karlsson, L. S., Blighe, F. M., De, S., Wang, Z., McGovern, I. T., Duesberg, G. S., and Coleman, J. N. (2009) Liquid Phase Production of Graphene by Exfoliation of Graphite in Surfactant/Water Solutions. *Journal of the American Chemical Society 131*, 3611–3620.

[63] He, H., Riedl, T., Lerf, A., and Klinowski, J. (1996) Solid-state NMR studies of the structure of graphite oxide. *Journal of Physical Chemistry 100*, 19954–19958.

[64] Geng, Y., Wang, S., and Kim, J. (2009) Preparation of graphite nanoplatelets and graphene sheets. *Journal of Colloid And Interface Science 336*, 592–598.

[65] Si, Y., and Samulski, E. (2008) Synthesis of water soluble graphene. *Nano Letters 8*, 1679–1682.

[66] Green, A., and Hersam, M. (2010) Emerging Methods for Producing Monodisperse Graphene Dispersions. *The Journal of Physical Chemistry Letters 1*, 544–549.

[67] Tung, V., Allen, M., Yang, Y., and Kaner, R. (2009) High-throughput solution processing of large-scale graphene. *Nature Nanotechnology 4*, 25–29.

[68] Park, S., An, J., Jung, I., Piner, R. D., An, S. J., Li, X., Velamakanni, A., and Ruoff, R. S. (2009) Colloidal Suspensions of Highly Reduced Graphene Oxide in a Wide Variety of Organic Solvents. *Nano Letters 9*, 1593–1597.

[69] Park, S., and Ruoff, R. (2009) Chemical methods for the production of graphenes. *Nature Nanotechnology 4*, 217–224.

[70] Ang, P., Wang, S., Bao, Q., Thong, J., and Loh, K. (2009) High-Throughput Synthesis of Graphene by Intercalation- Exfoliation of Graphite Oxide and Study of Ionic Screening in Graphene Transistor. *ACS Nano 3*, 3587–3594.

[71] Li, D., Muller, M., Gilje, S., Kaner, R., and Wallace, G. (2008) Processable aqueous dispersions of graphene nanosheets. *Nature Nanotechnology 3*, 101–105.

[72] Dikin, D. A., Stankovich, S., Zimney, E. J., Piner, R. D., Dommett, G. H. B., Evmenenko, G., Nguyen, S. T., and Ruoff, R. S. (2007) Preparation and characterization of graphene oxide paper. *Nature 448*, 457–460.

[73] Yu, M.-F., Files, B. S., Arepalli, S., and Ruoff, R. S. (2000) Tensile Loading of Ropes of Single Wall Carbon Nanotubes and their Mechanical Properties. *Physical review letters 84*, 5552.

[74] Stankovich, S., Dikin, D., Piner, R., Kohlhaas, K., Kleinhammes, A., Jia, Y., Wu, Y., Nguyen, S., and Ruoff, R. (2007) Synthesis of graphene-based nanosheets via chemical reduction of exfoliated graphite oxide. *Carbon 45*, 1558–1565.

[75] Stankovich, S., Piner, R., Chen, X., Wu, N., Nguyen, S., and Ruoff, R. (2006) Stable aqueous dispersions of graphitic nanoplatelets via the reduction of exfoliated graphite oxide in the presence of poly (sodium 4-styrenesulfonate). *Journal of Materials Chemistry 16*, 155–158.

[76] Hao, R., Qian, W., Zhang, L., and Hou, Y. (2008) Aqueous dispersions of TCNQ-anion-stabilized graphene sheets. *Chemical Communications 48*, 6576–6578.

[77] Blake, P., Brimicombe, P., Nair, R., Booth, T., Jiang, D., Schedin, F., Ponomarenko, L., Morozov, S., Gleeson, H., and Hill, E. (2008) Graphene-based liquid crystal device. *Nano Letters 8*, 1704–1708.

[78] Bourlinos, A. B., Georgakilas, V., Zboril, R., Steriotis, T. A., and Stubos, A. K. (2009) Liquid-Phase Exfoliation of Graphite Towards Solubilized Graphenes. *Small 5*, 1841–1845.

[79] Nuvoli, D., Valentini, L., Alzari, V., Scognamillo, S., Bon, S., Piccinini, M., Illescas, J., and Mariani, A. (2010) High concentration few-layer graphene sheets obtained by liquid phase exfoliation of graphite in ionic liquid. *J. Mater. Chem. 10*, 3428–3431.

[80] Lotya, M., King, P. J., Khan, U., De, S., and Coleman, J. N. (2010) High-Concentration, Surfactant-Stabilized Graphene Dispersions. *Acs Nano 4*, 3155–3162.

[81] Choi, W., Lahiri, I., Seelaboyina, R., and Kang, Y. S. (2010) Synthesis of Graphene and Its Applications: A Review. *Critical Reviews in Solid State and Materials Sciences 35*, 52 – 71.

[82] Stoller, M., Park, S., Zhu, Y., An, J., and Ruoff, R. (2008) Graphene-based ultracapacitors. *Nano Letters 8*, 3498–3502.

[83] Pumera, M. (2009) Electrochemistry of graphene: new horizons for sensing and energy storage. *The Chemical Record 9*, 211–223.

[84] Mohanty, N., and Berry, V. (2008) Graphene-Based Single-Bacterium Resolution Biodevice and DNA Transistor: Interfacing Graphene Derivatives with Nanoscale and Microscale Biocomponents. *Nano Letters 8*, 4469–4476.

[85] Wang, F., Zhang, Y., Tian, C., Girit, C., Zettl, A., Crommie, M., and Shen, Y. R. (2008) Gate-Variable Optical Transitions in Graphene. *Science 320*, 206–209.

[86] Stankovich, S., Dikin, D. A., Dommett, G. H. B., Kohlhaas, K. M., Zimney, E. J., Stach, E. A., Piner, R. D., Nguyen, S. T., and Ruoff, R. S. (2006) Graphene-based composite materials. *Nature 442*, 282–286.

[87] Watcharotone, S., Dikin, D. A., Stankovich, S., Piner, R., Jung, I., Dommett, G. H. B., Evmenenko, G., Wu, S.-E., Chen, S.-F., Liu, C.-P., Nguyen, S. T., and Ruoff, R. S. (2007) Graphene Silica Composite Thin Films as Transparent Conductors. *Nano Letters 7*, 1888–1892.

[88] Son, Y.-W., Cohen, M. L., and Louie, S. G. (2006) Energy Gaps in Graphene Nanoribbons. *Phys. Rev. Lett. 97*, 216803.

[89] Wilson, J., and Yoffe, A. (1969) The transition metal dichalcogenides discussion and interpretation of the observed optical, electrical and structural properties. *Advances in Physics 18*, 193–335.

[90] Gordon, R. A., Yang, D., Crozier, E. D., Jiang, D. T., and Frindt, R. F. (2002) Structures of exfoliated single layers of WS2, MoS2, and MoSe2 in aqueous suspension. *Physical Review B 65*, 125407.

[91] Splendiani, A., Sun, L., Zhang, Y., Li, T., Kim, J., Chim, C.-Y., Galli, G., and Wang, F. (2010) Emerging Photoluminescence in Monolayer MoS2. *Nano Letters 10*, 1271–1275, PMID: 20229981.

[92] Feldman, J. (1976) Elastic constants of 2H-MoS2 and 2H-NbSe2 extracted from measured dispersion curves and linear compressibilities. *Journal of Physics and Chemistry of Solids 37*, 1141 – 1144.

[93] Castellanos-Gomez, A., Poot, M., Steele, G. A., van der Zant, H. S. J., Agrait, N., and Rubio-Bollinger, G. (2012) Elastic Properties of Freely Suspended MoS2 Nanosheets. *Advanced Materials 24*, 772.

[94] Osada, M., and Sasaki, T. (2009) Exfoliated oxide nanosheets: new solution to nanoelectronics. *Journal of Materials Chemistry 19*, 2503–2511.

[95] Joensen, P., Frindt, R. F., and Morrison, S. R. (1986) Single-layer MoS2. *Materials Research Bulletin 21*, 457–461.

[96] Frindt, R. F. (1966) Single Crystals of MoS2 Several Molecular Layers Thick. *Journal of Applied Physics 37*, 1928–1929.

[97] Mattheiss, L. F. (1973) Band Structures of Transition-Metal-Dichalcogenide Layer Compounds. *Phys. Rev. B 8*, 3719–3740.

[98] Py, M. A., and Haering, R. R. (1983) Structural destabilization induced by lithium intercalation in MoS2 and related compounds. *Canadian Journal of Physics 61*, 76–84.

[99] Yang, D., Sandoval, S. J., Divigalpitiya, W. M. R., Irwin, J. C., and Frindt, R. F. (1991) Structure of single-molecular-layer MoS2. *Physical Review B 43*, 12053.

[100] Eda, G., Yamaguchi, H., Voiry, D., Fujita, T., Chen, M. W., and Chhowalla, M. (2011) Photoluminescence from Chemically Exfoliated MoS(2). *Nano Letters 11*, 5111–5116.

[101] Zeng, Z. Y., Yin, Z. Y., Huang, X., Li, H., He, Q. Y., Lu, G., Boey, F., and Zhang, H. (2011) Single-Layer Semiconducting Nanosheets: High-Yield Preparation and Device Fabrication. *Angewandte Chemie-International Edition 50*, 11093–11097.

[102] Radisavljevic, B., Radenovic, A., Brivio, J., Giacometti, V., and Kis, A. (2011) Single-layer MoS2 transistors. *Nat Nano 6*, 147–150.

[103] Benameur, M. M., Radisavljevic, B., Heron, J. S., Sahoo, S., Berger, H., and Kis, A. (2011) Visibility of dichalcogenide nanolayers. *Nanotechnology 22*, 125706.

[104] Late, D. J., Liu, B., Matte, H. S. S. R., Rao, C. N. R., and Dravid, V. P. (2012) Rapid Characterization of Ultrathin Layers of Chalcogenides on SiO2/Si Substrates. *Advanced Functional Materials 22*, 1894–1905.

[105] Kim, D., Sun, D., Lu, W., Cheng, Z., Zhu, Y., Le, D., Rahman, T. S., and Bartels, L. (2011) Toward the Growth of an Aligned Single-Layer MoS2 Film. *Langmuir 27*, 11650–11653.

[106] Liu, K.-K., Zhang, W., Lee, Y.-H., Lin, Y.-C., Chang, M.-T., Su, C.-Y., Chang, C.-S., Li, H., Shi, Y., Zhang, H., Lai, C.-S., and Li, L.-J. (2012) Growth of Large-Area and Highly Crystalline MoS2 Thin Layers on Insulating Substrates. *Nano Letters 12*, 1538–1544.

[107] Shi, Y., Zhou, W., Lu, A.-Y., Fang, W., Lee, Y.-H., Hsu, A. L., Kim, S. M., Kim, K. K., Yang, H. Y., Li, L.-J., Idrobo, J.-C., and Kong, J. (2012) van der Waals Epitaxy of MoS2 Layers Using Graphene As Growth Templates. *Nano Letters 12*, 2784–2791.

[108] Lee, Y.-H., Zhang, X.-Q., Zhang, W., Chang, M.-T., Lin, C.-T., Chang, K.-D., Yu, Y.-C., Wang, J. T.-W., Chang, C.-S., Li, L.-J., and Lin, T.-W. (2012) Synthesis of Large-Area MoS2 Atomic Layers with Chemical Vapor Deposition. *Advanced Materials 24*, 2320–2325.

[109] Zhan, Y., Liu, Z., Najmaei, S., Ajayan, P. M., and Lou, J. (2012) Large-Area Vapor-Phase Growth and Characterization of MoS2 Atomic Layers on a SiO2 Substrate. *Small 8*, 966–971.

[110] Lebegue, S., and Eriksson, O. (2009) Electronic structure of two-dimensional crystals from ab initio theory. *Phys. Rev. B 79*, 115409.

[111] Yin, Z., Li, H., Li, H., Jiang, L., Shi, Y., Sun, Y., Lu, G., Zhang, Q., Chen, X., and Zhang, H. (2012) Single-Layer MoS2 Phototransistors. *ACS Nano 6*, 74–80.

[112] Bertolazzi, S., Brivio, J., and Kis, A. (2011) Stretching and Breaking of Ultrathin MoS2. *Acs Nano 5*, 9703–9709.

[113] Smith, R. J., King, P. J., Lotya, M., Wirtz, C., Khan, U., De, S., O'Neill, A., Duesberg, G. S., Grunlan, J. C., Moriarty, G., Chen, J., Wang, J. Z., Minett, A. I.,

Nicolosi, V., and Coleman, J. N. (2011) Large-Scale Exfoliation of Inorganic Layered Compounds in Aqueous Surfactant Solutions. *Advanced Materials 23*, 3944.

[114] Du, G., Guo, Z., Wang, S., Zeng, R., Chen, Z., and Liu, H. (2010) Superior stability and high capacity of restacked molybdenum disulfide as anode material for lithium ion batteries. *Chemical Communications 46*, 1106–1108.

[115] Green, A. A., and Hersam, M. C. (2009) Solution Phase Production of Graphene with Controlled Thickness via Density Differentiation. *Nano Letters 9*, 4031–4036.

[116] Smith, R. J., King, P. J., Wirtz, C., Duesberg, G. S., and Coleman, J. N. (2012) Lateral size selection of surfactant-stabilised graphene flakes using size exclusion chromatography. *Chemical Physics Letters 531*, 169 – 172.

[117] Bergin, S., Sun, Z., Rickard, D., Streich, P., Hamilton, J., and Coleman, J. (2009) Multicomponent Solubility Parameters for Single-Walled Carbon Nanotube-Solvent Mixtures. *ACS Nano 3*, 787–792.

[118] Coleman, J. N. (2009) Liquid-Phase Exfoliation of Nanotubes and Graphene. *Advanced Functional Materials 19*, 3680–3695.

[119] Bergin, S. D., Nicolosi, V., Streich, P. V., Giordani, S., Sun, Z., Windle, A. H., Ryan, P., Niraj, N. P. P., Wang, Z.-T. T., Carpenter, L., Blau, W. J., Boland, J. J., Hamilton, J. P., and Coleman, J. N. (2008) Towards Solutions of Single-Walled Carbon Nanotubes in Common Solvents. *Advanced Materials 20*, 1876–1881.

[120] Hernandez, Y., Lotya, M., Rickard, D., Bergin, S. D., and Coleman, J. N. (2010) Measurement of Multicomponent Solubility Parameters for Graphene Facilitates Solvent Discovery. *Langmuir 26*, 3208–3213.

[121] Flory, P. J. *Principles of Polymer Chemistry*; Cornell University Press, 1953.

[122] Hansen, C. *Hansen solubility parameters: a user's handbook*; CRC Press, 2007.

[123] Hughes, J. M., Aherne, D., Bergin, S. D., O'Neill, A., Streich, P. V., Hamilton, J. P., and Coleman, J. N. (2012) Using solution thermodynamics to describe the dis-

persion of rod-like solutes: application to dispersions of carbon nanotubes in organic solvents. *Nanotechnology 23*, 265604–265612.

[124] Cunningham, G., Lotya, M., Cucinotta, C., Sanvito, S., Bergin, S., Menzel, R., Shaffer, M., and Coleman, J. (2012) Solvent Exfoliation of Transition Metal Dichalcogenides Dispersability of Exfoliated Nanosheets Varies Only Weakly Between Compounds. *Acs Nano 6*, 3468–3480.

[125] Israelachvili, J. *Intermolecular and surface forces: revised third edition*; Academic press, 2011.

[126] Nicolosi, V., Vrbanic, D., Mrzel, A., McCauley, J., O'Flaherty, S., McGuinness, C., Compagnini, G., Mihailovic, D., Blau, W. J., and Coleman, J. N. (2005) Solubility of Mo6S4.5I4.5 nanowires in common solvents: A sedimentation study. *Journal of Physical Chemistry B 109*, 7124–7133.

[127] Tory, E. *Sedimentation of small particles in a viscous fluid*; Computational Mechanics Publications, 1996.

[128] Burger, R., Evje, S., Hvistendahl Karlsen, K., and Lie, K. (2000) Numerical methods for the simulation of the settling of flocculated suspensions. *Chemical Engineering Journal 80*, 91–104.

[129] Garrido, P., Concha, F., and Burger, R. (2003) Settling velocities of particulate systems: 14. Unified model of sedimentation, centrifugation and filtration of flocculated suspensions. *International Journal of Mineral Processing 72*, 57–74.

[130] Atkins, P. *Physical Chemistry*; Oxford University press, 2002.

[131] Hennrich, F., Krupke, R., Arnold, K., Rojas Stutz, J. A., Lebedkin, S., Koch, T., Schimmel, T., and Kappes, M. M. (2007) The Mechanism of Cavitation-Induced Scission of Single-Walled Carbon Nanotubes. *The Journal of Physical Chemistry B 111*, 1932–1937.

[132] Huang, Y. Y., and Terentjev, E. M. (2012) Dispersion of Carbon Nanotubes: Mixing, Sonication, Stabilization, and Composite Properties. *Polymers 4*, 275–295.

[133] Lucas, A., Zakri, C., Maugey, M., Pasquali, M., van der Schoot, P., and Poulin, P. (2009) Kinetics of Nanotube and Microfiber Scission under Sonication. *Journal of Physical Chemistry C 113*, 20599–20605.

[134] Huang, Y. Y., Knowles, T. P. J., and Terentjev, E. M. (2009) Strength of Nanotubes, Filaments, and Nanowires From Sonication-Induced Scission. *Advanced Materials 21*, 3945–3948.

[135] Abergel, D., and Falako, V. (2007) Optical and magneto-optical far-infrared properties of bilayer graphene. *Physical Review B 75*, 155430.

[136] Ferrari, A. C., Meyer, J. C., Scardaci, V., Casiraghi, C., Lazzeri, M., Mauri, F., Piscanec, S., Jiang, D., Novoselov, K. S., Roth, S., and Geim, A. K. (2006) Raman Spectrum of Graphene and Graphene Layers. *Physical Review Letters 97*, 187401–187404.

[137] Li, H., Zhang, Q., Yap, C. C. R., Tay, B. K., Edwin, T. H. T., Olivier, A., and Baillargeat, D. (2012) From Bulk to Monolayer MoS2: Evolution of Raman Scattering. *Advanced Functional Materials 22*, 1385–1390.

[138] Ferrari, A. C. (2007) Raman spectroscopy of graphene and graphite: Disorder, electron-phonon coupling, doping and nonadiabatic effects. *Solid State Communications 143*, 47–57.

[139] Casiraghi, C., Hartschuh, A., Qian, H., Piscanec, S., Georgi, C., Fasoli, A., Novoselov, K. S., Basko, D. M., and Ferrari, A. C. (2009) Raman Spectroscopy of Graphene Edges. *Nano Letters 9*, 1433–1441.

[140] Reich, S., and Thomsen, C. (2004) Raman spectroscopy of graphite. *Philosophical Transactions: Mathematical, Physical and Engineering Sciences 362*, 2271–2288.

[141] Basko, D. M. (2009) Calculation of the Raman G peak intensity in monolayer graphene: role of Ward identities. *New Journal of Physics 11*, 095011.

[142] Graf, D., Molitor, F., Ensslin, K., Stampfer, C., Jungen, A., Hierold, C., and Wirtz, L. (2007) Raman imaging of graphene. *Solid State Communications 143*, 44–46.

[143] Malard, L., Pimenta, M., Dresselhaus, G., and Dresselhaus, M. (2009) Raman spectroscopy in graphene. *Physics Reports 473*, 51 – 87.

[144] Wieting, T. J., and Verble, J. L. (1971) Infrared and Raman Studies of Long-Wavelength Optical Phonons in Hexagonal MoS(2). *Phys. Rev. B 3*, 4286–4292.

[145] Molina-Sanchez, A., and Wirtz, L. (2011) Phonons in single-layer and few-layer MoS2 and WS2. *Phys. Rev. B 84*, 155413.

[146] Lee, C., Yan, H., Brus, L. E., Heinz, T. F., Hone, J., and Ryu, S. (2010) Anomalous Lattice Vibrations of Single- and Few-Layer MoS2. *Acs Nano 4*, 2695–2700.

[147] Li, S., Miyazaki, H., Song, H., Kuramochi, H., Nakaharai, S., and Tsukagoshi, K. (2012) Quantitative Raman Spectrum and Reliable Thickness Identification for Atomic Layers on Insulating Substrates. *ACS nano 6*, 7381–7388.

[148] Williams, D., and Carter, C. *Transmission electron microscopy: a textbook for materials science*; Springer, 2009.

[149] Horiuchi, S., Gotou, T., Fujiwara, M., Asaka, T., Yokosawa, T., and Matsui, Y. (2004) Single graphene sheet detected in a carbon nanofilm. *Applied Physics Letters 84*, 2403–2405.

[150] Dreyer, D., Ruoff, R., and Bielawski, C. (2010) From conception to realization: an historial account of graphene and some perspectives for its future. *Angewandte Chemie International Edition 49*, 9336–9344.

[151] Hennrich, F., Krupke, R., Arnold, K., Stutz, J., Lebedkin, S., Koch, T., Schimmel, T., and Kappes, M. (2007) The mechanism of cavitation-induced scission of single-walled carbon nanotubes. *Journal of Physical Chemistry B-Condensed Phase 111*, 1932–1937.

[152] Giordani, S., Bergin, S., Nicolosi, V., Lebedkin, S., Kappes, M., Blau, W., and Coleman, J. (2006) Debundling of single-walled nanotubes by dilution: observation of large populations of individual nanotubes in amide solvent dispersions. *J. Phys. Chem. B 110*, 15708–15718.

[153] Malard, L. M., Guimaraes, M. H. D., Mafra, D. L., Mazzoni, M. S. C., and Jorio, A. (2009) Group-theory analysis of electrons and phonons in N-layer graphene systems. *Physical Review B 79*, 125426–125434.

[154] Padawer, G. E., and Beecher, N. (1970) On Strength and Stiffness of Planar Reinforced Plastic Resins. *Polymer Engineering and Science 10*, 185–192.

[155] Hu, H. W., and Chen, G. H. (2010) Electrochemically Modified Graphite Nanosheets and Their Nanocomposite Films with Poly(vinyl alcohol). *Polymer Composites 31*, 1770–1775.

[156] Jiang, L., Shen, X. P., Wu, J. L., and Shen, K. C. (2010) Preparation and Characterization of Graphene/Poly(vinyl alcohol) Nanocomposites. *Journal of Applied Polymer Science 118*, 275–279.

[157] Kim, I. H., and Jeong, Y. G. (2010) Polylactide/Exfoliated Graphite Nanocomposites with Enhanced Thermal Stability, Mechanical Modulus, and Electrical Conductivity. *Journal of Polymer Science Part B-Polymer Physics 48*, 850–858.

[158] Liang, J. J., Huang, Y., Zhang, L., Wang, Y., Ma, Y. F., Guo, T. Y., and Chen, Y. S. (2009) Molecular-Level Dispersion of Graphene into Poly(vinyl alcohol) and Effective Reinforcement of their Nanocomposites. *Advanced Functional Materials 19*, 2297–2302.

[159] Miller, S. G., Bauer, J. L., Maryanski, M. J., Heimann, P. J., Barlow, J. P., Gosau, J. M., and Allred, R. E. (2010) Characterization of epoxy functionalized graphite nanoparticles and the physical properties of epoxy matrix nanocomposites. *Composites Science and Technology 70*, 1120–1125.

[160] Putz, K. W., Compton, O. C., Palmeri, M. J., Nguyen, S. T., and Brinson, L. C. (2010) High-Nanofiller-Content Graphene Oxide-Polymer Nanocomposites via Vacuum-Assisted Self-Assembly. *Advanced Functional Materials 20*, 3322–3329.

[161] Ramanathan, T., Abdala, A. A., Stankovich, S., Dikin, D. A., Herrera-Alonso, M., Piner, R. D., Adamson, D. H., Schniepp, H. C., Chen, X., Ruoff, R. S., Nguyen, S. T.,

Aksay, I. A., Prud'homme, R. K., and Brinson, L. C. (2008) Functionalized graphene sheets for polymer nanocomposites. *Nature Nanotechnology 3*, 327–331.

[162] Steurer, P., Wissert, R., Thomann, R., and Mulhaupt, R. (2009) Functionalized Graphenes and Thermoplastic Nanocomposites Based upon Expanded Graphite Oxide. *Macromolecular Rapid Communications 30*, 316–327.

[163] Yang, X. M., Li, L. A., Shang, S. M., and Tao, X. M. (2010) Synthesis and characterization of layer-aligned poly(vinyl alcohol)/graphene nanocomposites. *Polymer 51*, 3431–3435.

[164] Zhao, X., Zhang, Q. H., Chen, D. J., and Lu, P. (2010) Enhanced Mechanical Properties of Graphene-Based Poly(vinyl alcohol) Composites. *Macromolecules 43*, 2357–2363.

[165] Nirmalraj, P. N., Lutz, T., Kumar, S., Duesberg, G. S., and Boland, J. J. (2011) Nanoscale Mapping of Electrical Resistivity and Connectivity in Graphene Strips and Networks. *Nano Letters 11*, 16–22.

[166] Lyons, P. E., De, S., Blighe, F., Nicolosi, V., Pereira, L. F. C., Ferreira, M. S., and Coleman, J. N. (2008) The relationship between network morphology and conductivity in nanotube films. *Journal of Applied Physics 104*.

[167] Duesberg, G. S., Burghard, M., Muster, J., Philipp, G., and Roth, S. (1998) Separation of carbon nanotubes by size exclusion chromatography. *Chemical Communications* 435–436.

[168] De, S., and Coleman, J. N. (2010) Are There Fundamental Limitations on the Sheet Resistance and Transmittance of Thin Graphene Films? *Acs Nano 4*, 2713–2720.

[169] Hamilton, C. E., Lomeda, J. R., Sun, Z. Z., Tour, J. M., and Barron, A. R. (2009) High-Yield Organic Dispersions of Unfunctionalized Graphene. *Nano Letters 9*, 3460–3462.

[170] Bourlinos, A. B., Georgakilas, V., Zboril, R., Steriotis, T. A., Stubos, A. K., and Trapalis, C. (2009) Aqueous-phase exfoliation of graphite in the presence of

polyvinylpyrrolidone for the production of water-soluble graphenes. *Solid State Communications 149*, 2172–2176.

[171] De, S., King, P., Lotya, M., O'Neill, A., Doherty, E., Hernandez, Y., Duesberg, G., and Coleman, J. (2010) Flexible, Transparent, Conducting Films of Randomly Stacked Graphene from Surfactant Stabilized, Oxide Free Graphene Dispersions. *Small 6*, 458–464.

[172] Zhang, X., Coleman, A., Katsonis, W., N. Browne, van Wees, B., and Feringa, B. (2010) Dispersion of graphene in ethanol using a simple solvent exchange method. *Chem. Commun. 46*, 7539–7541.

[173] Barton, A. F. M. (1975) Solubility parameters. *Chemical Reviews 75*, 731–753.

[174] Zhou, K., Mao, N., Wang, H., Peng, Y., and Zhang, H. (2011) A Mixed-Solvent Strategy for Efficient Exfoliation of Inorganic Graphene Analogues. *Angewandte Chemie-International Edition 50*, 10839–10842.

[175] Khan, U., Porwal, H., O'Neill, A., Nawaz, K., May, P., and Coleman, J. N. (2011) Solvent-Exfoliated Graphene at Extremely High Concentration. *Langmuir 27*, 9077–9082.

[176] Bergin, S. D., Nicolosi, V., Giordani, S., de Gromard, A., Carpenter, L., Blau, W. J., and Coleman, J. N. (2007) Exfoliation in ecstasy: liquid crystal formation and concentration-dependent debundling observed for single-wall nanotubes dispersed in the liquid drug gamma-butyrolactone. *Nanotechnology 18*.

[177] Geim, A. K. (2009) Graphene: Status and Prospects. *Science 324*, 1530–1534.

[178] Eranna, G., Joshi, B., Runthala, D., and Gupta, R. (2004) Oxide materials for development of integrated gas sensors-A comprehensive review. *Critical Reviews in Solid State and Materials Sciences 29*, 111–188.

[179] Martinez, H. M., Torres, J., Rodriguez-Garcia, M., and Carreno, L. (2012) Gas sensing properties of nanostructured MoO3 thin films prepared by spray pyrolysis. *Physica B: Condensed Matter 407*, 3199–3202.

[180] Granqvist, C. *Handbook of inorganic electrochromic materials*; Elsevier Science, 1995.

[181] Ivanova, T., Gesheva, K., Popkirov, G., Ganchev, M., and Tzvetkova, E. (2005) Electrochromic properties of atmospheric CVD MoO_3 and MoO_3-WO_3 films and their application in electrochromic devices. *Materials science and engineering B 119*, 232–239.

[182] Mai, L., Hu, B., Chen, W., Qi, Y., Lao, C., Yang, R., Dai, Y., and Wang, Z. (2007) Lithiated MoO_3 Nanobelts with Greatly Improved Performance for Lithium Batteries. *Advanced Materials 19*, 3712–3716.